

## An experimental approach into the quantification of steering and balance behaviour of bicyclists

Dialynas, G.

**DOI**

[10.4233/uuid:3c6817fd-9d04-4461-9253-f02f0ca78a6a](https://doi.org/10.4233/uuid:3c6817fd-9d04-4461-9253-f02f0ca78a6a)

**Publication date**

2020

**Document Version**

Final published version

**Citation (APA)**

Dialynas, G. (2020). *An experimental approach into the quantification of steering and balance behaviour of bicyclists*. [Dissertation (TU Delft), Delft University of Technology]. <https://doi.org/10.4233/uuid:3c6817fd-9d04-4461-9253-f02f0ca78a6a>

**Important note**

To cite this publication, please use the final published version (if applicable).  
Please check the document version above.

**Copyright**

Other than for strictly personal use, it is not permitted to download, forward or distribute the text or part of it, without the consent of the author(s) and/or copyright holder(s), unless the work is under an open content license such as Creative Commons.

**Takedown policy**

Please contact us and provide details if you believe this document breaches copyrights.  
We will remove access to the work immediately and investigate your claim.

## An experimental approach into the quantification of steering and balance behaviour of bicyclists

Dialynas, G.

**DOI**

[10.4233/uuid:3c6817fd-9d04-4461-9253-f02f0ca78a6a](https://doi.org/10.4233/uuid:3c6817fd-9d04-4461-9253-f02f0ca78a6a)

**Publication date**

2020

**Document Version**

Final published version

**Citation (APA)**

Dialynas, G. (2020). *An experimental approach into the quantification of steering and balance behaviour of bicyclists*. <https://doi.org/10.4233/uuid:3c6817fd-9d04-4461-9253-f02f0ca78a6a>

**Important note**

To cite this publication, please use the final published version (if applicable).  
Please check the document version above.

**Copyright**

Other than for strictly personal use, it is not permitted to download, forward or distribute the text or part of it, without the consent of the author(s) and/or copyright holder(s), unless the work is under an open content license such as Creative Commons.

**Takedown policy**

Please contact us and provide details if you believe this document breaches copyrights.  
We will remove access to the work immediately and investigate your claim.

# **An experimental approach into the quantification of steering and balance behaviour of bicyclists**

## **Dissertation**

for the purpose of obtaining the degree of doctor at Delft University of Technology,  
by the authority of the Rector Magnificus, Prof. dr. ir. T.H.J.J. van der Hagen,  
chair of the Board for Doctorates, to be defended publicly on  
Tuesday, 15 September 2020 at 12:30 o'clock

by

**Georgios Dialynas**

Mechanical Engineer, Alexander Technological Educational Institute, Greece  
born in Athens, Greece

This dissertation has been approved by the

promotor: Dr. ir. R. Happee  
copromotor: Dr. ir. A. L. Schwab

Composition of the doctoral committee:

Rector Magnificus	Chairperson
Dr. ir. R. Happee	Delft University of Technology
Dr. ir. A. L. Schwab	Delft University of Technology

Independent members:

Prof. Dr. ir. D. A. Abbink	Delft University of Technology
Prof. Dr. M. Pierini	Università degli Studi di Firenze, Italy
Prof. Dr. M. Dozza	Chalmers University of Technology, Sweden
Dr. J. L. Escalona Franco	University of Seville, Spain
Dr. J. K. Moore	University of California, Davis
Prof. Dr. M. Hagenzieker	Delft University of Technology, reserve member

This research has been funded by the Marie Curie Initial Training Network through the project MOTORIST (Motorcycle Rider Integrated Safety) grant Nr.608092, [www.motorist-ptw.eu](http://www.motorist-ptw.eu)



Copyright © 2020 by Georgios Dialynas

All rights reserved. No part of the material protected by this copyright notice may be reproduced or utilized in any form or by any means, electronic or mechanical, including photocopying, recording or by any information storage and retrieval system, without written permission from the author.

*Science is a wonderful thing if one does not have to earn one's living at it.*

Albert Einstein



# Contents

<b>Summary</b>	<b>8</b>
<b>1 Introduction</b>	<b>1</b>
References	5
<b>2 Some effects of crosswind on the lateral dynamics of a bicycle</b>	<b>6</b>
2.1 Abstract	6
2.2 Introduction	6
2.3 Methods	7
2.3.1 Bicycle model	8
2.3.2 Crosswind	8
2.3.3 Time series	10
2.4 Rider control	10
2.5 Results and discussion	11
2.6 Conclusions	14
References	14
<b>3 The dynamic response of the bicycle rider's body to vertical, fore-and-aft and lateral perturbations</b>	<b>16</b>
3.1 Abstract	16
3.2 Introduction	17
3.3 Methods	18
3.3.1 Description of experimental set-up	18
3.3.2 Perturbation signal selection and design	20
3.3.3 Procedure	21
3.4 Data recording and processing	22
3.4.1 Subjective measures	22
3.4.2 Static and dynamic force measurements	22
3.4.3 Transfer functions	23
3.4.4 Seat-to-sternum transmissibility (STST)	24
3.4.5 Apparent mass (APMS)	25
3.5 Results	25
3.5.1 NASA-TLX	25
3.5.2 Static and dynamic force distribution	25
3.5.3 STST	27
3.5.4 APMS	27
3.6 Discussion	30
3.7 Conclusion	34
References	36

<b>4</b>	<b>Design and implementation of a steer-by-wire bicycle</b>	<b>39</b>
4.1	Abstract . . . . .	39
4.2	Introduction . . . . .	40
4.3	System design and simulation . . . . .	41
4.4	Hardware description . . . . .	45
4.5	Tracking controller performance . . . . .	46
4.6	Conclusions . . . . .	48
	References . . . . .	49
<b>5</b>	<b>The effect of haptic feedback in the balance task of bicycling</b>	<b>51</b>
5.1	Abstract . . . . .	51
5.2	Introduction . . . . .	51
5.3	Methods . . . . .	52
5.3.1	Description of experimental set-up . . . . .	52
5.3.2	Description of steer-by-wire controller . . . . .	53
5.3.3	Experimental procedure . . . . .	54
5.3.4	System identification . . . . .	54
5.3.5	Comparison metrics . . . . .	55
5.4	Results . . . . .	56
5.5	Discussion and conclusions . . . . .	59
	References . . . . .	60
<b>6</b>	<b>Rider control identification in cycling taking into account steer torque feedback and sensorial delays</b>	<b>61</b>
6.1	Abstract . . . . .	61
6.2	Introduction . . . . .	62
6.3	Methods . . . . .	64
6.3.1	Description of experimental set-up . . . . .	64
6.3.2	Description of steer-by-wire controller . . . . .	64
6.3.3	Procedure . . . . .	65
6.4	System model . . . . .	66
6.4.1	Bicycle model . . . . .	67
6.4.2	State space representation . . . . .	69
6.4.3	Rider control model . . . . .	71
6.4.4	Neuromuscular dynamics . . . . .	71
6.4.5	Combined plant model . . . . .	72
6.4.6	Sensory delay reafferent optimal predictor (SDROP) . . . . .	73
6.5	System identification . . . . .	74
6.5.1	Black box model . . . . .	75
6.5.2	Gray box model . . . . .	77
6.5.3	Parameter estimation . . . . .	77
6.5.4	Performance metrics . . . . .	78
6.6	Results . . . . .	78
6.6.1	Zero delay (ZD) . . . . .	79
6.6.2	With sensory delay (SD) . . . . .	79

6.6.3	Sensory delay reafferent optimal predictor (SDROP)	81
6.6.4	Testing and validation . . . . .	81
6.7	Discussion . . . . .	85
6.8	Conclusion . . . . .	87
	References . . . . .	93
<b>7</b>	<b>Design and hardware selection for a bicycle simulator</b>	<b>96</b>
7.1	Abstract . . . . .	96
7.2	Introduction . . . . .	96
7.3	Design requirements of bicycle simulator interfaces . . . . .	97
7.4	Description of the mechanical structure . . . . .	99
7.4.1	Description of haptic steering device . . . . .	101
7.4.2	Description of overload protection mechanism . . . . .	102
7.5	Sensor and motor selection . . . . .	103
7.6	Calibration and testing of hardware components . . . . .	106
7.6.1	Estimation of steering shaft moment of inertia . . . . .	109
7.7	Conclusions . . . . .	111
	References . . . . .	112
<b>8</b>	<b>Discussion</b>	<b>114</b>
8.1	Facilities . . . . .	114
8.1.1	Instrumented bicycle mock-up . . . . .	114
8.1.2	Steer-by-wire bicycle . . . . .	116
8.1.3	Bicycle simulator . . . . .	118
8.1.4	Summary . . . . .	119
8.2	Findings . . . . .	120
8.2.1	Some effects of crosswind on the lateral dynamics of a bicycle . . . . .	120
8.2.2	The dynamic response of the bicycle rider's body to vertical, fore-and-aft and lateral perturbations . . . . .	121
8.2.3	Rider control identification in bicycling using lateral force perturbation tests . . . . .	122
8.2.4	Bicycle simulator . . . . .	123
8.3	Integration and outlook . . . . .	123
	References . . . . .	124
<b>9</b>	<b>Conclusions</b>	<b>126</b>
	<b>Acknowledgements</b>	<b>129</b>
	<b>Publications</b>	<b>131</b>
	<b>Curriculum Vitæ</b>	<b>132</b>
	<b>Propositions belonging to the PhD thesis</b>	<b>133</b>

# Summary

The aim of this thesis is to derive bicycle rider control models, based on experimental data, that mimic the rider in his balance control task at various forward speeds. These rider control models can help to understand cyclists falls, improve training techniques, assess the handling properties of new bicycle designs and create active balance control systems (e.g. steer assist). This thesis consists of 9 Chapters; Chapter 1 introduces relevant background theory and identifies the research gap.

Chapter 2 presents some effects of crosswind on the lateral dynamics of a bicycle and on rider control. The Chapter gives an insight on how rider control modelling can be used to assess crosswind related falls. Simulations indicated that crosswind has a considerable effect on the stability and control of the bicycle. Increasing wind speed can make an uncontrolled bicycle resonate for all forward speeds. The rider control effort increases considerably and a constant steer torque is required to keep the bicycle at a straight heading.

Chapter 3 investigates the dynamic response of the bicycle rider's body during vertical, fore-and-aft and lateral perturbations in order to understand how riders are using postural control to restrain excessive movements and prevent falling off the seat. The analysis is presented by means of apparent mass (APMS) and seat-to-sternum transmissibility (STST) functions in the frequency domain. Measured forces at saddle, steer and pedals revealed that for each individual motion the rider applied forces in all three directions. Heave and surge motion interacted with each other and had similar responses. Sway showed totally different responses and weak interaction with the other two motions. Resonant frequencies were considerably higher in the vertical direction as compared to the longitudinal direction. Lateral measurements showed no resonance, and trunk postural control was evident in the APMS. The results of this Chapter can be used to identify the parameters of biodynamic lumped human-machine models. Such models can support the development of more comfortable and safe bicycle designs and suspension systems.

Chapter 4 presents the design and implementation of an instrumented steer-by-wire bicycle (SBW) that was designed and built at TU Delft bicycle laboratory. The SBW was used as a versatile experimental platform to capture the rider's responses with (haptics on) and without steering torque feedback (haptics off) during lateral perturbation experiments. Simulations and testing of the steer-by-wire system indicated good tracking performance between 0-2.5 Hz and almost identical steer stiffness with the Carvallo-Whipple bicycle model in a frequency range of 0-3 Hz and in a forward speed range of 0-10 m/s.

The bicycle served its purpose successfully, the responses of the rider's control actions with lateral perturbations were captured by means of impulse response functions (IRFs) in Chapter 5. Results failed to indicate any statistically significant difference between the two steering configurations (haptics on/ off).

Chapter 6 presents and validates a parametric rider control model using data presented in Chapter 5 and uses this model to further assess the effect of haptic feedback in the balance task of bicycling. Bicycle and rider mechanics have been modelled using the Carvallo-Whipple bicycle model extended with rider inertia. A balancing and heading controller was added, capturing visual, vestibular and proprioceptive sensory information using feedback of roll angle, roll angle rate, heading angle, heading angle rate, steering angle and steering torque, taking into account muscular activation dynamics. Non-parametric and parametric model responses failed to indicate any statistically significant difference between the haptics on/off configurations. However, further analysing the haptic off configuration it became apparent that the rider still receives relevant torque feedback due to the inertia of the handlebars. The reduced feedback was proven to be adequate for the rider to control the bicycle without any major steering discrepancies. To further evaluate the effect of torque feedback in simulations we disconnected the handlebar torque feedback loop of the parametric rider model. In addition, we also disconnected the handlebar position and velocity feedback. Results showed that handlebar torque feedback is significantly important during the riding process. This knowledge might be crucial for the development of new safety systems that could further optimize bicycle handling and assist the rider's steer control actions in critical situations preventing falls.

Chapter 7 outlines the design and hardware selection for a bicycle simulator. The design requirements together with a detailed description of the hardware selection and testing are presented. The simulator was designed to explore human control behaviour in a safe environment. Preliminary tests showed that all subjects can balance and manoeuvre the bicycle when a simplified bicycle model is used to generate haptic feedback and project the dynamics in the virtual environment. Visual roll of the horizon turned out to be an effective tool for creating the illusion of physical roll but motion sickness was reported.

This thesis ends with the discussion and conclusion Chapters 8, 9 highlighting the developed experimental facilities and main findings of the research. The Chapters herein investigate the effects of external perturbations on bicycle stability and human control using numerical modelling and experimental bicycles capable of measuring kinematics and rider applied forces. This interdisciplinary approach delves into the foundations of human control modelling from both a biomechanical and biomechatronics engineering perspective in an effort to improve cycling safety and reduce falls.



# 1

## Introduction

### Problem statement

According to the European Road Safety Observatory [1] in 2016 about 2.000 cyclists were killed in road accidents throughout the EU. Despite the overall reduction in the road toll (down 40% from 2007), the proportion of cycling-related fatalities<sup>1</sup> increased, from 6% in 2007 to 8% in 2016, see Figure 1.1. These preventable deaths have created a significant need to better understand the characteristics specifically to this user group. The majority of the cycling accidents are “single vehicle accidents”, meaning that there are no other road users involved [2]. The cyclists simply fall off their bicycles due to loss of steering and balance control. To improve cycling safety and prevent the actual falls a quantitative approach is necessary not only to reveal the cause of these accidents but also to create models that mimic the rider in his balance control task.

### Research gap

Even though over 50 percent of the human population knows how to ride a bike, yet the way humans control and balance a bicycle has not been fully understood or quantified from a scientific point of view. The majority of studies available in the literature focus on bicycle dynamics and do not incorporate a rider model [3–6]. A detailed review on bicycle dynamics and rider control is given by A. L. Schwab et al. [7]. Only two studies can be found in the literature that try to identify the effect of rider motion [8] and rider control [9] on bicycle dynamics and only one that actually investigates the effect of a passive rider model on the lateral dynamics of a bicycle [10].

---

<sup>1</sup>Fatality refers to any road user who was killed outright or who died within 30 days as a result of the accident.

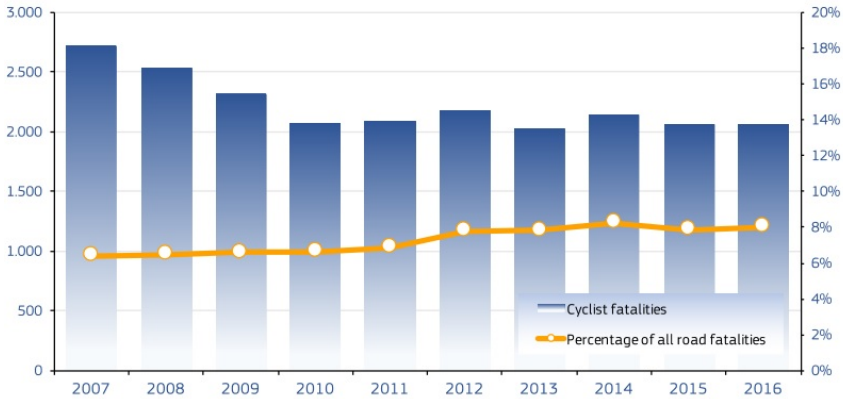


Figure 1.1: Number of cyclist fatalities and percentage of all road fatalities, EU, 2007-2016.

## Thesis embedding

This thesis is part of the MOTORIST (Motorcycle Rider Integrated Safety) project Nr.608092, [www.motorist-ptw.eu](http://www.motorist-ptw.eu). The objective of the research activities of the MOTORIST project was to make the use of Powered Two Wheelers (PTWs) safer. The project was divided into three work packages (WPs) with three separate but related goals.

- WP1 aimed to improve the rider's skills with training strategies that are derived from in-depth accident data and from a quantification of rider behaviour in critical situations.
- WP2 aimed at developing advanced safety systems that improve the interaction between the rider and the PTW by modelling the rider.
- WP3 considered the cases where the crash is unavoidable and will develop personal protective equipment to protect the riders, given the input conditions from WP2 at the moment right before impact.

The work of this thesis covers the position of early stage researcher (ESR 2.2) and relates to WP2 of the MOTORIST project.

## Thesis aim

The aim of this thesis is to derive bicycle rider control models, based on experimental data, that mimic the rider in his balance control task at various forward speeds. These rider control models can help to understand cyclists falls, improve training techniques, assess the handling properties of new bicycle designs and create active balance control systems (e.g. steer assist).

## Methods

To derive these bicycle rider control models three experimental setups have been built. The first is to determine the passive rider contribution to the dynamic model of a Carvallo-Whipple type of bicycle model [5] to create a dynamic rider-bicycle system. A bicycle mock-up is equipped with sensors measuring three-dimensional seat and trunk accelerations and rider's force responses at the seat, handlebars and footpegs. The bicycle mock-up is driven by a hexapod motion platform that generates random noise perturbations in all translational motions. The responses of the rider's body are captured by means of three-dimensional force interactions at the seat, handlebars and footpegs in terms of apparent mass, and rider's trunk motion one-dimensional as function of seat motion as seat-to-sternum transmissibility. The second is a fully instrumented steer-by-wire bicycle to collect measured data for rider control identification under random lateral perturbations. The steer-by-wire bicycle is equipped with multiple sensors measuring most bicycle states required for identification, including steer torque, steer angle, roll angle and forward velocity. Two servomotors are used to control the fork and handlebars, and a rear wheel hub-motor with cruise controller to ride the bicycle at constant speeds. Rider responses are captured by linear impulse response functions and are used to evaluate rider-bicycle models in their ability to capture human behaviour. The third is a fixed base bicycle simulator to execute rider control experiments in a safe manner. The bicycle simulator is equipped with a haptic steering device and sensors capable of measuring the applied steer torque, angle and forward velocity. The virtual environment is developed in the Unity® game engine and can be displayed to the rider via standard monitors or virtual reality headset such as the Oculus Rift. Preliminary rider tests using the bicycle simulator are conducted in order to evaluate the ability of the subjects to balance and manoeuvre the bicycle in a virtual environment.

## Impact to society

The work presented in this thesis has revealed a number of interesting conclusions for both bicycle dynamics and rider control. The influence of crosswind on the lateral dynamics of a bicycle indicated resonance at certain wind speeds and loss of control. The dynamic response of the rider's body subjected to translational motions indicated resonant-like behaviour for the vertical and fore-and-aft motions and complex human control during the sway motion. The steer-by-wire bicycle outperformed and proved to be extremely useful as a platform to conduct rider control identification experiments which revealed that steering feedback is important for balancing a bicycle. Future applications may be able to utilize the methods and results of this thesis to help objectively design safer bicycles by the following steps:

- improve the rider's skills with training strategies that are derived from a quantification of rider behaviour in critical situations.
- improve bicycle stability by artificially evaluating the handling, stability and controllability of new bicycle designs under the influence of external disturbances.
- evaluate the performance and comfort of given vibration isolators by incorporating a passive rider model.
- improve bicycle stability by developing new safety systems such as steer assist.

## Thesis structure

The thesis consists of 9 Chapters; Chapter 1 introduces relevant background theory in order to reveal the motivation of this study and research gap prior to this thesis. Chapter 2 examines the effect of crosswind on the lateral dynamics and control of the bicycle in a wide range of forward speeds and various crosswinds, by means of computer model analysis and simulation. A three-degrees-of-freedom bicycle model is used together with an experimentally identified rider controller. Chapter 3 investigates the dynamic response of the bicycle rider's body during translational perturbations, in an effort to improve two-wheeler safety and comfort. A bicycle mock-up is equipped with sensors measuring three-dimensional seat and one-dimensional trunk accelerations and rider's force responses at the seat, handlebars and footpegs. The bicycle mock-up is driven by a hexapod motion platform that generates random noise perturbations. Chapter 4 describes the design and implementation of a steer-by-wire bicycle. A linear multibody model for the bicycle is used to design the system. The model is based on the three-degree-of-freedom Carvallo-Whipple bicycle model. The model is extended by separating the handlebar assembly from the fork assembly, which introduces an additional rotational degree of freedom. The performance of the steer-by-wire bicycle is evaluated in both computer simulations as well as real-life tests. Chapter 5 presents the effect of haptic feedback in the balance task of bicycling during lateral perturbation tests. The steer-by-wire bicycle described in Chapter 4 is used as an experimental platform to analyse the rider response with (haptics on) and without (haptics off) steering feedback. The response of the rider's control actions is represented in the time domain by means of impulse response functions (IRFs). To further examine the effect of proprioceptive feedback on the balance and control of a bicycle, three parametric rider models with increase complexity are presented in Chapter 6. Two metrics are used to assess the performance of the simulated and actual responses. The covariance coefficient (CV) of the estimated controller parameters is used as a measure of uncertainty, whereas the variance accounted (VAF) as a measure of fitting between the responses. Chapter 7 outlines the design and hardware selection for a bicycle simulator. The design requirements together with a detailed description of the hardware selection and testing are presented. The thesis ends with the discussions and conclusions Chapter 8, 9 highlighting the main findings of

this research.

## References

- [1] E. Commission, *Traffic safety basic facts on cyclists*, European Commission, Directorate-General for Mobility and Transport (2018).
- [2] P. Schepers and K. K. Wolt, *Single-bicycle crash types and characteristics*, Cycling Research International **2**, 119 (2012).
- [3] J. Godthelp and M. Buist, *Stability and manoeuvrability characteristics of single track vehicles*. (Soesterberg, Intitute for Reception TNO, 1975, 30 cm., 86 p., fig., graph ..., 1975).
- [4] J. P. Meijaard and A. L. Schwab, *Linearized equations for an extended bicycle model*, in *III European Conference on Computational Mechanics* (Springer, 2006) pp. 772–772.
- [5] J. P. Meijaard, J. M. Papadopoulos, A. Ruina, and A. L. Schwab, *Linearized dynamics equations for the balance and steer of a bicycle: a benchmark and review*, in *Proceedings of the Royal Society of London A: Mathematical, Physical and Engineering sciences*, Vol. 463 (The Royal Society, 2007) pp. 1955–1982.
- [6] J. Kooijman, J. P. Meijaard, J. M. Papadopoulos, A. Ruina, and A. L. Schwab, *A bicycle can be self-stable without gyroscopic or caster effects*, Science **332**, 339 (2011).
- [7] A. L. Schwab and J. Meijaard, *A review on bicycle dynamics and rider control*, Vehicle System Dynamics **51**, 1059 (2013).
- [8] J. K. Moore, J. Kooijman, A. L. Schwab, and M. Hubbard, *Rider motion identification during normal bicycling by means of principal component analysis*, Multibody System Dynamics **25**, 225 (2011).
- [9] A. L. Schwab, P. D. L. de Lange, R. Happee, and J. K. Moore, *Rider control identification in bicycling using lateral force perturbation tests*, Proceedings of the Institution of Mechanical Engineers Conference, Part K: Journal of Multibody Dynamics **227**, 390 (2013).
- [10] A. L. Schwab, J. Meijaard, and J. Kooijman, *Lateral dynamics of a bicycle with a passive rider model: stability and controllability*, Vehicle System Dynamics **50**, 1209 (2012).

# 2

## Some effects of crosswind on the lateral dynamics of a bicycle

Corresponding article: A. L. Schwab, G. Dialynas and R. Happee, Some effects of crosswind on the lateral dynamics of a bicycle, In Multidisciplinary Digital Publishing Institute Proceedings **2**, 218, (2018), <https://doi.org/10.3390/proceedings2060218>.

### 2.1. Abstract

The bicycle, being unstable at low speed and marginally stable at high speed, is sensitive to lateral perturbations. One of the major lateral perturbations is crosswind, which can lead to accidents and fatalities. Here we investigate the effect of crosswind on the lateral dynamics and control of the bicycle in a wide range of forward speeds and various crosswinds, by means of computer model analysis and simulation. A low dimensional bicycle model is used together with experimentally identified rider control parameters. The crosswind forces are obtained from a recent experimental study. Analysis and simulation show that crosswind decreases the stability of the bicycle and is clearly a safety issue.

#### **Keywords**

Bicycle, crosswind, dynamics, control, stability, handling.

### 2.2. Introduction

Aerodynamic drag in bicycling has been studied extensively, with the main goal to reduce drag and improve performance, see f.i. [1]. Only very few studies have

been done on the effect of crosswind in bicycling, one of the first being Godthelp et al. [2]. Nathan Barry et al. [3] measured the effect of crosswinds and wheel selection on the aerodynamic behavior of a cyclist. In competitive cycling the need for speed with less physical effort has also lead researchers to study the aerodynamic drag interactions between cyclists in a team pursuit [4]. Belloli et al. [5] investigated drafting effects between two cyclists by wind tunnel tests. Blocken et al. [6, 7] investigated the upstream effect on the cyclist by a following car, and a motorcycle using (CFD) simulations and wind tunnels tests. Kyle et al. [8] present a review on the history of aerodynamics in cycling and physical factors that influence performance.

Here we study the effect of crosswind on the lateral dynamics and control of the bicycle by means analysis and simulation on a computational model. Crosswind is a lateral perturbation on bicycling. The bicycle, being unstable at low speed and marginally stable at high speed, is very sensitive to such a lateral perturbation, and there is a clear safety issue here. Although the total number of accidents caused by crosswind is small (5%), the effect is large since the majority of these accidents lead to severe or fatal accidents [9].

This paper is organized as follows. After this introduction the methods for model analysis and simulation are described. Next some results of various cases are presented and discussed, and the paper ends with some conclusions.

## 2.3. Methods

To study the effect of crosswind on the dynamics and control of a bicycle three basic ingredients are needed: a bicycle model, crosswind data, and a bicycle rider controller. For the bicycle model the recently benchmarked low dimensional Carvallo-Whipple bicycle model [10] is used. This is a minimal, three-degree of freedom, model of a bicycle rider system that is still able to show realistic lateral dynamics. The lateral forces generated by the crosswind are obtained from a recent experimental study by Fintelman et al. [11]. They measured the aerodynamic forces on a full-scale bicycle with mannequin for a variety of crosswind angles ranging from 0-90 degrees in a wind tunnel. In order to study the effect of crosswind in the unstable forward speed range of the bicycle, a realistic rider control model is added to the bicycle model. The added controller is a linear steer torque controller with full state feedback, where the feedback gains were obtained experimentally from a system identification process on a real bicycle rider system riding on a treadmill [12].

The effect of crosswind is studied by means of time series analysis on the models, which are obtained by numerical integration of the equations of motion. Although the lateral dynamics can be described by a set of linear differential equations [10], the large change in heading angle of the bicycle at a space-fixed wind speed angle, adds a nonlinear element to the analysis.

### 2.3.1. Bicycle model

For the lateral bicycle dynamics the low dimensional Carvallo-Whipple bicycle model is used. This model, as shown in Figure 2.1, is fully described and benchmarked by Meijaard et al. [10]. For small nominal motions of the upright position, the longitudinal and lateral motions are decoupled. The forward dynamics can be described by one degree of freedom, the forward speed  $v$ . Here we assume constant forward speed. The lateral dynamics can be described by two-degrees-of-freedom: the roll angle of the rear frame, denoted by  $\phi$ , and the steering angle between the rear frame and the front frame, denoted by  $\delta$ . The linearized equations for the lateral motion, if the bicycle is moving at a constant forward velocity  $v$ , have the structure

$$\mathbf{M}\ddot{\mathbf{q}} + v\mathbf{C}_1\dot{\mathbf{q}} + [g\mathbf{K}_0 + v^2\mathbf{K}_2]\mathbf{q} = \mathbf{T} \quad (2.1)$$

where  $\mathbf{q} = [\phi, \delta]^T$  is the vector of generalized coordinates, the degrees-of-freedom,  $\mathbf{T} = [T_\phi, T_\delta]^T$  is the vector of generalised forces,  $\mathbf{M}$  is the mass matrix,  $v\mathbf{C}_1$  is the non-symmetric velocity sensitivity matrix that is linear in the velocity, and  $g\mathbf{K}_0 + v^2\mathbf{K}_2$  is the non-symmetric stiffness matrix that consists of a symmetric part that depends on the acceleration of gravity  $g$  and a part that is quadratic in the forward velocity  $v$ . The generalized forces are  $T_\phi$ , an externally applied roll moment to the rear frame and  $T_\delta$ , an applied action-reaction steer torque between the front frame and the rear frame. Expressions for the entries of the matrices in terms of geometric and mass parameters of the bicycle can be found in [10]. Here we use the values as presented by Schwab et al. [12], since for this specific bicycle rider configuration we are able to add, later on, experimentally determined rider control parameters.

Although the two-degrees-of-freedom fully describe the dynamics of the bicycle, the kinematics of the bicycle, i.e., the position of the rear contact point P on the plane and the heading of the bicycle, described by the yaw angle of the rear frame  $\psi$ , are described by the following set of first order differential equations,  $\dot{\psi} = \left(\frac{v^2\delta + c\dot{\delta}}{w}\right)\cos\epsilon$ ,  $\dot{x}_p = v\cos\psi$ , and  $\dot{y}_p = v\sin\psi$ , with the wheelbase  $w$ , the front wheel trail  $c$  and the head angle  $\epsilon$ , see Figure 2.1. Finally, the position of the front wheel contact point Q, which can be used for animation of the motion, can be calculated from the state variables and the kinematics as,  $x_Q = x_p + w\cos\psi + c\delta\cos\epsilon\sin\psi$ , and  $y_Q = y_p + w\sin\psi + c\delta\cos\epsilon\cos\psi$ .

### 2.3.2. Crosswind

For the aerodynamic forces the experimentally obtained data from Fintelman et al. [11] is used. They measured, in an open subsonic wind tunnel, the forces and moments exerted by the wind on a full-scale bicycle with mannequin. Measurements were done at a constant wind speed  $U_\infty$  of 9.91 m/s and for a variety of angles of attack  $\beta$  from 0 to 90 degrees. They present their results in the form of force and moment coefficients,  $C_{xA}$ , such that the forces and moments can be calcu-



and direction,  $\alpha$ , see Figure 2.2 (c). The apparent wind speed with respect to the bicycle,  $v_{\alpha}$ , is the vectorial sum of the absolute wind speed minus the forward speed of the bicycle. With the bicycle forward speed  $v$ , and bicycle heading  $\psi$ , the size and direction of the apparent wind speed with respect to the bicycle are,

$$v_{\alpha} = \sqrt{v^2 + 2vv_w \cos(\alpha - \psi) + v_w^2}, \quad \tan\beta = \frac{v_w \sin(\alpha - \psi)}{v + v_w \cos(\alpha - \psi)} \quad (2.4)$$

Finally, with these values the aerodynamics coefficients,  $C_{xA}$ , can be interpolated from Figures 3 and 6, as presented by Fintelman et al. [11], and the generalised applied torques (Equation 2.3) due to the crosswind can be calculated.

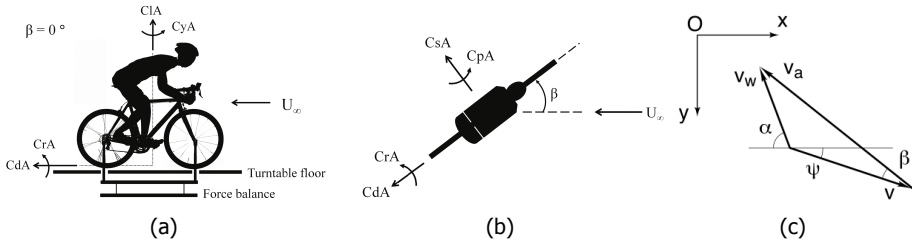


Figure 2.2: Bicycle and rider system subjected to crosswind together with the definition of the various aerodynamic force and moment coefficients and apparent wind speed, in (a) side view; and (b) top view, with drag force coefficient  $C_{dA}$ , lift force coefficient  $C_{lA}$ , side force coefficient  $C_{sA}$ , roll moment coefficient  $C_{rA}$ , pitch moment coefficient  $C_{pA}$ , and yaw moment coefficient  $C_{yA}$ ; Figures (a) and (b) from Fintelman et al. [11]; and (c) absolute wind speed  $v_w$  at an angle  $\alpha$ , forward speed of the bicycle  $v$  at a heading  $\psi$ , and apparent wind speed  $v_{\alpha}$  at an apparent angle  $\beta$  relative to the bicycle heading.

### 2.3.3. Time series

For the time series analysis the set of second order differential equations describing the lateral dynamics (Equation 2.1) together with the differential equation for the heading are numerically integrated with a Runge-Kutta fourth order scheme with variable stepwise for local error control. For visualisation it can be useful to show the path of the contact points on the ground. Then the differential equations of the rear contact point can be added to system of differential equations. The path of the front contact point can finally be constructed from the state variables and kinematic equations, as presented in Section 2.3.1.

## 2.4. Rider control

At low to moderate forward speed the bicycle is usually unstable and any lateral perturbation, like crosswind, will result in an unstable motion (fall to the ground). In order to investigate what the effect of crosswind is on the bicycle rider system, a rider controller is added to the system, stabilizing the system at low forward speed. In previous work it has been shown that most of the rider control in bicycling is done by steering only [14]. Therefore, a steer torque controller with full state feedback is

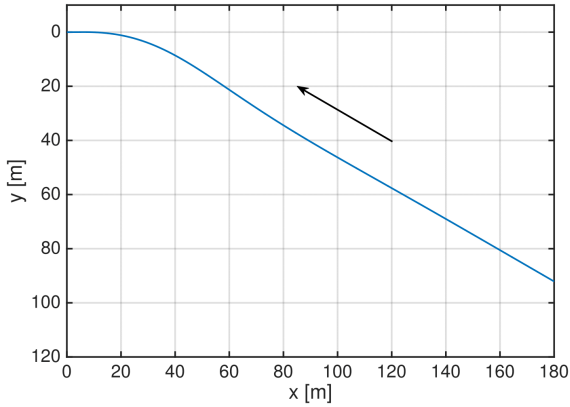
considered, where the feedback gains were obtained experimentally from a system identification process on a real bicycle rider system, riding on a treadmill [12]. This controller has the form,  $T_\delta = \mathbf{K}_c \mathbf{x}$ , with the linear feedback gains  $\mathbf{K}_c$ , and the state vector  $\mathbf{x} = [\dot{\phi}, \delta, \phi, \delta, \psi]$ . The feedback gains are scheduled for the specific forward speeds at hand. The values used in the simulation are represented in Table 2.1.

## 2.5. Results and discussion

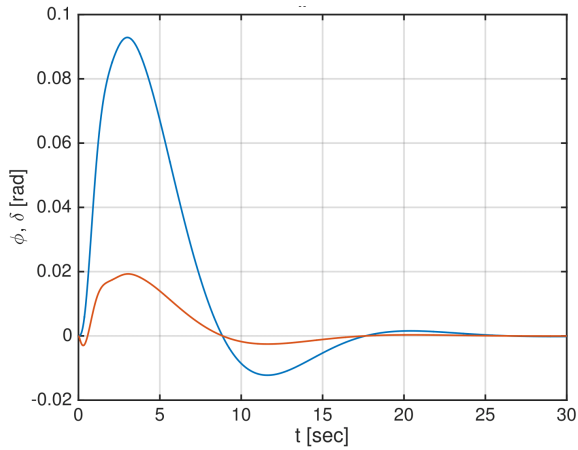
As a first example of the effect of crosswind on an uncontrolled bicycle two cases are considered. The first case is riding at a constant forward speed of  $v = 7.34$  m/s (where the uncontrolled unperturbed bicycle is stable) in a crosswind with absolute wind speed  $v_w = 2.0$  m/s at a wind speed angle of  $\alpha = 30$  degrees (Beaufort 2, light breeze). The analysis is done by means of a time series analysis, where the initial conditions on the bicycle are a zero roll and steer angle and zero roll and steer rate.

The path of the rear wheel contact point is shown in Figure 2.3 (a) and shows that, after a short transient manoeuvre, the uncontrolled bicycle turns into the wind (the arrow indicates the wind direction). The transient behaviour of the roll and steer angle are shown in Figure 2.3 (b), where initially ( $t < 1$  s) the crosswind force makes the bicycle steer to the left ( $\delta < 0$ ) which makes the bicycle fall over to the right ( $\phi > 0$ ), this roll angle reverses the steering and makes the bicycle steer into the wind. The roll and steer angles settle to zero after about 25 seconds. This is in a light breeze and the maximum roll and steer angle are respectively 5.3 and 1.1 degree. In the second case all conditions remain the same, except for the wind speed, which is increased to  $v_w = 8.0$  m/s. This corresponds to Beaufort 5, a fresh breeze. Again, the uncontrolled bicycle turns into the wind but now the oscillatory behaviour persists for a much longer time, as shown in Figure 2.4. The maximum roll and steer angle are now much larger, respectively 30 and 7.5 degree. The mildly damped oscillation demonstrates the effect of the wind force on the lateral stability of the bicycle, and shows that an increasing wind speed reduces the stability of the system.

As a last example, the effect of crosswind on a rider-controlled bicycle will be shown, by means of time series analysis. One case is considered, a low forward speed of  $v = 4.25$  m/s, where the uncontrolled bicycle is unstable. A rider control model, as described in Section 2.4, is added to make the system stable. The control parameters are according to Table 2.1. These rider control parameters were identified in an experiment where the rider was riding a bicycle on a treadmill [14]. Therefore, the controller not only tries to stabilise the bicycle, but also tries to keep the heading zero, otherwise one would run off the treadmill. The effect of crosswind with wind speed  $v_w = 10$  m/s at a wind direction of  $\alpha = 30$  degrees; is considered, this is again Beaufort 5, a fresh breeze. After some initial transient response of about 10 seconds, the rider-controlled bicycle settles at a constant roll angle of 0.3 degrees at a zero steer angle, and a constant steer torque of 0.9 Nm, which is a considerable effort.

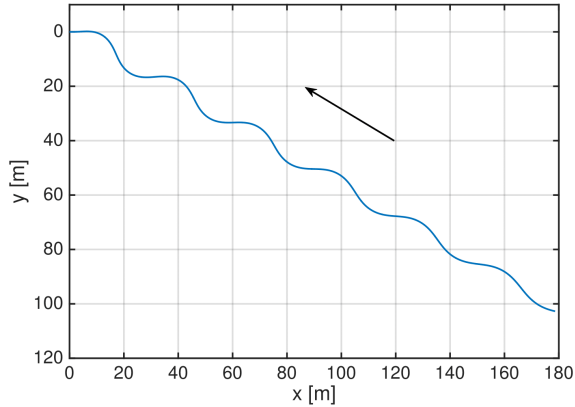


(a)

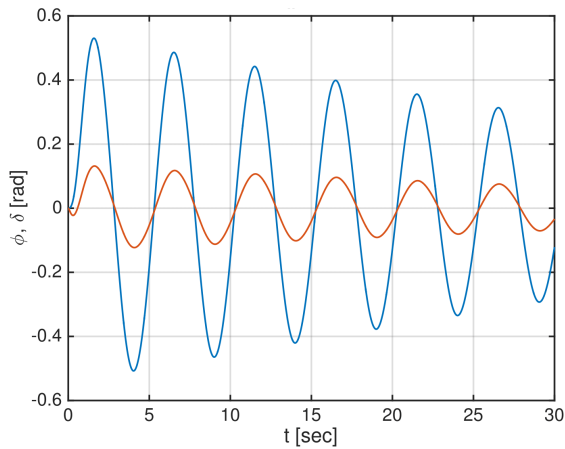


(b)

Figure 2.3: Time series of an uncontrolled bicycle running a constant forward speed of 7.34 m/s against a crosswind of 2.0 m/s at 30 degrees (Beaufort 2, light breeze); (a) path of the rear wheel contact point (arrow indicates the wind direction) (b) bicycle roll angle (blue) and steer angle (red) as a function of time.



(a)



(b)

Figure 2.4: Time series of an uncontrolled bicycle running a constant forward speed of 7.34 m/s against a crosswind of 8.0 m/s at 30 degrees (Beaufort 5, fresh breeze); (a) path of the rear wheel contact point (arrow indicates the wind direction) (b) bicycle roll angle (blue) and steer angle (red) as a function of time.

Table 2.1: Mass, damping and stiffness matrices of Equation 2.1 for the bicycle model from Figure 2.1, together with some kinematic bicycle parameters; wheelbase  $w$ , front wheel trail  $c$ , head angle  $\psi$ , and gravity acceleration  $g$ , and rider control feedback gains  $\mathbf{K}_c$  for a forward speeds  $v$ ; all in SI units, from [14].

$$\mathbf{M}_0 = \begin{bmatrix} 133.31668525 & 2.43885691 \\ 2.43885691 & 0.22419262 \end{bmatrix}, \quad \mathbf{C}_1 = \begin{bmatrix} 0 & 44.65783277 \\ -0.31500940 & 1.46189246 \end{bmatrix},$$

$$\mathbf{K}_0 = \begin{bmatrix} -116.73261635 & -2.48042260 \\ -2.48042260 & -0.77434358 \end{bmatrix}, \quad \mathbf{K}_2 = \begin{bmatrix} 0 & 104.85805076 \\ 0 & 2.29688720 \end{bmatrix},$$

$$\mathbf{K}_c = [28.22, -3.19, 41.51, -2.9979, 47.8354], \quad v = 4.25 \text{ m/s}$$

$$w = 1.0759 \text{ m}, \quad c = 0.0718 \text{ m}, \quad \epsilon = 20.1 \text{ deg}, \quad g = 9.81 \text{ m/s}^2$$

## 2.6. Conclusions

Crosswind in bicycling has a considerable effect on the stability and control of the bicycle. Our model simulations show that the tendency of an uncontrolled bicycle under the influence of crosswind is to steer into the wind. In addition, crosswind can decrease the stable forward speed range of an uncontrolled bicycle, and with increasing wind speed can even make an initially stable uncontrolled bicycle, unstable for all forward speeds<sup>1</sup>. Crosswind in a controlled bicycle increases the rider control effort considerably, due to a constant steer torque that has to be applied in order to keep the bicycle at a straight heading. These preliminary results clearly show that crosswind is a serious safety issue in bicycling.

## References

- [1] P. Debraux, F. Grappe, A. V. Manolova, and W. Bertucci, *Aerodynamic drag in cycling: methods of assessment*, Sports Biomechanics **10**, 197 (2011).
- [2] J. Godthelp and M. Buist, *Stability and manoeuvrability characteristics of single track vehicles*. (Soesterberg, Intitute for Reception TNO, 1975, 30 cm., 86 p., fig., graph ..., 1975).
- [3] N. Barry, D. Burton, T. Crouch, J. Sheridan, and R. Luescher, *Effect of crosswinds and wheel selection on the aerodynamic behavior of a cyclist*, Procedia Engineering **34**, 20 (2012).
- [4] N. Barry, D. Burton, J. Sheridan, M. Thompson, and N. A. Brown, *Aerodynamic drag interactions between cyclists in a team pursuit*, Sports Engineering **18**, 93 (2015).

<sup>1</sup>Due to the fact that a bicycle is stable or not the word "resonance" could have been used instead of "unstable" to refer to the effect of certain wind speeds on the bicycle dynamics.

- [5] M. Belloli, S. Giappino, F. Robustelli, and C. Somaschini, *Drafting effect in cycling: Investigation by wind tunnel tests*, *Procedia Engineering* **147**, 38 (2016).
- [6] B. Blocken and Y. Toparlar, *A following car influences cyclist drag: CFD simulations and wind tunnel measurements*, *Journal of Wind Engineering and Industrial Aerodynamics* **145**, 178 (2015).
- [7] B. Blocken, Y. Toparlar, and T. Andrianne, *Aerodynamic benefit for a cyclist by a following motorcycle*, *Journal of Wind Engineering and Industrial Aerodynamics* **155**, 1 (2016).
- [8] C. Kyle and M. Weaver, *Aerodynamics of human-powered vehicles*, *Proceedings of the Institution of Mechanical Engineers, Part A: Journal of Power and Energy* **218**, 141 (2004).
- [9] P. Schepers and K. K. Wolt, *Single-bicycle crash types and characteristics*, *Cycling Research International* **2**, 119 (2012).
- [10] J. P. Meijaard, J. M. Papadopoulos, A. Ruina, and A. L. Schwab, *Linearized dynamics equations for the balance and steer of a bicycle: a benchmark and review*, in *Proceedings of the Royal Society of London A: Mathematical, Physical and Engineering sciences*, Vol. 463 (The Royal Society, 2007) pp. 1955–1982.
- [11] D. Fintelman, M. Sterling, H. Hemida, and F.-X. Li, *The effect of crosswinds on cyclists: an experimental study*, *Procedia Engineering* **72**, 720 (2014).
- [12] A. L. Schwab, P. D. L. de Lange, R. Happee, and J. K. Moore, *Rider control identification in bicycling using lateral force perturbation tests*, *Proceedings of the Institution of Mechanical Engineers Conference, Part K: Journal of Multibody Dynamics* **227**, 390 (2013).
- [13] J. P. Meijaard, *The loop closure equation for the pitch angle in bicycle kinematics*, in *Proceedings of Bicycle and Motorcycle Dynamics Conference* (2013).
- [14] J. K. Moore, J. G. Kooijman, A. L. Schwab, and M. Hubbard, *Rider motion identification during normal bicycling by means of principal component analysis*, *Multibody System Dynamics* **25**, 225 (2011).

# 3

## The dynamic response of the bicycle rider's body to vertical, fore-and-aft and lateral perturbations

Corresponding article: G. Dialynas, J. W. de Haan, A. C. Schouten, R. Happee, A. L. Schwab, The dynamic response of the bicycle rider's body to vertical, fore-and-aft and lateral perturbations, Proceedings of the Institution of Mechanical Engineers, Part D: Journal of Automobile Engineering, (2019), <https://doi.org/10.1177%2F0954407019891289>.

### 3.1. Abstract

The objective of this study was to identify the dynamic response of the bicycle rider's body during translational perturbations, in an effort to improve two-wheeler safety and comfort. A bicycle mock-up was equipped with sensors measuring three-dimensional seat and trunk accelerations and rider's force responses at the seat, handlebars, and footpegs. The bicycle mock-up was driven by a hexapod motion platform that generated random noise perturbations in the range of 0–10 Hz. Twenty-four healthy male adults participated in this study. Responses are represented as frequency response functions capturing three-dimensional force interactions of the rider's body at the seat, handlebars and footpegs in terms of apparent mass, and rider's trunk motion (one-dimensional) as function of seat motion as seat-to-sternum transmissibility. Results showed that the vertical and longitudinal apparent mass for most of the bicycle interfaces followed the resonance of the seat-to-sternum transmissibility. A twice as high magnitude was observed at

the resonance, although a more heavily damped system was apparent in the seat-to-sternum transmissibility. Resonant frequencies were considerably higher in the vertical direction compared to the longitudinal direction. Different dynamics were observed for the lateral measurements, where all magnitudes decreased after the base frequency, and no resonance was observed.

**Keywords**

Bicycle dynamics, rider identification, whole-body vibration, apparent mass, transmissibility.

## 3.2. Introduction

In cycling the rider's mass is much larger than the vehicle mass. Hence, the rider can contribute considerably to the dynamic behaviour of the bicycle, not only by means of voluntary control actions, but also by means of the passive response of his/her body to bicycle oscillations. The rider's body consists of inertial and visco-elastic properties that interact with the bicycle and affect the dynamic response of the combined system. The stabilization of dangerous oscillatory two-wheeler modes such as weave [1] and wobble [2] can be influenced by the rider's biomechanical properties. Therefore, a biomechanical model with human-like properties needs to be included to study the dynamic behaviour of the combined bicycle-rider system.

In the automotive field the biodynamic response characteristics of seated subjects exposed to whole body vibration (WBV) have been extensively reported in terms of apparent mass (APMS). Fairley and Griffin [3] measured the APMS of seated humans with and without backrest in the fore-aft and lateral directions. Mansfield and Lundström [4] measured the APMS of seated humans exposed to non-orthogonal horizontal vibrations. Rakheja et al. [5] and Toward and Griffin [6] measured the APMS of seated humans under automotive postures hands-in-lap (e.g. passengers) and hands-on-steering wheel (e.g. drivers) in the vertical direction. Toward and Griffin [7] measured the vertical APMS of seated humans for four different backrest conditions. Wang et al. [8] and Kim et al. [9] reported the vertical APMS for different sitting postures and seat designs. Gao et al. [10] conducted similar experiments as Toward and Griffin [7]. A simple two-mass-lumped model was adopted to describe the vertical vibration characteristics of the seated human body. The APMS predicted by the established model agreed very well with those obtained from experiments. In general, body mass dependent models are successful in predicting the apparent mass and transmissibility responses of a seated human body [11]. The driving point mechanical impedance, seat-to-head transmissibility and apparent mass are the principal characteristics used to describe the biodynamic response of a seated human body under WBV in the automotive sector. The apparent mass is popular, as it is straightforward in physics and can be measured conveniently. A review on the fundamentals of biomechanical modelling of the human body in transport systems is presented by Wieckowski [12].

In the field of two-wheelers no study was found reporting the APMS of seated rider's

exposed to translational perturbations. Most related studies in the open literature focus on the rotational motions and measure different biodynamic characteristics. Katayama et al. [13] measured the center of mass and moment of inertia for normal and forward-leaning riding positions and proposed two different biomechanical models to describe the motions of rider's body without his control actions. One of these models has two degrees-of-freedom (DOF) concerning leaning motion of the trunk and lateral movement of the lower trunk, the other model describes the yaw motions of upper and lower body segments. These models, however, have not yet been validated. Cossalter et al. [14] generated steer torque perturbations using a motorcycle simulator to identify the visco-elastic properties of the rider's arms (i.e. steering impedance) and trunk. A two DOF model was adopted for this purpose, but the coefficient of variation (ratio of the standard deviation to the mean) of the identified arm properties was quite large. The variations were possibly due to differences in the physique and riding experience of the participants. Doria and Tognazzo [15] generated yaw perturbations using a motorcycle mock-up and developed two biomechanical models to simulate the response of the rider to yaw and steer oscillations. Predictions of the one DOF model were successful below 4 Hz, whereas the two DOF model captured the whole frequency bandwidth of 0-10 Hz. The identified values of stiffness and damping of waist and arms were in good agreement between the two models. Doria et al. [16] and Doria and Tognazzo [17] used a motorcycle mock-up and a bicycle mock-up to generate roll perturbations and measured the rider's trunk lean stiffness and steering impedance. Biomechanical models with up to five DOF have been used in the first study, whereas in the second study a similar approach to the one of Schwab et al. [18] was followed to model and analyse effects of the passive response of the rider's body on the stability of a bicycle. Similar results with Doria and Tognazzo [15] were observed for the one, two and three DOF models. The five DOF model which included a detailed description of the arms stiffness and damping properties was able to simulate accurately both the lean and torque FRFs responses.

The aim of this study is to identify the dynamic response of the rider's body at all interfaces and in all three translational directions. The response of the rider's body is represented in the frequency domain by means of frequency response functions (FRFs). More specific, the interaction of the rider's body in the seat, handlebars and footpegs is expressed in terms of APMS and as seat-to-sternum transmissibility (STST) functions. The paper is organized as follows: First, the experimental set-up, the perturbation signal design and experimental procedure are presented. Next, the results, including STST and APMS, are presented. The article ends with a discussion and conclusion section highlighting the main findings.

### 3.3. Methods

#### 3.3.1. Description of experimental set-up

To identify the rider's body response to whole body vibration a dedicated modular experimental set-up was developed, consisting of a custom made bicycle mock-up placed on an industrial high-end hexapod, see Figure 3.1 (a). The experimental

set-up is able to perturb and monitor the rider's body in a wide frequency range (0-12 Hz), while keeping the rider in an upright riding posture similar to that of a city bike. The mechanical structure of the bicycle mock-up consists of standard bicycle parts and steel tubes held together with aluminum clamps. The steering assembly is fixed and the footpegs are placed symmetrically in order to obtain comparable results between the two sides. The geometry of the bicycle mock-up is based on the dutch city bike Batavus Browser (56 cm). The fundamental geometrical dimensions of the constructed frame, together with a seated rider are presented in Figure 3.1 (b): (D) declares the seat post inclination which is 72 deg, (E) is the head angle which is 12 deg, (TT) is the top tube length which is 68 cm, (RTH), (STH) are the reach and stack to handlebars dimensions which are 44 cm and 75 cm, respectively. The average seated rider had an upper trunk inclination (A) of approximately 20 deg, a knee (B), and ankle angle (C) of about 90 and 75 deg, respectively. The later applies to the body build of the 95% of the male European population [19].

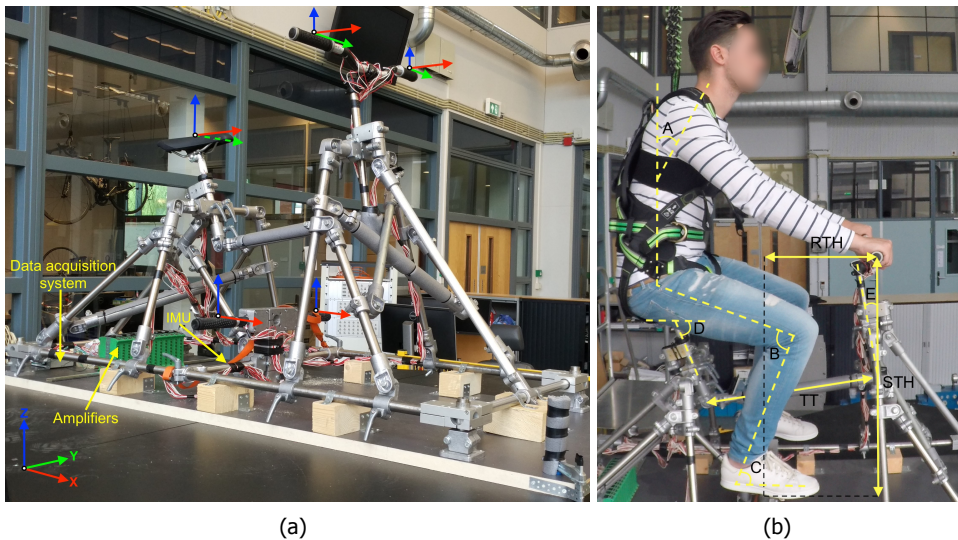


Figure 3.1: Bicycle mock-up without and with seated rider, (a) location of sensors and amplifiers, (b) basic frame dimensions, anthropometric rider measurements and safety harness.

The bicycle mock-up is equipped with an inertial measurement unit (IMU) and a total of 13 full-bridge strain gauge sensors in half-bridge configuration to measure the motion and the forces at the interfaces. Six half-bridges are located at each handlebar, four at each footpeg and six at the seatpost. A side view of the locations of the half-bridges is shown in Figure 3.2. With the strain gauge configuration, the rider's force responses in all interfaces and directions can be measured (except for the footpegs forces in lateral Y-axis, where no relevant force responses are expected). Laboratory tests were performed to determine the optimal location of the strain gauges on the handlebars, minimizing the potential geometrical and crosstalk effects. For instance, the strain gauges that measure the vertical and

longitudinal applied handlebar loads (i.e. Z, X-axis) were placed immediately after the tapered clamping area. On the other hand, the strain gauges that measure the lateral applied handlebar loads (i.e. Y-axis) were placed near the grips to avoid any geometrical artifact due to the handlebar curvature, see Figure 3.2 (a). The footpeg and saddle strain gauges were placed as close as possible to the mounting area of the bicycle frame, see Figure 3.2 (b) and (c). Crosstalk, the influence of forces from the non-measuring direction, was subtracted from the strain gauge measurements.

3

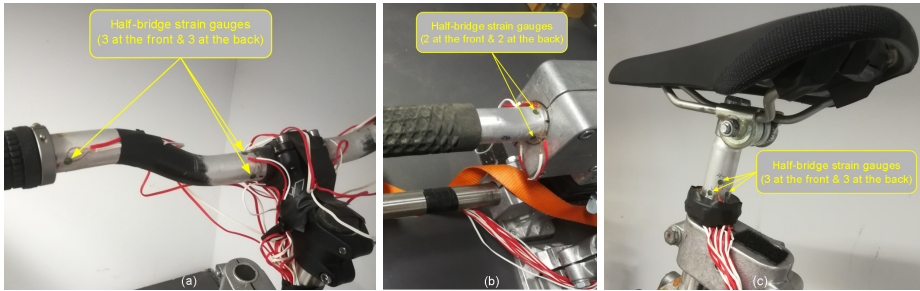


Figure 3.2: Locations of the strain gauges at all bicycle interfaces, (a) left handlebar, (b) left footpeg, and (c) seatpost.

A data acquisition system from National Instruments (LabVIEW) and MTW Awinda (Xsens software) sampled the strain gauges and IMU signals at 100 Hz. The bicycle mock-up was mounted on the top of a hexapod from E2M Technologies. The hexapod provides a sufficient response up to around 10 Hz; for higher frequencies there was observable latency in the system. The perturbation signals were designed in Matlab and were implemented in the platform using the eMove eM6-670 electric motion system of the hexapod.

### 3.3.2. Perturbation signal selection and design

In the automotive field, random noise oscillations with different bandwidths and magnitudes are typically applied to identify the APMS of seated humans. Fairley and Griffin [3] used random noise perturbations in which the frequency bandwidth was limited between 0.25-20 Hz, the acceleration spectral density was flat  $\pm 5\%$  and the maximum magnitude was set  $1 \text{ ms}^{-2}$  rms. Toward and Griffin [6, 7] and Gao et al. [10] used random noise perturbations with a duration of 60 seconds and a maximum acceleration magnitude of  $1 \text{ ms}^{-2}$  and  $2 \text{ ms}^{-2}$  rms, respectively. The frequency bandwidth was limited using 8-pole Butterworth filters between 0.13-40 Hz, 0.125-25 Hz and 1-20 Hz, respectively.

In the field of two-wheelers frequency sweep perturbations are commonly used to excite the seated rider. Cossalter et al. [14] used steer sine-sweep excitations with a duration of 200 seconds, a mean amplitude of 2 deg and a frequency range 0.5-12 Hz. Doria et al. [15] used yaw sine-sweep excitations with a duration of 115 seconds, a mean amplitude of 2 deg and frequency range 0.5-10 Hz. Doria

et al. [16, 17] used roll sine-sweep oscillations initial amplitude was set to 1.5 deg, duration and frequency range remained the same as previous study. To avoid non-linear rider behaviour, the amplitude was decreased at higher frequencies by dividing with the square root of the instantaneous angular frequency.

In general, an optimal perturbation signal requires prior knowledge of the system and its corresponding noise characteristics [20]. Since the dynamics of the passive bicycle-rider system are unknown, filtered white-noise was selected to excite the rider's body. A 5-pole Butterworth filter with a cut-off frequency of 9 Hz was used to filter the white-noise signal. With the filter the signal is concentrated in the frequency bandwidth 0-9 Hz and thereby improving the SNR. The maximum perturbation amplitudes and rms for the translational signals were selected based on naturalistic cycling data collected from Ouden and Schwab [21], see Table 3.1.

Table 3.1: Amplitudes of perturbation signals in the three directions including mean ( $\mu$ ) and root mean square (*rms*) values.

	Heave Z (m/s <sup>2</sup> )	Surge X (m/s <sup>2</sup> )	Sway Y (m/s <sup>2</sup> )
Van den Ouden	1.0	1.5	1.0
max. amplitudes	1.0	0.75	0.75
mean	4.25e-05	-2.62e-04	-6.11e-04
rms	0.33	0.25	0.25

For safety and comfort, the acceleration of all perturbation signals was limited to 1 ms<sup>-2</sup> rms. The selected frequency bandwidth includes the oscillation frequencies of dangerous oscillatory modes such as weave (0-4 Hz) and wobble (0-9 Hz) observed by Meijaard et al. [1] and Plöchl et al. [2]. The final coloured noise PVA signals were designed to have a duration of 60 seconds. The filtered white noise signals had a duration of 60 seconds, see Figure 3.3 as an example of the heave acceleration signal  $p(t)$ .

### 3.3.3. Procedure

Twenty-four healthy men (mean age =  $26 \pm 3$  years, weight =  $81.7 \pm 7.4$  kg, height =  $181 \pm 7$  cm) volunteered in this study. To assure safety a full body safety harness was used as a fall arrest system during the experiments<sup>1</sup>. All participants gave informed consent according to the guidelines of the human research ethics committee of the Delft University of Technology. Women were not included due to their different body build. Participants self reported that they did not experience any kind of pain or injury in the year before the experiments. The mean weight of the participants was selected to be close to the European population [22], whereas the height is close to the mean height of young European men [23].

<sup>1</sup>The participants were commanded to sit on the bicycle mock-up as they normally do when riding their bicycles and look at the horizon in front of them. During the experiments it was evident that the participants tried to constrain their torso movement by consciously increasing their stiffness and damping properties of their arms, legs and torso. Preliminary trials indicated volunteer transient movements below 1 Hz. For this reason fade-in and fade-out periods were applied as explained later in this section.

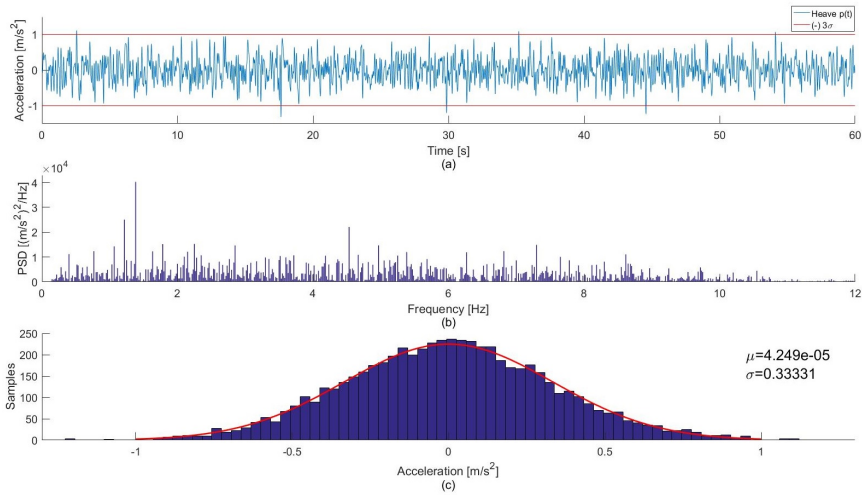


Figure 3.3: Profile of heave acceleration signal  $p(t)$ , (a) signal in the time domain (red lines indicate  $\mu-3\sigma$  and  $\mu+3\sigma$ ), (b) acceleration spectral density and (c) amplitude distribution.

Each experimental trial had a duration of 69 seconds consisting of a 4.5 seconds fade-in period, 60 seconds perturbation signal  $p(t)$ , and a 4.5 seconds fade-out period. The fade-in and fade-out periods were included to minimize transient behaviour and to prevent abrupt platform motions. Two repetitions of the same trial were performed for every motion<sup>2</sup>. Repeatability was good between the two trials for all acceleration and force measurements (standard error of the mean (SEM) was kept to  $\pm 8\%$ ). The results from both trials were averaged and shown in the frequency domain analysis.

## 3.4. Data recording and processing

### 3.4.1. Subjective measures

The participants completed a subjective assessment immediately after finishing the experiment. A NASA "Raw-TLX" questionnaire was used to evaluate the perceived workload, effectiveness and other aspects of performance [24]. The NASA-TLX includes six sub-scales with scores ranging from 0-100%, from which the experimental workload is assessed.

### 3.4.2. Static and dynamic force measurements

For each motion the static forces and dynamic forces in the time domain are used as a measure to indicate dominant force directions at the three interfaces. The static force is a measure of the gravitational forces that the rider's body mass exerts at all bicycle interfaces and is calculated as the average of the mean force over the participants. The dynamic force is a measure of behaviour during the experimental

<sup>2</sup>A relaxation period of approximately two minutes was given to all participants between the trials.

trials and is computed as the rms of the force signal, see Table 3.2.

### 3.4.3. Transfer functions

The block diagram of the motion platform combined with the passive rider is presented in Figure 3.4, where  $p(t)$  is the input perturbation signal to the motion platform  $E(t)$ ,  $u(t)$  is the input to the passive rider  $H(t)$ ,  $n(t)$  is additional noise and  $y(t)$  is the rider output response. Note that the rider cannot influence the motion of the platform, as would be possible with a normal bike.

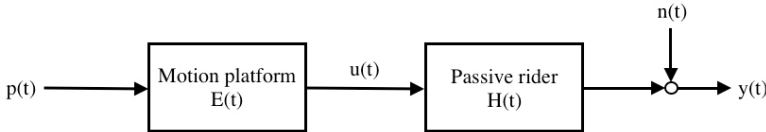


Figure 3.4: Block diagram of motion platform combined with passive rider system.

The dynamics of the rider are described based on the input-output relationship of the measured signals in the frequency domain. The STST and APMS are defined as ratios and calculated as transfer functions using the cross-spectral density (CSD) method defined by Mansfield et al. [25] and Griffin [26]:

$$TF_{CSD}(f) = \frac{CSD_{input-output}(f)}{PSD_{input}(f)} \quad (3.1)$$

The linear correlation between the input and output is expressed in terms of the coherence, see Equation 3.2. Coherence ranges from 0 to 1, where one reflects a perfect, noise-free linear relation.

$$Coherence(f)^2 = \frac{|CSD_{input-output}(f)|^2}{PSD_{input}(f) \times PSD_{output}(f)} \quad (3.2)$$

The transfer functions of the STST and APMS of the rider's body are estimated using Welch' method in which the spectral densities are averaged over 10 segments [27]. The dynamic responses of the left and right handlebar and footpeg side appeared symmetrical, therefore the results of the left and right side are merged as the mean resultant forces and APMSs. The mean magnitude and SD is calculated over all subjects, however for the phase a different approach is used. The mean phase is calculated by taking the angle of the average complex number, whereas the SD by estimating the circular standard deviation. The SD is displayed as a shaded area around the mean line. The coherence significance level (CSL)<sup>3</sup> is shown as a dashed line in the coherence plots. A Hanning window with 50% segment overlap

<sup>3</sup>The CSL indicates the threshold above which the coherence is significantly different from zero and is calculated as;  $CSL = 1 - (1 - \alpha)^{1/(L_{seg} - 1)}$  in which  $\alpha$  is the significance level and  $L_{seg}$  is the number of independent segments. A probability of making a Type I error is set for our hypothesis test.

is used to prevent frequency leakage and the 5 independent segments results in a CSL of 0.53 with probability  $p < 0.05$  [28]. The SD demonstrates the variability in the behaviour between the participants, whereas CSL underlines the confidence interval of the spectral estimator.

#### 3.4.4. Seat-to-sternum transmissibility (STST)

Measurement of the transmission of vibration between the bicycle mock-up and rider's upper body is expressed in terms of transmissibility. Transmissibility  $T(f)$  is defined as the ratio of the acceleration at a point on the body to the acceleration at the base of the mock-up:

$$T(f) = \frac{a_{body}(f)}{a_{base}(f)} \quad (3.3)$$

To measure the transmissibility an additional IMU was mounted on the rider's sternum, see Figure 3.5 for the exact locations of the two IMUs. The IMU of the rider's sternum was placed between two elastic stretch bands to avoid local displacements due to skin movements. Because that the accelerations of the bicycle base and seat are identical, the term STST is used herein to express the acceleration transmissibility measurements between the seat base and rider's sternum. For all motions the acceleration measurements were transformed to the inertial reference frame, all sign conventions follow the right-handed Cartesian coordinate system, see Figure 3.5. In other words, all accelerations are positive in the forward (X-axis), left (Y-axis) and upward direction (Z-axis), respectively.

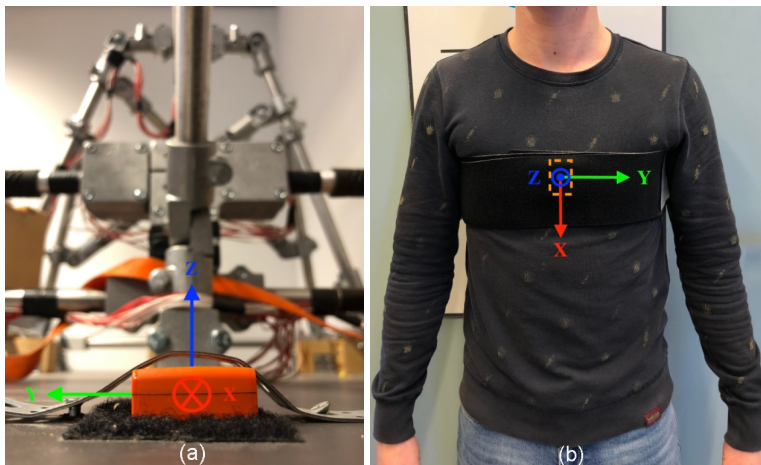


Figure 3.5: Locations of the IMUs with right-handed Cartesian coordinate system, (a) back view of motion platform and (b) front view of rider's sternum.

### 3.4.5. Apparent mass (APMS)

The measurement of the transmission of forces between the rider's body and the bicycle interfaces is expressed in terms of apparent mass<sup>4</sup>. Apparent mass  $M(f)$  is defined as the ratio of the applied force at the interfaces to the acceleration at the base of the mock-up at a frequency ( $f$ ), see Equation 3.4.

$$M(f) = \frac{F(f)}{a(f)}, \quad (3.4)$$

For all motions the APMS measurements follow the sign conventions of the right-handed Cartesian coordinate system, see Figure 3.1 (a). This implies that all forces exerted from the bicycle to the rider are positive in the forward (X-axis), left (Y-axis) and upward direction (Z-axis), respectively.

## 3.5. Results

### 3.5.1. NASA-TLX

Results of the NASA-TLX are summarized in Figure 3.6. Two clusters can be identified when correlating the performance and effort scale. The first cluster (16 subjects) indicates high performance (> 50%) with low effort (< 40%). The second cluster (8 subjects) indicates high workload with poor performance. The scores of the second group are indicated with black markers in Figure 3.6 and also explain the outliers in mental demand and frustration. There were no differences between the groups in the STST and APMS (see supplementary material, STST\_individual figure). The results of the subjective workload scores show the highest score for performance (83% median), and the lowest score for frustration (8% median). Mental, physical, temporal and effort demand score between 13-25% median reflecting the passive nature of the experiments<sup>5</sup>.

### 3.5.2. Static and dynamic force distribution

Table 3.2 presents the static and dynamic force distribution at all bicycle interfaces and directions. The large ratio between the static and dynamic forces indicates that the magnitude of the (static) gravitational forces is much larger than the magnitude of the forces resulting from the dynamic perturbations. Due to bicycle geometry and rider posture, symmetry is expected in the dynamic force distribution at the ZX, ZY-plane for all motions. To indicate symmetry the dynamic force distribution matrix was decomposed into a symmetric and an asymmetric part (see supplementary material, Table 3). The symmetric part was calculated by taking the mean of the dynamic force cross-terms (ZX, ZY, XY) for every motion, whereas, the asymmetric part by subtracting the latter from the dynamic force part.

<sup>4</sup>Apparent mass is derived as ratio of force and acceleration with a frequency dependent gain and phase. Hence the apparent mass captures body inertial properties as well as stiffness, damping and neuromuscular feedback.

<sup>5</sup>The idea here was to have a subjective assessment of the mental, physical, temporal and effort demand in order to evaluate passive or active control behaviour. A better approach could have been to use electromyography (EMG) to evaluate maximal voluntary contraction (MVC) as a percentage.

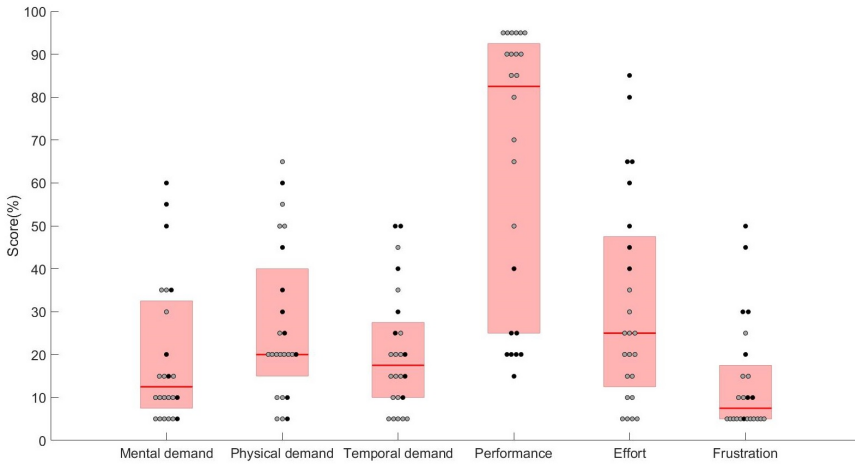


Figure 3.6: Boxplots of the NASA Task Load Index (TLX) scores for 24 participants.

For heave and surge the interactions at the seat (SP) indicated higher correlation in the ZX-plane compared to the ZY-plane, symmetric coefficients were 7.5 and 3.5, respectively. Correlation was also higher in the ZY-plane compared to the XY-plane for the surge and sway motion, coefficients were 3.5 and 2.5 for the former and latter plane. Footpegs (FP) showed perfect symmetry, and handlebars (HB) had a symmetric correlation coefficient of 1.5 for all planes and bicycle motions.

For heave, dynamic forces are mainly observed at the seat (SP<sub>Z</sub>) followed by the footpegs (FP<sub>Z</sub>) and the handlebars (HB<sub>Z</sub>). The forces in the longitudinal direction of the seat (SP<sub>X</sub>) are mainly due to the bicycle geometry, while the forces in the lateral direction of seat (SP<sub>Y</sub>) are probably due to asymmetry of the human body. The lateral forces in the left (HB<sub>LY</sub>) and right handlebar (HB<sub>RY</sub>) might be a result of lateral handlebar deformation induced by the vertical and longitudinal applied forces.

For surge, dynamic forces are generated in the longitudinal (SP<sub>X</sub>) and vertical (SP<sub>Z</sub>) direction of the seat, followed by the handlebars (HB<sub>X</sub>) and (HB<sub>Z</sub>). Footpegs show similar forces at the longitudinal (FP<sub>X</sub>) and vertical (FP<sub>Z</sub>) directions. Forces in the vertical direction are presumably a result of rider posture and anterior/posterior trunk movements.

For sway, dynamic forces are present in the lateral seat direction (SP<sub>Y</sub>) followed by (SP<sub>Z</sub>) and (SP<sub>X</sub>). At the footpegs and handlebars forces are more dominant at the vertical direction. It is evident that the rider co-activates his leg and arm muscles (i.e. vertical foot and handlebar forces) to reduce side-to-side swing of his trunk effectively.

Table 3.2: Static (S) and dynamic forces (D) at the seat (SP), footpegs (FP) and handlebars (HB) for heave, surge and sway motion.

Interface	Heave (Z)		Surge (X)		Sway (Y)	
	S (N)	D (N)	S (N)	D (N)	S (N)	D (N)
SP <sub>Z</sub>	579	24	571	11	569	6
SP <sub>X</sub>	66	4	63	12	66	4
SP <sub>Y</sub>	22	1	28	1	30	11
FPL <sub>Z</sub>	89	4	90	1	90	2
FPL <sub>X</sub>	17	1	16	1	16	1
FPR <sub>Z</sub>	87	4	89	1	86	2
FPR <sub>X</sub>	17	1	16	1	16	1
HBL <sub>Z</sub>	40	2	41	2	41	2
HBL <sub>X</sub>	14	1	15	3	15	2
HBL <sub>Y</sub>	42	1	51	1	41	1
HBR <sub>Z</sub>	39	2	38	2	38	2
HBR <sub>X</sub>	16	1	16	3	16	2
HBR <sub>Y</sub>	33	1	34	1	28	1

### 3.5.3. STST

The STST for all motions are presented in Figure 3.7. For the heave motion, coherence is significant ( $p < 0.05$ ) for all frequencies. The magnitude of the STST increases after 1.5 Hz and reaches a resonant peak at 5 Hz. The phase of the trunk leads from 0.17-4.8 Hz and lags for all other frequencies.

For the surge motion, coherence is significant ( $p < 0.05$ ) between 0.33-11.5 Hz. The magnitude of the STST increases after 0.8 Hz and reaches a resonant peak at 2 Hz. The phase of the trunk flips above 0.33 Hz and continues to lead up to 2 Hz, next the phase lags up to 8 Hz. For both motions the rider's trunk accelerations exceed seat accelerations by a factor of 2.

For the sway motion, coherence is significant ( $p < 0.05$ ) between 0.33-8 Hz. At 0.33 Hz the acceleration of the trunk is approximately three times higher (magnitude = 2.8) than the seat. Between 1-8 Hz the acceleration of the trunk is lower (magnitude < 1) than the seat. The phase lag suggests that participants try to restrain the sway of the upper trunk. Participants used postural control to restrain excessive movements and prevent falling off the seat.

### 3.5.4. APMS

The APMS for the heave motion (Z) are presented in Figure 3.8. All cross-axes are included in the Figure, nevertheless the analysis is mainly focused on the vertical direction (Z-axis), since this is the axis where the most dominant rider forces are present. Coherence is significant ( $p < 0.05$ ) above 0.2 Hz for all APMS, thus this frequency is used as a base to interpret the magnitude and phase responses for this motion. At this base frequency of 0.2 Hz the magnitude is 52.08 kg\* at the seat, 7.13 kg\* at each footpeg and 5.23 kg\* at each handlebar. The sum of all magnitudes at the base frequency is 76.8 kg, which is approximately the mean rider's weight.

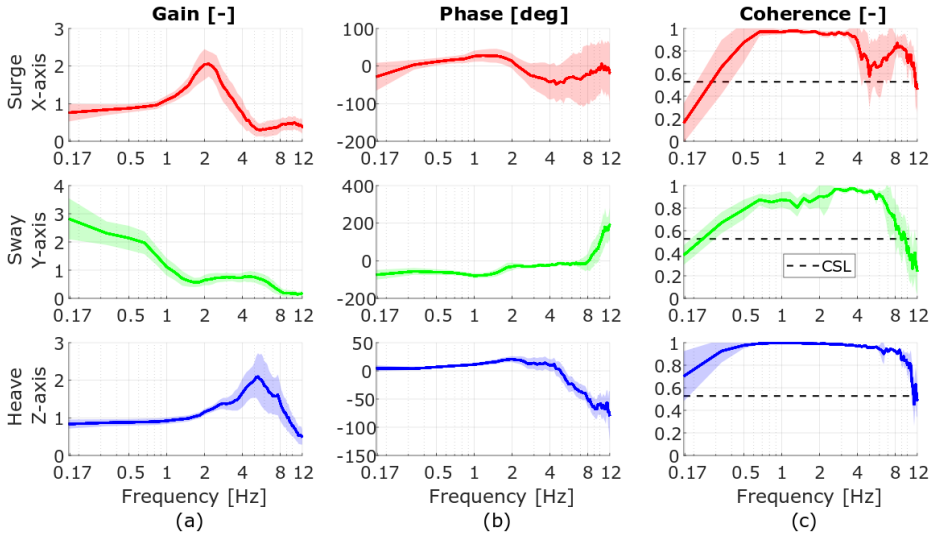


Figure 3.7: Seat-to-sternum transmissibility (STST) for heave (Z, Vertical), surge (X, longitudinal) and sway (Y, lateral) motions as a function of the applied frequency ( $f$ ), (a) gain, (b) phase and (c) coherence, shade = SD over participants, coherence is significant above the dashed line.

The vertical and longitudinal APMSs are also close to the static loads, see Table 3.2. The magnitudes at the seat and handlebars show a resonant peak at 5 Hz, which matches the resonance of the STST, whereas that of the footpegs is 6.3 Hz. All magnitudes above the primary resonance tend to decrease with increasing frequencies. The phase of the seat and footpegs leads between 0.5-4.6 Hz, albeit up to 2 Hz the lead is small and the phase response indicates a mass system. Above 4.6 Hz, the phase of the seat and footpegs lags with a slope of 13.7 deg/Hz. The phase of the handlebars is almost flat up to 4 Hz, onwards the phase lags and flips at 8 Hz (i.e. lag to lead). The magnitude and phase show similar trends for almost all directions and interfaces, except for the handlebars in the longitudinal direction (X-axis) where the phase leads for all frequencies. The large phase lead of the handlebars indicates that the rider exerts forces opposed to the anterior/posterior trunk movements (i.e. provoked due to the vertical motion) to keep his trunk stable in space.

The APMS measurements for the surge motion (X) are presented in Figure 3.9. For surge, most of the dynamic forces are generated in the longitudinal direction (X-axis). Coherence is significant ( $p < 0.05$ ) above 0.33 Hz for all APMS measurements, thus this frequency is used as a base to interpret the magnitude and phase responses for this motion. At this reference frequency of 0.33 Hz the magnitude is 51.2 kg\* at the seat, 3.16 kg\* at the footpegs and 24.71 kg\* at the handlebars. The magnitudes of all interfaces show a resonant peak at 2 Hz, which is the same as the resonance of the STST. At the footpegs and handlebars a second resonant peak occurs at 5 and 7 Hz, correspondingly. The sum of all measured magnitudes

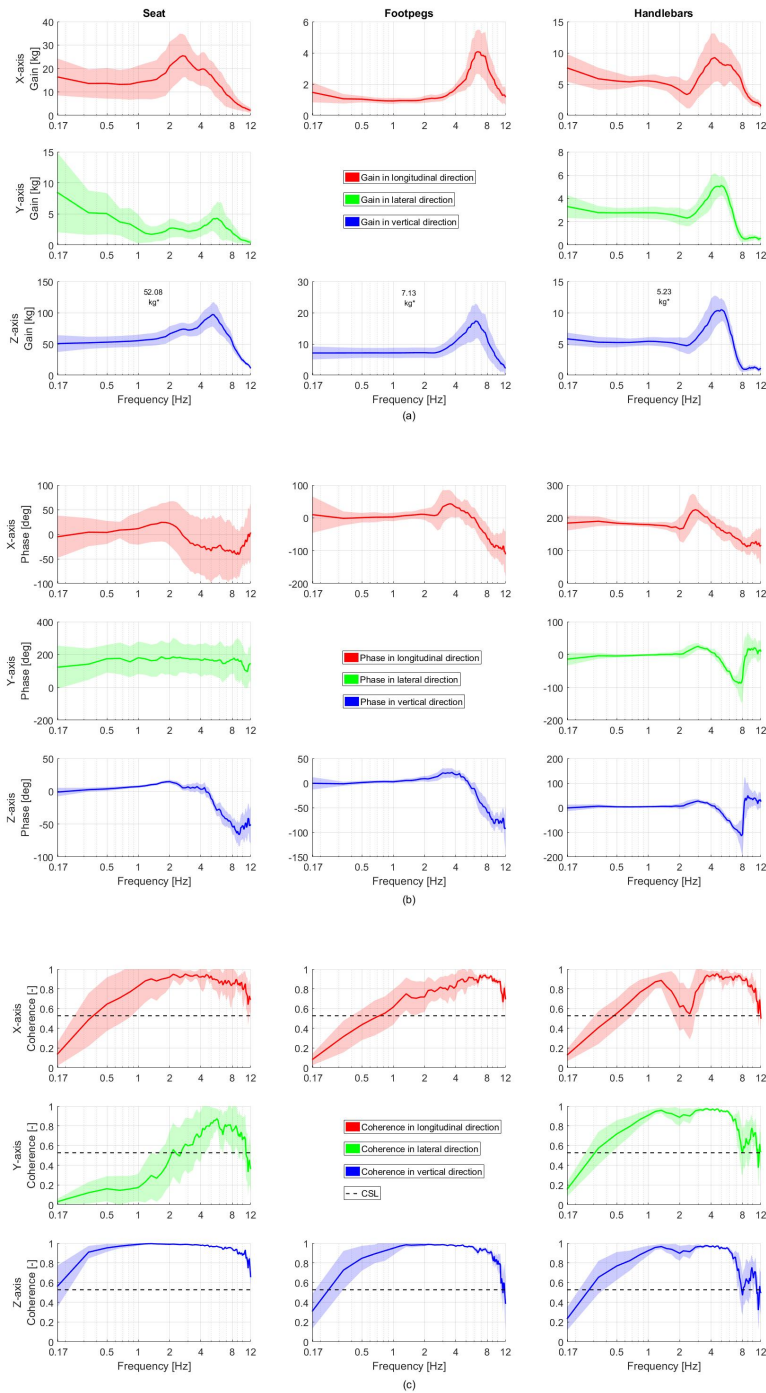


Figure 3.8: Apparent mass (APMS) for the heave (Z, vertical) motions as a function of the applied frequency (f) at the seat, footpegs and handlebars (a) gain, (b) phase and (c) coherence, shade = SD over participants.

at the base frequency exceeds the mean rider's weight, presumably due to phase differences in forces at seat, footpegs and handlebars. The phase response up to 2 Hz indicates a mass system, but this does not apply for all the other frequencies. Onwards, the phase of the seat and handlebars lags up to 7.3 Hz and 10 Hz, respectively. The phase of the footpegs and handlebars flips at 2.8 Hz and at 5.5 Hz, respectively. The phase flips are probably caused due modulation in the control behaviour of the knee and arms. The magnitude and phases show similar trends for almost all directions and interfaces, exception are the footpegs and handlebars in the vertical direction (Z-axis) where the phase leads significantly. Similar to the heave motion the large phase lead of the footpegs and handlebars implies that the rider applies forces oppose to the anterior/posterior pelvis and trunk movements to keep his body stable in space.

The APMS for the sway (Y) motion are presented in Figure 3.10. For sway, most of the dominant dynamics are noticed at the seat (Y-axis), footpegs (Z-axis) and handlebars (X, Z-axis). Coherence is significant above 0.5 Hz ( $p < 0.05$ ) for most of the frequencies. At the base frequency of 0.5 Hz the magnitude at the seat is 205.3 kg, whereas the magnitude of the footpegs and handlebars in the (X, Z-axis) is 8.86 kg, 30.49 kg, 34.86 kg, 30.52 kg, respectively. All magnitudes decrease as the frequency increases, and no resonance is observed for sway motion. The phase of the seat, footpegs and handlebars leads for all frequencies. The vertical and longitudinal directions of the footpegs and handlebar show good coherence, obviously the rider uses his feet and hands to stabilize his pelvis and trunk in space.

### 3.6. Discussion

Here, we measured the dynamics (STST and APMS) of a bicycle rider. To the best of our knowledge, such work has not been presented before. The APMS and STST can be used to create a biomechanical rider model. The addition of a human like model to the Carvallo–Whipple bicycle model [1] is essential to explore unstable oscillatory bicycle modes and improve bicycle safety and comfort. Bicycle comfort could be improved, for example, by designing vibration isolators for the saddle and handlebars, whereas, safety by designing steering stabilizers. The selection of the stiffness and damping properties of these isolators can be obtained by analysing the eigenvalues and eigenmodes of the combined bicycle-rider system. Comfort, safety and performance can now be easily evaluated by running multiple simulations for different bicycle types (e.g. city, racing etc.). The methodology described herein is focused on the translational motions, the dynamic responses of the rider for the rotational motions might differ, even with motions that are considered similar (e.g. sway and roll).

All motions resulted in consistent transmissibility and apparent mass responses over the participants with a relatively high coherence. Therefore the system identification techniques were justified indicating FRF estimates of high quality. Heave and surge motion interacted with each other and showed similar dynamics (i.e. a result of subject leaning forward). Similar forces were observed in the ZX-plane of the seat (SP), footpegs and ZX, ZY plane of the handlebars (HB), see Table 3.2. The

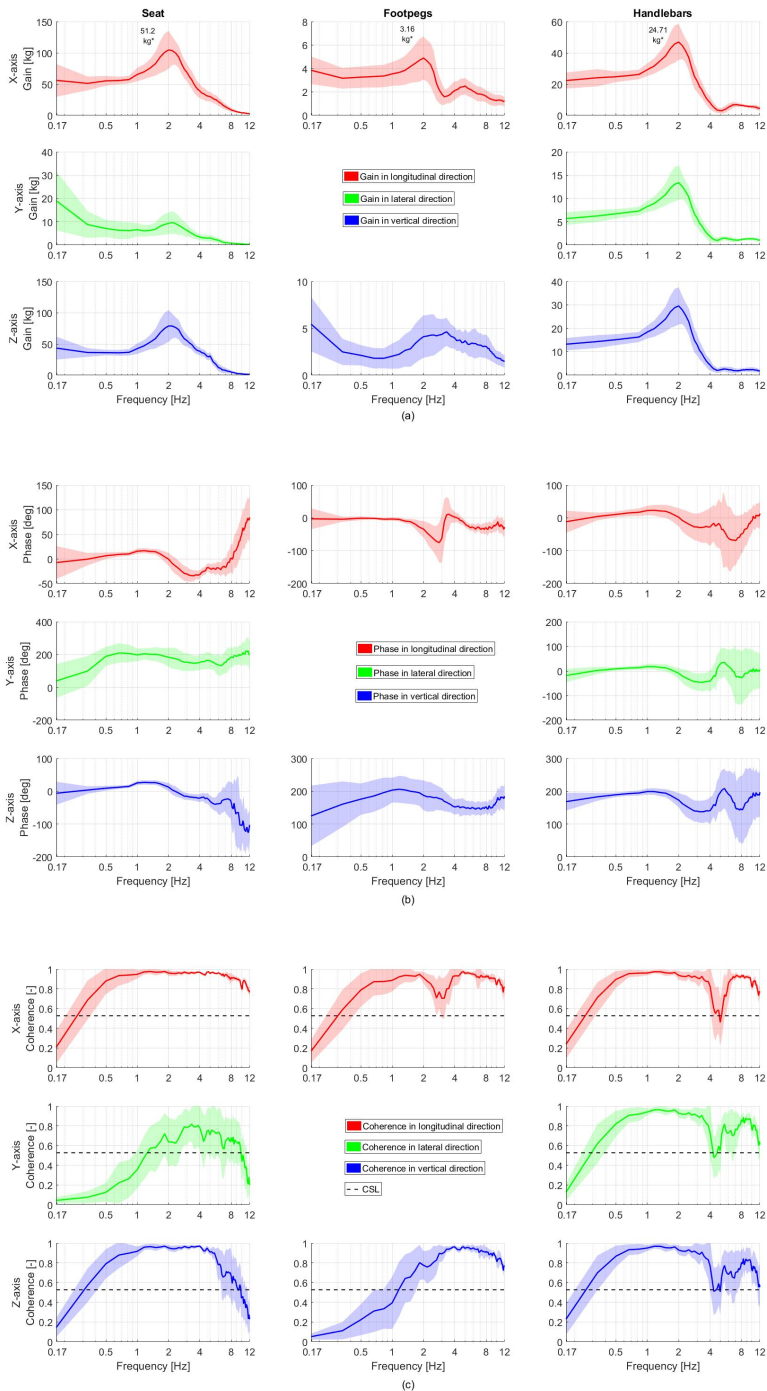


Figure 3.9: Apparent mass (APMS) for the surge (X, longitudinal) motions as a function of the applied frequency (f) at the seat, footpegs and handlebars (a) gain, (b) phase and (c) coherence, shade = SD over participants.

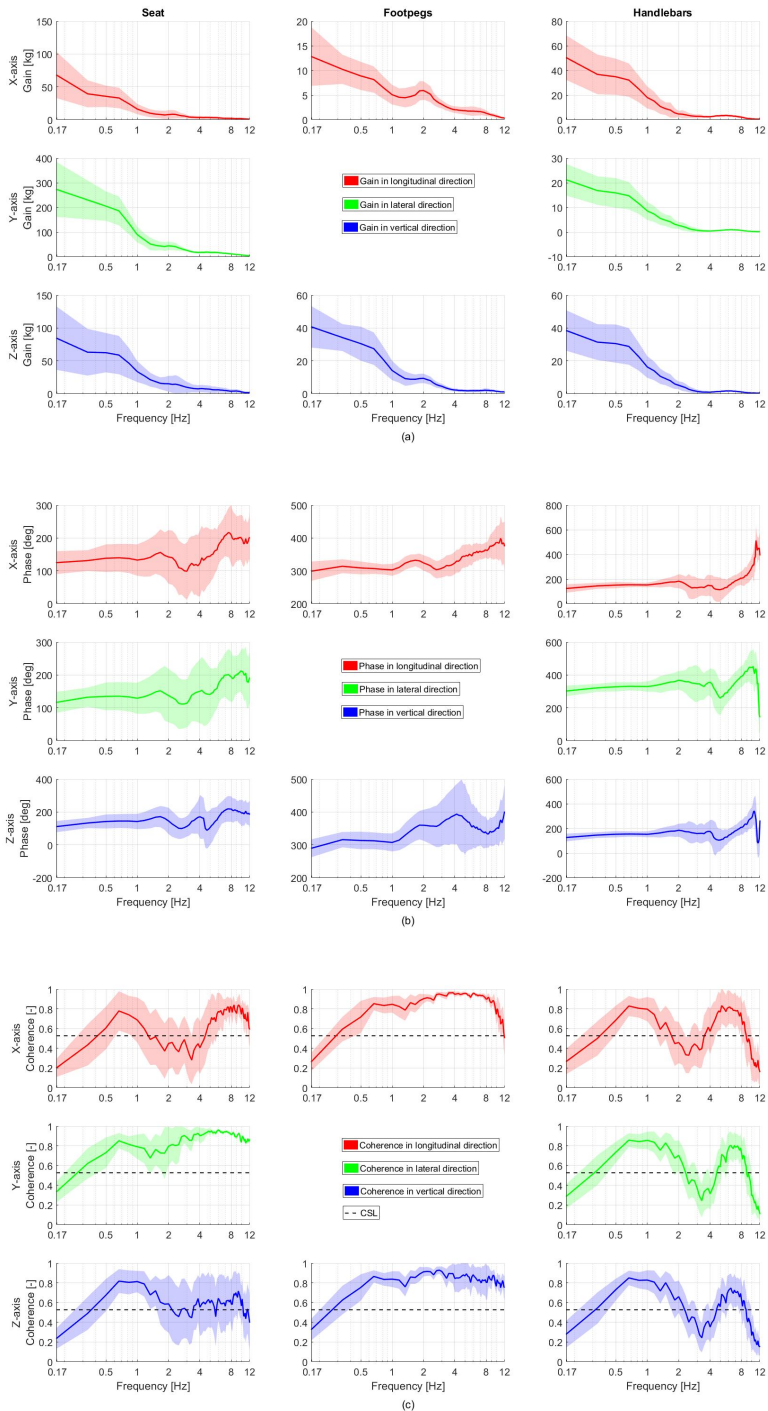


Figure 3.10: Apparent mass (APMS) for the sway (Y, lateral) motions as a function of the applied frequency ( $f$ ) at the seat, footpegs and handlebars (a) gain, (b) phase, and (c) coherence, shade = SD over participants.

vertical STST and APMS of the seat and handlebars showed a resonance at 5 Hz, in agreement with the resonance reported by Toward and Griffin [6, 7] and Mansfield and Griffin [29]. The longitudinal STST and APMS had a resonance at 2 Hz, which is close to the resonance of 2.5 Hz and 2.62 Hz found for male seated subjects without backrest by Fairley and Griffin [3] and Mansfield and Lundström [4], respectively. The small resonant frequency variations could be attributed to different body masses and postures. For instance, higher body mass can lead to higher magnitudes and lower resonance [5, 6]. Holding a steering wheel could lead to lower resonance in respect with hands-in-lap posture as suggested by Wang et al. [8], Rakheja et al. [5] and Toward and Griffin [6]. Sway was independent from the other two motions, the lateral STST and APMS showed similar trends: no resonance was observed and postural control was evident in both measurements.

For heave and surge the rider's body acted as a rigid mass up to 2 Hz. For sway the rider's body behaved like a horizontal mass spring-damper system (pelvis) with a torsional spring inverted pendulum (trunk) on top (see supplementary material, Schematic 1) for all frequencies. The high magnitude APMS ( $> 200\text{kg}$ ) for sway motion were perhaps a result of the angular  $\theta$  trunk dynamics. The upper body center of gravity lies above the saddle requiring roll moments generated by lateral forces at saddle, footpegs and steer. To validate this explanation we first estimated the mass of the pelvis ( $M_p = 15\text{ kg}$ ) and trunk ( $M_{tr} = 45\text{ kg}$ ) as percentages of the mean rider's weight [30]. Next, we used the measured accelerations and the aforementioned masses to calculate the expected forces. At the base frequency the acceleration of the trunk was about three times higher and opposed to the direction of the saddle (see Y-axis magnitude, Figure 3.7). Therefore, a force  $F_{tr}$  with a magnitude of about 1350 N was induced at the pelvis and applied at the saddle as a reaction to the trunk postural control. The applied saddle force  $F_p$  was possibly amplified by a factor of two due to the intrinsic and reflexive responses of the rider's feet and arms (stiffness  $K_p$  and damping  $C_p$  properties of the moving base). This justifies the high lateral APMS observed at the seat and in the vertical direction of the footpegs and handlebars (see Y for seat, Z-axis for footpegs and handlebars, Figure 3.10).

As proposed by Van Drunen et al. [31] kinematic FRFs could also be interpreted as trunk-in-space (perfectly stationary orientation in space: magnitude of 0 and phase of  $\pm 180$  deg) and trunk-on-seat (perfectly moving in line with the seat: magnitude of 1 and phase of 0 deg). For heave up to 2 Hz and for surge up to 1 Hz the STST magnitude is 1 and the phase is almost 0 indicating a trunk-on-seat moving behaviour, see Figure 3.7 (Z, vertical) and (X, longitudinal). For sway above 1 Hz the STST magnitude  $< 1$  and the phase lags up to 8 Hz indicating that the rider tries to keep his trunk-in-space, see Figure 3.7 (Y, lateral). The sway APMS magnitude drops further above 1 Hz, see Figure 3.10 (Y, lateral). This can be explained by the limited STST, whereby the torso does not fully follow the saddle motion, reducing the required forces. The low frequency sway behaviour is more complex and may be studied further using models of postural control, capturing how rider's use proprioceptive, vestibular and visual feedback to generate the required

roll moments to stabilize the upper body.

### 3.7. Conclusion

For all translational motions the bicycle rider applied forces in all three-dimensional directions. Heave and surge motion interacted with each other, sway showed weak interaction with heave and surge. The vertical and longitudinal APMS for almost all bicycle interfaces followed the resonance of the STST measurements. All showed a twice as high magnitude at resonance, albeit a more heavily damped system was apparent in the STST measurements. Resonant frequencies were considerably higher in the vertical direction as compared to the longitudinal direction. Lateral measurements showed no resonance, and trunk postural control was evident in the APMS measurements. For most frequencies and perturbation directions the response of the rider's body was not close to a rigid mass, hence a parametric model is required to understand better the passive dynamic contribution of the rider to the bicycle-rider system.

## Appendix

### Notation

$a(f)$	acceleration at the bicycle base.
$a_{body}(f), a_{base}(f)$	acceleration of upper body and bicycle base.
$Coherence(f)^2$	coherence.
$CSD(f)$	cross-spectral density.
$E(t)$	motion platform.
$F(f)$	applied forces at the bicycle interfaces.
$F_{tr}, F_p$	force induced at the rider's trunk and pelvis.
$H(t)$	passive rider.
$K_p, C_p$	stiffness and damping properties of the moving base.
$M(f)$	apparent mass.
$M_p, M_{tr}$	mass of the rider pelvis and trunk.
$n(t)$	input noise.
$p(t)$	perturbation signal.
$PSD(f)$	power-spectral density.
$T(f)$	transmissibility.
$TF_{CSD}(f)$	transfer function of cross-spectral density.
$u(t)$	input signal.
$y(t)$	rider output response.

All the data used in this manuscript can be obtained by requesting from the corresponding author. The supplementary data and material related to this article are available online at <https://doi.org/10.4121/uuid:826b3dbe-886d-40f7-9f67-31f801cdc2f9> (Dialynas et al., 2019).

## References

- [1] J. P. Meijaard, J. M. Papadopoulos, A. Ruina, and A. L. Schwab, *Linearized dynamics equations for the balance and steer of a bicycle: a benchmark and review*, Proceedings of the Royal society A: mathematical, physical and engineering sciences **463**, 1955 (2007).
- [2] M. Plöchl, J. Edelmann, B. Angrosch, and C. Ott, *On the wobble mode of a bicycle*, Vehicle System Dynamics **50**, 415 (2012).
- [3] T. Fairley and M. Griffin, *The apparent mass of the seated human body in the fore-and-aft and lateral directions*, Journal of Sound and Vibration **139**, 299 (1990).
- [4] N. Mansfield and R. Lundström, *The apparent mass of the human body exposed to non-orthogonal horizontal vibration*, Journal of Biomechanics **32**, 1269 (1999).
- [5] S. Rakheja, I. Haru, and P. E. Boileau, *Seated occupant apparent mass characteristics under automotive postures and vertical vibration*, Journal of Sound and Vibration **253**, 57 (2002).
- [6] M. G. Toward and M. J. Griffin, *Apparent mass of the human body in the vertical direction: Effect of a footrest and a steering wheel*, Journal of Sound and Vibration **329**, 1586 (2010).
- [7] M. G. Toward and M. J. Griffin, *Apparent mass of the human body in the vertical direction: Inter-subject variability*, Journal of Sound and Vibration **330**, 827 (2011).
- [8] W. Wang, S. Rakheja, and P. Boileau, *Effects of sitting postures on biodynamic response of seated occupants under vertical vibration*, International Journal of Industrial Ergonomics **34**, 289 (2004).
- [9] M. S. Kim, G. J. Jeon, J. Y. Lee, S. J. Ahn, W. S. Yoo, and W. B. Jeong, *Human response of vertical and pitch motion to vertical vibration on whole body according to sitting posture*, Journal of Mechanical Science and Technology **26**, 2477 (2012).
- [10] J. Gao, Z. Hou, L. He, and Q. Xia, *Vertical vibration characteristics of seated human bodies and a biodynamic model with two degrees of freedom*, Science China Technological Sciences **54**, 2776 (2011).
- [11] P. E. Boileau, S. Rakheja, and X. Wu, *A body mass dependent mechanical impedance model for applications in vibration seat testing*, Journal of Sound and Vibration **253**, 243 (2002).
- [12] D. Więckowski, *The fundamentals of biomechanical modelling in transport facilities*, Archiwum Motoryzacji , 81 (2011).

- [13] T. Katayama, A. Aoki, T. Nishimi, and T. Okayama, *Measurements of structural properties of riders*, Tech. Rep. (SAE Technical Paper, 1987).
- [14] V. Cossalter, A. Doria, R. Lot, and M. Massaro, *The effect of rider's passive steering impedance on motorcycle stability: Identification and analysis*, *Mechanica* **46**, 279 (2011).
- [15] A. Doria and M. Tognazzo, *Identification of the biomechanical parameters of the riders of two-wheeled vehicles by means of vibration testing*, in *ASME 2012 International Design Engineering Technical Conferences and Computers and Information in Engineering Conference* (American Society of Mechanical Engineers, 2012) pp. 223–232.
- [16] A. Doria, M. Tognazzo, and V. Cossalter, *The response of the rider's body to roll oscillations of two wheeled vehicles; experimental tests and biomechanical models*, *Proceedings of the Institution of Mechanical Engineers, Part D: Journal of Automobile Engineering* **227**, 561 (2013).
- [17] A. Doria and M. Tognazzo, *The influence of the dynamic response of the rider's body on the open-loop stability of a bicycle*, *Proceedings of the Institution of Mechanical Engineers, Part C: Journal of Mechanical Engineering Science* **228**, 3116 (2014).
- [18] A. L. Schwab, J. P. Meijaard, and J. D. G. Kooijman, *Lateral dynamics of a bicycle with a passive rider model: stability and controllability*, *Vehicle System Dynamics* **50**, 1209 (2012).
- [19] J. Webster and J. Cornolo, *Comparison of european and asian morphology*, in *International Conference on 3D Body Scanning Technologies Conference* (2013) pp. 238–242.
- [20] B. E. Maki, *Selection of perturbation parameters for identification of the posture-control system*, *Medical and Biological Engineering and Computing* **24**, 561 (1986).
- [21] J. V. D. Ouden and A. L. Schwab, *Inventory of bicycle motion for the design of a bicycle simulator*, Master's thesis, Delft University of Technology (2011).
- [22] S. C. Walpole, D. Prieto Merino, P. Edwards, J. Cleland, G. Stevens, and I. Roberts, *The weight of nations: an estimation of adult human biomass*, *BMC Public Health* **12**, 1 (2012).
- [23] P. Grasgruber, J. Cacek, T. Kalina, and M. Sebera, *The role of nutrition and genetics as key determinants of the positive height trend*, *Economics and Human Biology* **15**, 81 (2014).
- [24] S. G. Hart and L. E. Staveland, *Development of NASA-TLX (task load index): Results of empirical and theoretical research*, in *Advances in psychology*, Vol. 52 (Elsevier, 1988) pp. 139–183.

- [25] N. J. Mansfield, *Human response to vibration* (CRC press, 2004).
- [26] M. J. Griffin, *Handbook of human vibration* (Academic press, 2012).
- [27] R. Pintelon and J. Schoukens, *System identification: a frequency domain approach* (John Wiley & Sons, 2012).
- [28] D. Halliday, J. Rosenberg, A. Amjad, P. Breeze, B. Conway, and S. Farmer, *A framework for the analysis of mixed time series/point process data-theory and application to the study of physiological tremor, single motor unit discharges and electromyograms*, *Progress in Biophysics and Molecular Biology* **64**, 237 (1995).
- [29] N. J. Mansfield and M. J. Griffin, *Effects of posture and vibration magnitude on apparent mass and pelvis rotation during exposure to whole-body vertical vibration*, *Journal of Sound and Vibration* **253**, 93 (2002).
- [30] S. Plagenhoef, F. G. Evans, and T. Abdelnour, *Anatomical data for analyzing human motion*, *Research Quarterly for Exercise and Sport* **54**, 169 (1983).
- [31] P. Van Drunen, Y. Koumans, F. C. T. van der Helm, J. H. Van Dieën, and R. Happee, *Modulation of intrinsic and reflexive contributions to low-back stabilization due to vision, task instruction, and perturbation bandwidth*, *Experimental Brain Research* **233**, 735 (2015).

# 4

## Design and implementation of a steer-by-wire bicycle

Corresponding article: G. Dialynas, R. Happee, A. L. Schwab, Design and implementation of a steer-by-wire bicycle, In Proceedings of the 7th Annual International Cycling Safety Conference, (2018).

### 4.1. Abstract

Since the 1800s, the design of bicycles involves a mechanical linkage between the handlebar and the fork assembly. Herein, we propose an innovation, where the traditional mechanical connection between the handlebar and fork is decoupled and replaced with sensors, servomotors and a microcontroller allowing artificial manipulation of the bicycle and steering dynamics. The purpose of our steer-by-wire bicycle<sup>1</sup> is to investigate the influence of handlebar torque feedback on rider control in order to understand rider control on a bicycle. In addition, steer-by-wire bicycles have the potential to be used as stability-enhancing support systems which can improve cycling safety. We demonstrate the design and performance of the steer-by-wire bicycle in computer simulations as well as real-life tests. Preliminary rider tests showed a perceived near-to-identical behaviour of the steer-by-wire system to a mechanical connection at steering frequencies below 3 Hz.

#### Keywords

Bicycle, steer-by-wire, stability, control, rider control.

---

<sup>1</sup>In this Chapter we present the second steer-by-wire bicycle prototype designed and built at TU Delft bicycle laboratory. The methodology adopted for the development of the first steer-by-wire prototype by Nick Appelman et al. [1] is also followed herein.

## 4.2. Introduction

Already some time ago, electronic enhancements regarding vehicle behaviour has made its way into the aviation and automotive industry by the term “by-wire” technology. This covers technology like fly-by-wire, drive-by-wire, brake-by-wire and steer-by-wire. Electronic sensors and actuators are used to replace traditional mechanical systems, and software running on a controller is used to operate the actuators in a way that it is not possible with traditional mechanical systems. The use of steer-by-wire technology can also offer great opportunities to enhance the vehicle dynamics of single-track vehicles like motorcycles, scooters and bicycles. Single-track vehicles can be laterally unstable, especially at low forward speeds and they require a relative high amount of rider control [2, 3].

### 4

In the open literature there is currently no research available which experimentally evaluates a steer-by-wire system on single-track vehicles. Only a few theoretical publications proposing enhancements in motorcycle handling [4, 5] are available. Marumo and Nagai [4] introduce a steer-by-wire system on a motorcycle which removes the counter steer behaviour to initiate a turn, where it remains questionable if this is beneficial. On the other hand, the possibility of a lane keeping assistance system on motorcycles by Katagiri et al. [5] can greatly improve safety. This is also demonstrated by Seiniger et al. [6] by actively assisting the motorcycle rider’s steer input to hold its driving path during extensive in-corner braking manoeuvres. Schwab et al. [7] were the first who actually investigated in practice the impact of active steer-torque control on the lateral stability of a bicycle. Their results showed a considerably lower rider steer effort and increased stability at low forward speeds.

Alternatively, steer-by-wire technology can also serve as a versatile experimental platform for identifying rider control in bicycling. Still, the question remains how the rider stabilizes the lateral motions of the bicycle when driven at low (unstable) forward speeds and how the rider follows a desired path. The control input probably comprises of haptic, vestibular and visual cues; however the impact of these sensory cues on rider control is still unknown. With a steer-by-wire system we can investigate the importance of haptic feedback on steering behaviour for a given set of control tasks. For instance, the task of bicycle stabilization with and without handlebar feedback can be investigated, which is not possible with a mechanical steered bicycle. The evaluation of handlebar torque feedback on rider control might lead to the development of new design criteria for safer bicycles.

The work presented here, is focused on the modelling and experimental validation of a steer-by-wire system on a bicycle. Such a system is used as a research tool to investigate rider control. After this brief introduction, the model for the system design is described and simulation results are shown. Next, the experimental setup is described and preliminary test results are shown. The chapter ends with the conclusion section highlighting the findings of this research.

### 4.3. System design and simulation

A linear multibody model for the bicycle was used to design the system. The model is based on the three-degree-of-freedom Carvallo-Whipple bicycle model [2]. This model is extended by separating the handlebar assembly from the fork assembly, which introduces an additional rotational degree of freedom.

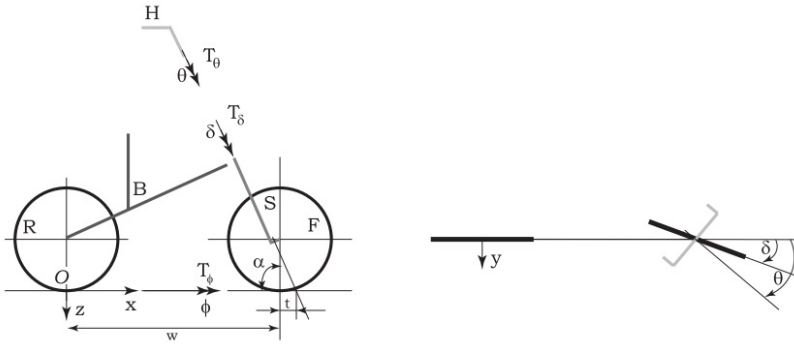


Figure 4.1: Steer-by-wire bicycle model together with the lateral degrees-of-freedom, rear frame roll angle  $\phi$ , fork angle  $\delta$ , and handlebar steering angle  $\theta$ , and some geometry variables. This model, based on the Carvallo-Whipple bicycle model [2], shows the addition of a separate handlebar body H and the possibility to have unequal steer  $\delta$  and handlebar  $\theta$  and torques  $T_\delta$  and  $T_\theta$ .

The lateral degrees-of-freedom of this extended model are shown in Figure 4.1: the rear frame roll angle  $\phi$  the fork angle  $\delta$ , and the handlebar steering angle  $\theta$ . Since we are only interested in the lateral dynamics, the forward speed  $v$ , which is a degree-of-freedom of the Carvallo-Whipple model [2], is treated as a parameter. Combining the lateral degrees-of-freedom in a generalized coordinate vector  $\mathbf{q} = [\theta, \phi, \delta]^T$ , the linearized equations of motion for the extended bicycle model can be expressed by,

$$\overline{\mathbf{M}}\ddot{\mathbf{q}} + \overline{\mathbf{C}}\dot{\mathbf{q}} + \overline{\mathbf{K}}\mathbf{q} = \overline{\mathbf{f}} \quad (4.1)$$

with the mass matrix  $\overline{\mathbf{M}}$ , damping matrix  $\overline{\mathbf{C}}$ , and stiffness matrix  $\overline{\mathbf{K}}$  given by,

$$\overline{\mathbf{M}} = \begin{bmatrix} \mathbf{I}_\theta & \mathbf{0} \\ \mathbf{0} & \mathbf{M} \end{bmatrix}, \overline{\mathbf{C}} = \begin{bmatrix} \mathbf{0} & \mathbf{0} \\ \mathbf{0} & v\mathbf{C1} \end{bmatrix}, \overline{\mathbf{K}} = \begin{bmatrix} \mathbf{0} & \mathbf{0} \\ \mathbf{0} & g\mathbf{K0} + v^2\mathbf{K2} \end{bmatrix}, \quad (4.2)$$

and the right hand side forcing term  $\overline{\mathbf{f}} = [T_\theta, T_\phi, T_\delta]^T$ , which contains the handlebar torque  $T_\theta$ , the external rear frame roll torque  $T_\phi$  (usually zero), and the fork torque  $T_\delta$ . The matrices  $\mathbf{M}$ ,  $\mathbf{C1}$ ,  $\mathbf{K0}$  and  $\mathbf{K2}$ , are the two-by-two matrices from the linearized equations of motion of the original Carvallo-Whipple model [2],  $\mathbf{I}_\theta$  is the mass moment of inertia of the handlebar assembly,  $v$  is forward speed and  $g$  is the gravitational acceleration. There is a small coupling between handlebar steering angle and the other degrees-of-freedom, but given the already small value for

the mass and inertia of the handlebar assembly  $H$ , the off-diagonal terms in the Matrices 4.2 are neglected here.

As a reference case, it will be desirable to simulate a direct connection between the handlebar and the fork. To minimize the difference between the handlebar angle  $\theta$  and the fork angle  $\delta$ , tracking control has been implemented. In this way, the steer-by-wire system should behave like an ordinary, mechanically steered bicycle, when the rider applies a steer torque at the handlebar. Two proportional-differential PD-controllers are implemented in order to provide an action-reaction torque  $T_{PDH}$  to the handlebar and  $T_{PDF}$  to the fork assembly. Angular velocity  $\dot{\theta}$  and  $\dot{\delta}$  are estimated by taking the time derivative of angular position  $\theta$  and  $\delta$  respectively, for a fixed time interval of 1 ms. The double PD-configuration can also be used to manipulate the steer feedback torque independent of the tracking performance. The double PD-controller is of the following form,

$$T_{PDH} = K_{PH}(\theta - \delta) + K_{DH}(\dot{\theta} - \dot{\delta}), \quad (4.3)$$

$$T_{PDF} = K_{PF}(\theta - \delta) + K_{DF}(\dot{\theta} - \dot{\delta}) \quad (4.4)$$

with proportional gains  $K_{PH}$ ,  $K_{PF}$  and differential gains  $K_{DH}$ ,  $K_{DF}$  respectively. The torque  $T_{PDH}$  is applied at the upper motor, and the torque  $T_{PDF}$  at the lower motor (thus ignoring motor dynamics). The forcing term in Equation 4.1 then becomes,

$$\bar{\mathbf{f}} = \begin{bmatrix} T_{\theta} \\ T_{\phi} \\ T_{\delta} \end{bmatrix} = \begin{bmatrix} T_h - T_{PDH} \\ 0 \\ T_{PDF} \end{bmatrix}, \quad (4.5)$$

with the rider applied steer torque  $T_h$  at the handlebar, and zero applied roll angle torque. Ideally the two controller torques could be identical, however we have the freedom to choose the gains  $K_{PH}$  and  $K_{PF}$  and  $K_{DH}$  and  $K_{DF}$  differently. From the outside a rider perceives only the in series combined stiffness and damping. The double PD-controller configuration combined with steer-by-wire bicycle plant model can be visualized in a block diagram as shown in Figure 4.2. For the PD-controllers, the proportional and differential gains in Equation 4.3, 4.4 are chosen such that a critically damped system response is obtained to ensure a fast and accurate response without overshoot.

As an example, we use the parameters of the benchmark bicycle [2], with a handlebar inertia of  $I_0 = 0.001 \text{ kgm}^2$ , proportional gain  $K_p = 90 \text{ Nm/rad}$ , and differential gain  $K_d = 0.6 \text{ Nms/rad}$ . As a first measure of performance the tracking transfer function of the steer-by-wire system, defined as  $H_{SBWe}(s) = \delta(s)/\theta(s)$  is analyzed. The tracking transfer function magnitude shows the angular error between the handlebar and the fork whereas the phase describes the latency in the system response.

In Figure 4.3 the tracking transfer function magnitude (a) and phase (b) are presented as a function of input frequency and forward speed. In general the gain

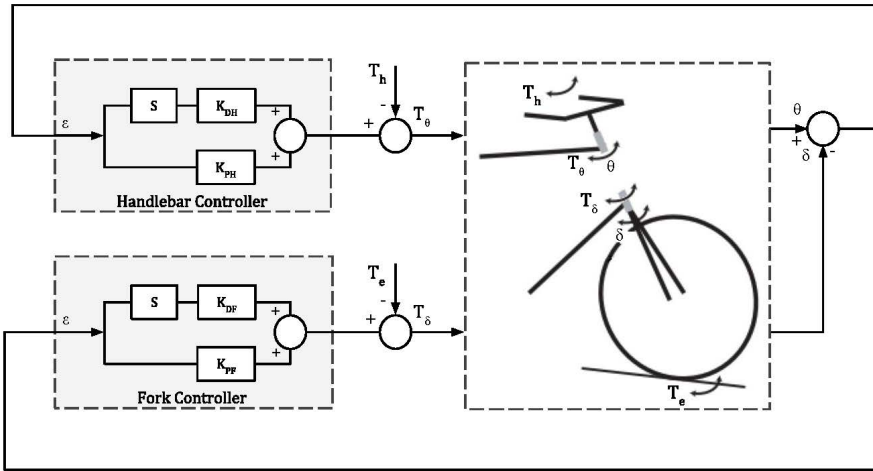


Figure 4.2: Block diagram of the steer-by-wire bicycle model, which includes a double PD-configuration, with rider applied steering torque  $T_h$ , handlebar steering feedback torque  $T_\theta$ , handlebar steering angle  $\theta$ , fork applied torque  $T_\delta$ , ground reaction  $T_e$  and fork angle  $\delta$ .

is close to one and phase is close to zero indicating a behaviour approximating a mechanical connection. At a steering frequency of 3.1 Hz and a bicycle speed below the weave speed ( $v_w = 4.29$  m/s), a substantial increase in tracking magnitude occurs (as shown by the resonance-like upward peak at 0 m/s). A slight tracking magnitude decrease occurs above 7 m/s at an input steering frequency range of 0.2-0.8 Hz. The increase in the tracking magnitude near the resonance-like peak makes the bicycle hard to control, but this occurs only at very low speeds combined with steering input above 2.5 Hz.

Phase lead is noticed for an input steering frequency of 0-1.2 Hz and an input speed above 7 m/s. On the other hand, the phase lag fluctuates between 0-20 deg below 7 m/s up to 2.5 Hz. Above 2.5 Hz the phase lag decreases for all speed ranges with a slope of approximate -86 deg/Hz until it reaches a plateau of about -150 deg above 4 Hz. The phase lag decrease above 2.5 Hz indicates a large latency in the system response. The fork can no longer follow the handlebar commanded steer angle within a given time threshold. The increased time delay above certain frequencies might increase the steer effort and lead to loss of control in case the phase lag becomes too large.

The resonance-like peak in the tracking magnitude at 3.1 Hz and the increase in phase lag above 2.5 Hz is due to the finite stiffness of the tracking controller, whereas the slight tracking magnitude decrease and phase lead at forward speeds above 7 m/s is due to the velocity-dependent properties of the stiffness matrix **K2**. In summary, the simulated controller shows good tracking performance in a frequency range of 0-2.5 Hz and in a speed range of 0-10 m/s; above this frequency

range, the tracking magnitude and phase lag significantly increase, especially at low forward speeds.

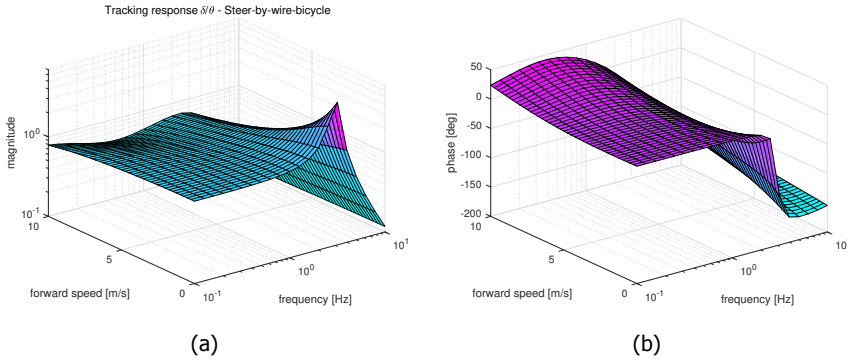


Figure 4.3: Magnitude and phase response of tracking transfer function of steer-by-wire system  $H_{SBWe}(s)$ , as a function of forward speed  $u$  and frequency.

As a second measure of performance we compared the steer stiffness transfer functions of the benchmark bicycle and the steer-by-wire bicycle. The steer stiffness transfer function for the benchmark bicycle model is defined as  $H_{BB}(s) = T_{\delta}(s)/\delta(s)$  and for the steer-by-wire bicycle are defined as  $H_{SBW}(s) = T_{\theta}(s)/\theta(s)$  and as  $H_{SBWS}(s) = T_{\theta}(s)/\delta(s)$ . The steer-by-wire transfer function  $H_{SBW}(s)$  describes the steer stiffness perceived by the rider at the handlebars, whereas  $H_{SBWS}(s)$  describes the in series stiffness and damping of the handlebar and fork assembly as a combined system. The steer stiffness transfer functions of the benchmark bicycle  $H_{BB}(s)$  and steer-by-wire system  $H_{SBWS}(s)$  are influenced in the same way and for this reason they are not discussed.

In Figure 4.4 the steer stiffness magnitude of the benchmark bicycle model (a) and the steer stiffness magnitude of the steer-by-wire bicycle (b) are presented as a function of input frequency and forward speed. At higher frequencies the steer stiffness is primarily defined by the mass and inertia properties of the bicycle. A significant drop in the steer stiffness magnitude relation occurs in both models at the weave speed ( $v_w = 4.29$  m/s) and the corresponding weave frequency (0.55 Hz) of the bicycle shown by the downward peak approaching a zero stiffness. The steer stiffness of the steer-by-wire bicycle at higher frequencies is primarily defined by the stiffness and damping properties of the PD-controller, whereas the resonance-like upward peak at low forward speeds is caused by the PD-controller coefficients and the mass and inertia properties defined in the system matrix.

The steer stiffness comparison shows an almost identical handlebar stiffness behaviour in a frequency range of 0-3 Hz and in a forward speed range of 0-10 m/s. Above 3 Hz the steer stiffness of the steer-by-wire bicycle shows a plateau whereas the steer stiffness of the benchmark bicycle continues to increase until it reaches a maximum of about 920 Nm/rad at 10 Hz. In other words, the steer-by-wire bicycle

handlebars are more compliant compared to the benchmark bicycle, a larger steer angle is obtained for the same steer torque input. The difference in the handlebar steer stiffness might also indicate higher rider steer effort but does not influence bicycle stability.

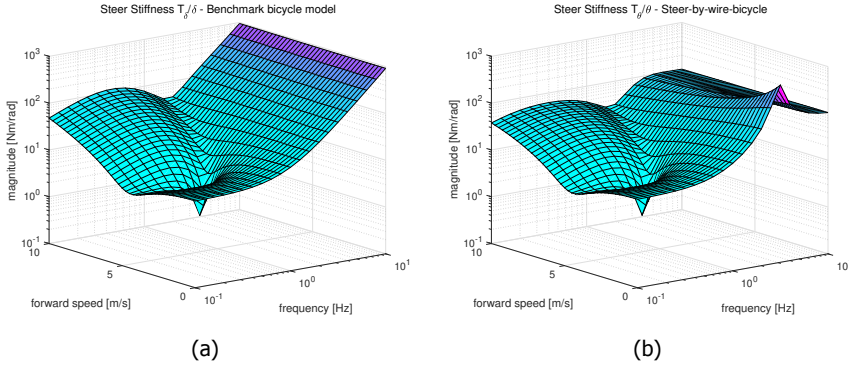


Figure 4.4: Magnitude of the steer stiffness transfer function, as perceived by the rider, as a function of forward speed  $u$  and frequency, (a) on the benchmark bicycle  $H_{BB}(s)$ , and (b) the steer-by-wire bicycle  $H_{SBW}(s)$ .

## 4.4. Hardware description

A custom made bicycle frame with two headtube assemblies was designed and built, see Figure 4.5. The basic geometry configuration of the custom frame was selected based on the dimensions of a Dutch city bicycle (Batavus Browser 54 cm). To adapt the frame geometry for an increased stack height (due to the extended headtube assembly) rattleCAD software was used. RattleCAD software provides a fully parametric bicycle model and was used in this case to evaluate the impact of an increase stack height on the rest of the frame geometry. A frame stack height of 713 mm and a frame reach of 358 mm were selected for this particular bicycle frame.

Two identical Maxon EC45 brushless DC motors coupled with two Maxon GP42C planetary gearhead (36:1 reduction ratio) are used to actuate the fork and handlebar assembly. Belt drive (1:1 reduction ratio) transmissions are used to transmit torque from the motor to the fork and handlebar respectively. The existing drive configuration allows a maximum continuous torque of 7.5 Nm and a maximum instantaneous torque of about 11.3 Nm. The total backlash of the system is about  $0.8^\circ$  (mainly due to the planetary gearhead configuration). To provide the handlebar and fork tracking controllers with the required states two identical RMB20SC 13 bit absolute angular encoders are used. The simulation of the control loops, state estimation and data logging are implemented in a Teensy 3.6 microcontroller that runs an update loop at a rate of 1 kHz. The constant update loop rate is achieved by the implementation of a real time operational system (RTOS) called



Figure 4.5: Steer-by-wire bicycle prototype with handlebar and fork actuators, sensors, digital controller and custom made battery pack.

4

Teensy threads.

Additional sensors are implemented on the bicycle to acquire knowledge of the rest of the bicycle states. More specific, an inertial measurement (IMU) unit MPU9250 is located inside the electronic control box at the back of the bicycle rack, see Figure 4.5. The IMU is used to monitor 6D translational and rotational accelerations. Two gearwheel rotary encoders with a resolution of 192 counts /revolution combined with GTS35 reading heads are used to measure pedal cadence and forward velocity at the rear wheel. A rear hub magic pie 5 motor driven by a throttle controller is used to cruise at high speeds without pedalling if needed. A deadband mechanism with  $\pm 5$  deg play is designed as a safety to enable steering upon system failure. The locations of the sensors (excluding the IMU), actuators and safety mechanism are shown in Figure 4.6.

## 4.5. Tracking controller performance

The proposed PD-controller gains of  $K_p = 90$  Nm/rad and of  $K_d = 0.6$  Nm/rad of the benchmark bicycle simulation would in practice result in unrealistic high actuator torques. On the other hand, unmodeled actuator and controller dynamics of the fork and handlebar assembly can also cause unstable oscillatory modes. For these reasons, the double PD-controller gains were selected experimentally to maximize the tracking performance without forcing the handlebar or fork assembly in an unstable mode. The effective stiffness and damping in the steer torque path and

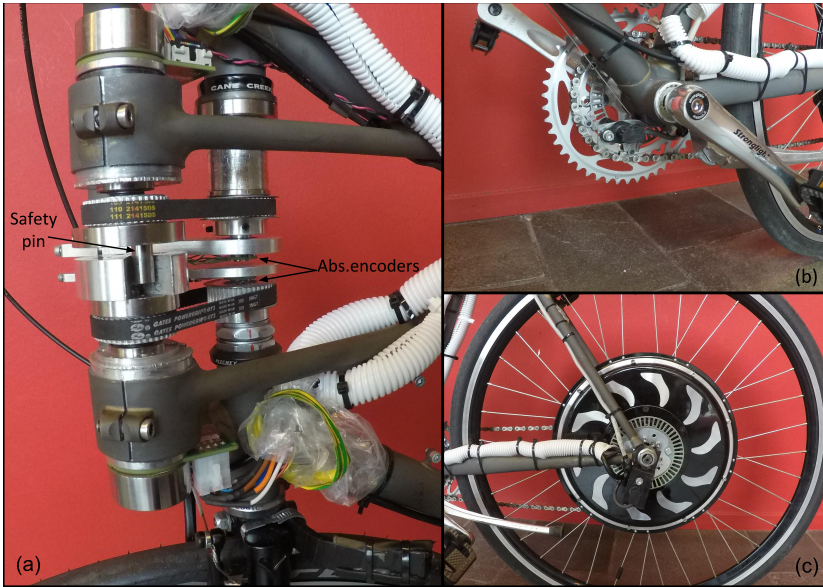


Figure 4.6: Steer-by-wire bicycle component layout, showing the physical placement of the actuators and sensors, with (a) headtube assembly with motor sensors and safety pin, (b) pedal speed sensor, and (c) rear wheel with forward speed sensor and hub motor.

in the handlebar torque path are  $K_{PH} = 0.9$  Nm/rad,  $K_{DH} = 0.012$  Nm/rad and  $K_{PF} = 2$  Nm/rad,  $K_{DF} = 0.025$  Nm/rad respectively.

To test the tracking performance, fifteen participants were asked to perform a set of slalom maneuvers in a controlled environment in the stable and unstable bicycle speed region. All participants could easily control the steer-by-wire bicycle without any training. The frequency steering range during the 90 second task for all participants swept between 0 and 2 Hz. The tracking response of the controller in the time domain for one of the participants is shown in Figure 4.7. As can be seen, a maximum tracking error of approximately 0.05 rad can be noticed for large steering amplitudes  $\pm 0.4$  rad and a tracking error of about 0.02 rad for smaller steering amplitudes  $\pm 0.25$  rad. The mean tracking error during the 90 second stability tasks is 0.002 rad.

The frequency response of the tracking controller can be approximated by the empirical tracking transfer function, the ratio of the Discrete Fourier Transform (DFT) between the fork angle  $\delta$  and handlebar angle  $\theta$ . The empirical steer-by-wire tracking transfer function is defined as  $H_{ESBWe}(s) = \delta(s)/\theta(s)$ . A Savitzky-Golay filter (2nd order, 113 frame length) is used to smooth the magnitude and phase data. The tracking magnitude and phase for a frequency range between 0-2 Hz is shown in Figure 4.8. As can be seen, the tracking amplitude ratio fluctuates between 0.95-1.1 for the entire frequency range, whereas the phase lag increases for higher

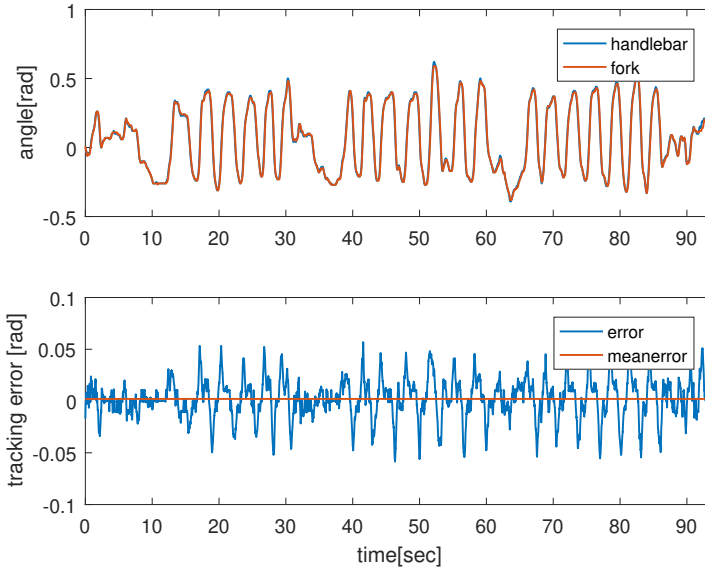


Figure 4.7: Commanded handlebar steering angle and actual fork angle, tracking error and mean tracking error, while a human subject performs a slalom.

frequencies and reaches a maximum of 24 deg at 2 Hz <sup>2</sup>. In general the gain is close to one and the phase lag fluctuates between 10-20 deg indicating a behaviour approximating a mechanical connection. Future studies are recommended using feedforward control algorithms to improve system performance at higher frequencies.

## 4.6. Conclusions

A steer-by-wire bicycle with a double PD-controller configuration has been designed and built. Simulations showed good tracking performance in a frequency range of 0-2.5 Hz and almost identical steer stiffness with the Carvallo-Whipple model [2] in a frequency range of 0-3 Hz and in a forward speed range of 0-10 m/s. Preliminary testing also showed a perceived near-to identical behavior of the steer-by-wire system to a mechanical connection. More specifically, a mean tracking error in the steer angle of 0.02 rad and a mean phase lag of approximately 15.6 deg is noticed during the stability experiments. In future research the steer-by-wire bicycle will serve as a versatile experimental platform for identifying human rider control in bicycling [8], and development of support systems enhancing balance and handling.

<sup>2</sup>Due to the fact that steering frequencies might exceed the aforementioned bandwidth at certain conditions further analysis of the tracking response is recommended. An idea could be to inject colored noise with a frequency bandwidth of 0-5 Hz but the latter might be tricky especially if real-riding tests are conducted.

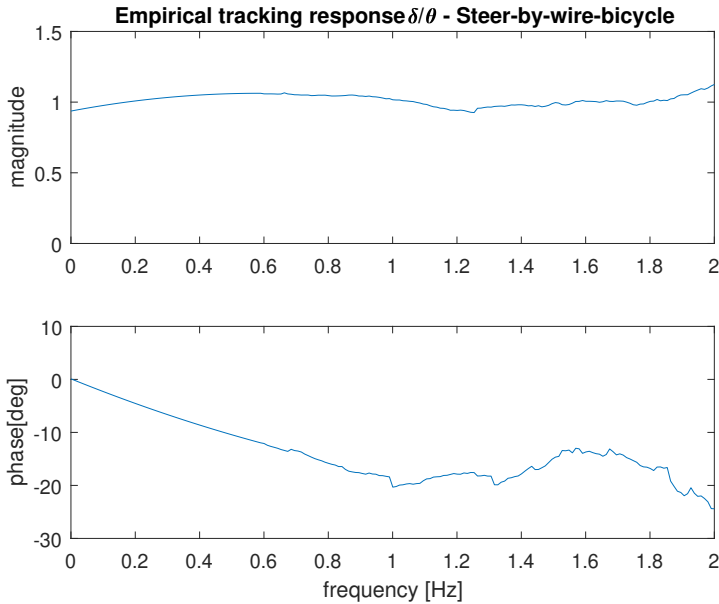


Figure 4.8: Magnitude and phase response of empirical steer-by-wire tracking transfer function  $H_{ESBe}(s)$ , as a function of frequency.

## References

- [1] N. Appelman and A. L. Schwab, *Dynamics and control of a steer-by-wire bicycle*, *Master's thesis*, Delft University of Technology (2012).
- [2] J. P. Meijaard, J. M. Papadopoulos, A. Ruina, and A. L. Schwab, *Linearized dynamics equations for the balance and steer of a bicycle: a benchmark and review*, in *Proceedings of the Royal Society of London A: Mathematical, Physical and Engineering sciences*, Vol. 463 (The Royal Society, 2007) pp. 1955–1982.
- [3] J. D. G. Kooijman, J. P. Meijaard, J. M. Papadopoulos, A. Ruina, and A. L. Schwab, *A bicycle can be self-stable without gyroscopic or caster effects*, *Science* **332**, 339 (2011).
- [4] Y. Marumo and M. Nagai, *Steering control of motorcycles using steer-by-wire system*, *Vehicle System Dynamics* **45**, 445 (2007).
- [5] N. Katagiri, Y. Marumo, and H. Tsunashima, *Controller design and evaluation of lane-keeping-assistance system for motorcycles*, *Journal of Mechanical Systems for Transportation and Logistics* **2**, 43 (2009).
- [6] P. Seiniger, K. Schröter, and J. Gail, *Perspectives for motorcycle stability control systems*, *Accident Analysis & Prevention* **44**, 74 (2012).

- [7] A. L. Schwab and N. Appelman, *Dynamics and control of a steer-by-wire bicycle*, in *Proceedings of Bicycle and Motorcycle Dynamics Conference* (2013).
- [8] A. L. Schwab, P. D. L. de Lange, R. Happee, and J. K. Moore, *Rider control identification in bicycling using lateral force perturbation tests*, *Proceedings of the Institution of Mechanical Engineers Conference, Part K: Journal of Multibody Dynamics* **227**, 390 (2013).

# 5

## The effect of haptic feedback in the balance task of bicycling

Corresponding article: G. Dialynas, C. Christoforidis, R. Happee, A. L. Schwab, The effect of haptic feedback in the balance task of bicycling, In Proceedings of the 4th Triannual International Bicycle and Motorcycle Dynamics Conference, (2019).

### 5.1. Abstract

The objective of this research is to study the effect of haptic steering feedback on the balancing task of a bicycle during lateral perturbation tests, in an effort to improve two-wheeler safety. The steer-by-wire bicycle designed and built at TU Delft bicycle laboratory is used as an experimental platform to analyze the rider response with and without steering feedback. The response of the rider's control actions is represented in the time domain by means of impulse response functions (IRFs). More specifically, three metrics are defined in order to assess both steering and balancing performance. Results failed to indicate any statistically significant difference between experimental conditions. Although it should be mentioned that parametric rider control identification of the sensory systems might be prerequisite to indicate any possible changes.

### 5.2. Introduction

Since the birth of the safety bicycle in the 1890s, dynamics and self-stability have been subjects of numerous discussions and bodies of research. These issues can nowadays be considered to be partly resolved [1] for a wide range of applications. Still, the question remains on how the rider stabilizes the lateral motions of the

bicycle when it's driven at low (unstable) forward speeds or how the rider follows a desired path; e.g. the required control inputs and the rider learning process. These probably comprise of haptic, vestibular and visual cues; here we will focus on the haptic cues and the task of stabilization.

Haptic systems in vehicle control are usually connected with two types of realities. One current application of kinesthetic devices is focused on enabling the driver to feel feedback from the vehicle state when steer-by-wire systems come into play. Steer-by-wire vehicles often need a resistance torque to prevent excessive rotation of the steering wheel. This feedback torque is often defined by a simple relation, e.g. a function of wheel angle, wheel torque, or vehicle state, and aims to assist the driver in achieving the desired trajectory in real performance [2]. Similarly, haptics can also be used as a tool to improve first stages of task learning through fading guidance towards a goal [3]. On the other hand, computer simulations can be helpful in evaluating different strategies for steering control [4], as a previous stage to its implementation, and in development of control systems aimed to improve riding safety [5].

In this work we use the experimental steer-by-wire bicycle [6] which has been developed in the TU Delft bicycle laboratory to study the effect of haptic feedback in the balancing task of bicycling. This is achieved by analyzing the rider response with and without steering feedback during lateral perturbation tests. The response of the rider's control actions is represented in time domain by means of impulse response functions (IRFs). More specific, the applied steer angle and the estimated roll angle is used as a measure of control effort and performance respectively.

The paper is organized as follows: After this brief introduction the experimental set-up and experimental procedure are presented. Next, the methods followed by the results are described. The article ends with the discussion and conclusion section providing further insights in an attempt to explain the findings of this research.

## 5.3. Methods

### 5.3.1. Description of experimental set-up

At TU Delft an instrumented steer-by-wire bicycle which is fully equipped with a number of sensors to measure the state and rider input has been designed and built, see Figure 5.1. For this study measurements from the inertial measurement unit (IMU) sensor (MPU-9250) and the steering angle encoder (RMB-20SC) are used. In addition, a perturbator mechanism is present, which is used to excite the system. These perturbations are applied by laterally pulling a rope with a force transducer in series, which is attached on the seat post. All sensors output are logged with a sampling frequency ( $F_s$ ) equal to 1000 Hz. The measurement bicycle is electrically driven and has a cruise control system, so the rider does not need to exert pedaling power and thus eliminates the need for lower limb movement. Steering angle ( $\delta$ ) is directly measured from the absolute encoder of the upper front assembly, while the roll angle ( $\phi$ ) is estimated from the IMU data using the

approach described by Sanjurjo et al. [7].



Figure 5.1: Steer-by-wire bicycle prototype with handlebar and fork actuators, sensors, pulling rope mechanism, digital controller and custom made battery pack.

### 5.3.2. Description of steer-by-wire controller

To minimize the difference between the handlebar angle  $\theta$  and the fork angle  $\delta$ , tracking control has been implemented. In this way, the steer-by-wire system should behave like an ordinary, mechanically steered bicycle, when the rider applies a steer torque at the handlebar. Two proportional-differential PD-controllers are implemented in order to provide an action-reaction torque  $T_{PDH}$  to the handlebar and  $T_{PDF}$  to the fork assembly. Angular velocity  $\dot{\theta}$  and  $\dot{\delta}$  are estimated by taking the time derivative of angular position  $\theta$  and  $\delta$  respectively, for a fixed time interval of 1 ms. The double PD-configuration can also be used to manipulate the steer feedback torque independent of the tracking performance. The double PD-controller is of the following form:

$$T_{PDF} = K_{PF}(\theta - \delta) + K_{DF}(\dot{\theta} - \dot{\delta}), \quad (5.1)$$

$$T_{PDH} = K_{PH}(\theta - \delta) + K_{DH}(\dot{\theta} - \dot{\delta}) \quad (5.2)$$

with proportional gains  $K_{PH}$ ,  $K_{PF}$  and differential gains  $K_{DH}$ ,  $K_{DF}$  respectively. The torque  $T_{PDH}$  is applied at the upper servomotor, and the torque  $T_{PDF}$  at the lower servomotor. By setting  $T_{PDH}$  to zero a steering configuration is created where the rider feels no reaction torque from the steering assembly (feedback off), without majorly affecting tracking error performance. The current controller configuration

performs with high level of accuracy up to 3 Hz, the tracking error is kept below 3 degrees. However, in certain conditions non-linear effects of the servomotors and tires might create a delay in the control loop effecting the tracking error and realism of the haptic steering feel.

### 5.3.3. Experimental procedure

Twenty healthy subjects volunteered in this study. To assure safety all subjects were requested to wear protective equipment in the shape of a standards-approved bike helmet, knee and elbow pads. All participants gave informed consent according to the guidelines of the human research ethics committee of Delft University of Technology. All subjects were healthy and reported that they did not experience any kind of pain or injury in the year before the experiments. The mean weight of all subjects was selected to be close to the European population [8].

Each experiment trial consisted of four different speeds (i.e. 2.6, 3.7, 4.5, 5.6 m/s). Two individual trials were performed in total for every speed. In the first trial steering feedback was enabled, whereas in the second trial steering feedback was disabled. Every trial had a duration of approximately 60 seconds. All experiments were performed across Heertjeslaan cycling path of TU Delft, the subjects were requested to ride the steer-by-wire bicycle in all aforementioned speeds while being laterally perturbed. An additional bicycle was used from the experiment coordinator to cycle next to the instrumented steer-by-wire bicycle and perturb the subject, see Figure 5.2. A set-up which allowed both push and pulls was initially tested but the pushes were subject to inconsistencies. After inspecting the data of the pilot runs, it was observed that unilateral disturbances did not affect the predictability of the perturbation, as the response of the rider was similar. For this reason the unilateral approach was chosen. Nevertheless, to avoid any feedforward control behaviour (e.g. seeing the coordinator preparing to pull the rope) all subjects were asked to keep their focus on the road ahead.

### 5.3.4. System identification

In order to remove the effects of unwanted disturbances and noise, the measured steering angle and estimated roll angle signals were filtered through a finite impulse response (FIR) model. The impulse response function is defined as the function  $h(\tau)$  which when convoluted with external input  $w(t)$  results in the output  $y(t)$ . The output data either represents  $y(t) = \phi(t)$  corresponding to  $h_\phi(\tau)$  or  $y(t) = \delta(t)$  corresponding to  $h_\delta(\tau)$ . In discrete time the convolution can be approximated by the following equation:

$$y(t) = \sum_{\tau=0}^{T-1} h(\tau)w(t - \tau)\Delta\tau + v(t) \quad (5.3)$$

where  $T$  is the time length of the impulse function, which is equal to 3.08 seconds as the oscillations die out after that point and  $v(t)$  the remnant which is caused by



Figure 5.2: Experimental trial performed across Heertjeslaan cycling path of TU Delft; Experiment coordinator cycling next to steer-by-wire bicycle while pulling laterally the subject with a rope.

5

unwanted disturbances. Equation 5.3 is rewritten in matrix form as follows:

$$y = Wh + v \quad (5.4)$$

where  $W$  is the matrix containing time shifted versions of the the input signal.

$$W = \begin{bmatrix} w(0) & 0 & 0 & \dots & 0 \\ w(1) & w(0) & 0 & \dots & 0 \\ w(2) & w(1) & w(0) & \dots & 0 \\ \vdots & \vdots & \vdots & \ddots & 0 \\ w(N-1) & w(N-2) & w(N-3) & \dots & w(N-T) \end{bmatrix} \quad (5.5)$$

Since Equation 6.18 is linear in the parameters (the coefficients of  $h$ ) there exists a unique solution that can be found through the least squares method.

$$\hat{h} = (W^T W)^{-1} W^T y \quad (5.6)$$

Having an estimate of the IRF, the input signal is convoluted with  $(\hat{h})$  in order to produce an estimate of the output ( $\hat{y}$ ) without the noise. The estimated responses are further smoothed using a eight-order Butterworth filter with cutoff frequency of 10 Hz.

### 5.3.5. Comparison metrics

In order to correctly assess if there is a statistically significant difference between the two conditions, three metrics are defined. The first one is the Power Spectral

Centroid (PSC) of measured angle ( $\delta$ ) defined as

$$(PSC_x, PSC_y) = \left( \frac{\sum_{n=1}^N f(n)S_\delta(n)}{\sum_{n=1}^N S_\delta(n)}, \frac{\sum_{n=1}^N S_\delta(n)^2}{\sum_{n=1}^N S_\delta(n)} \right) \quad (5.7)$$

where  $N$  is the number of samples lower than 5 Hz and  $S_\delta(f)$  the power spectral density of the signal. This metric gives an indication of the frequency which most of the power in the signal is centered around. Higher value of  $PSC_x$  will indicate more oscillatory behaviour for the steering response and can be used as a metric of control effort.

The variance accounted for (VAF) is used to assess the quality of the fit of the FIR model output. The runs which scored lower than 60% were removed from further analysis as it was deemed that the model did not sufficiently capture the characteristics of the raw signal. The VAF between  $\hat{h}_\phi^{off}$  and  $\hat{h}_\phi^{on}$  is also used as a metric of similarity for the roll angle response. In that case VAF is defined as:

$$VAF_\phi = \left( 1 - \frac{\text{var}(\hat{h}_\phi^{off} - \hat{h}_\phi^{on})}{\text{var}(\hat{h}_\phi^{off})} \right) \cdot 100\% \quad (5.8)$$

Finally as a third test, the relative delay between the steering angle IRFs of the two conditions is estimated by finding the lag value of maximum cross-correlation between the signals.

## 5.4. Results

A dependant paired sample t-test was conducted to compare if there was significant difference (95% confidence interval) in steering effort between conditions for all speed levels, see Figure 5.3.

For forward speed 2.6 m/s there was no significant difference in the scores for feedback on ( $M = 0.8$ ,  $SD = 0.1$ ) and feedback off ( $M = 0.77$ ,  $SD = 0.12$ ) conditions;  $t(19) = 1.18$ ,  $p = 0.2539$ . For forward speed 3.7 m/s there was no significant difference in the scores for feedback on ( $M = 0.91$ ,  $SD = 0.13$ ) and feedback off ( $M = 0.92$ ,  $SD = 0.2$ ) conditions;  $t(19) = -0.28$ ,  $p = 0.7825$ . For forward speed 4.5 m/s there was no significant difference in the scores for feedback on ( $M = 0.97$ ,  $SD = 0.14$ ) and feedback off ( $M = 1.01$ ,  $SD = 0.2$ ) conditions;  $t(19) = -1.58$ ,  $p = 0.13$ . For forward speed 5.6 m/s there was no significant difference in the scores for feedback on ( $M = 1.06$ ,  $SD = 0.16$ ) and feedback off ( $M = 1.1$ ,  $SD = 0.21$ ) conditions;  $t(19) = -1.27$ ,  $p = 0.21$ .

The impulse response function of the mean rider for steer angle ( $\delta$ ) and roll angle ( $\phi$ ) is shown in Figure 5.4. The variance accounted for between roll angle impulse responses (see Equation 5.8) is averaged over all participants and displayed for all speed levels in Figure 5.5 (a). Similar roll angle response between feedback on and off indicated by higher  $VAF_\phi$  values suggests matching task performance.

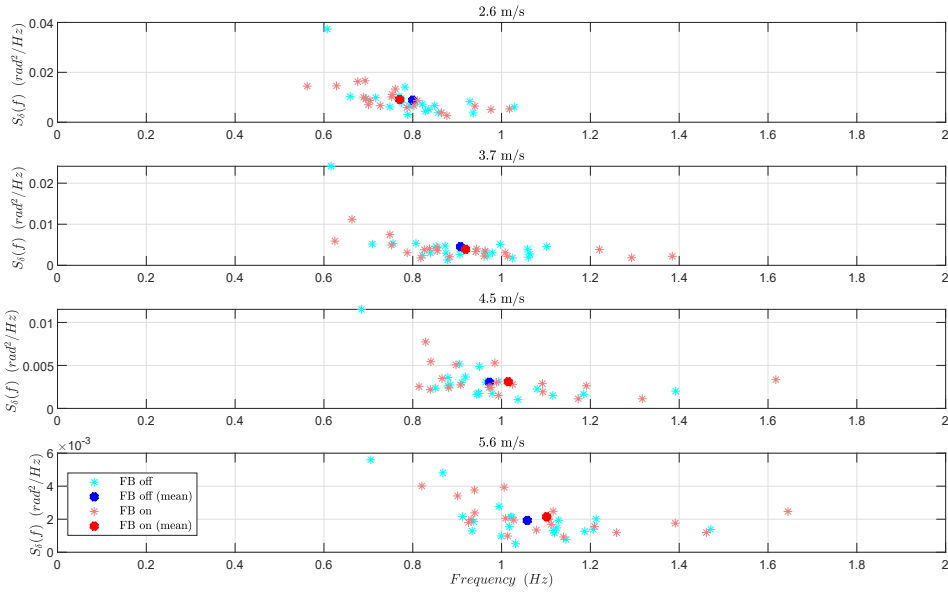


Figure 5.3: The x and y coordinate of the PSC used to determine the frequency where most of the power is concentrated.

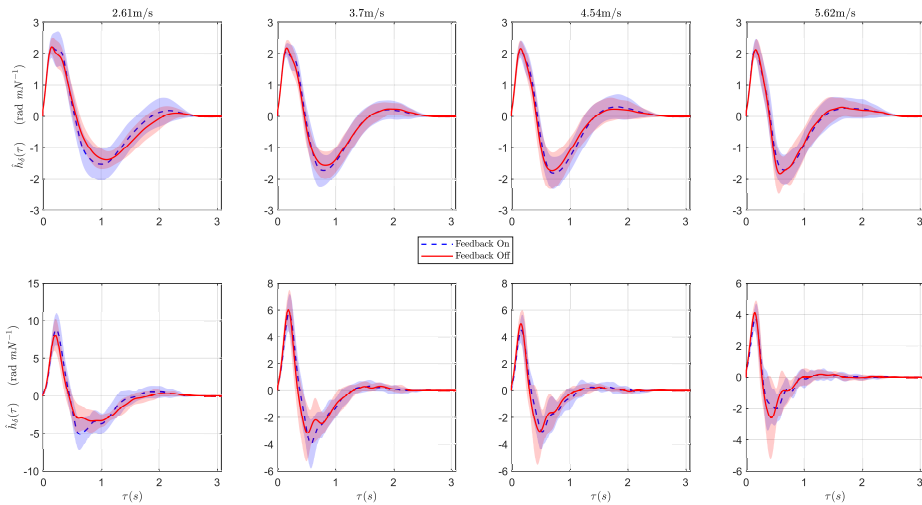


Figure 5.4: The impulse response function of the mean rider for steer angle ( $\delta$ ) and roll angle ( $\phi$ ). The shaded area represents the values within one standard deviation of the mean.

In addition to the variance roll test an one-sample t-test was conducted to examine if there is any delay in the steering response between feedback on and off, see Figure 5.5 (b). For 2.6 m/s there was no significant deviation in the delay ( $M = -3$ ,  $SD = 25.89$ ) from zero mean;  $t(19) = -0.52$ ,  $p = 0.6103$ . However, for 3.7 m/s the delay ( $M = -20.65$ ,  $SD = 25.93$ ) was statistically significant;  $t(19) = -3.56$ ,  $p = 0.0021$ . Also for 4.5 m/s the mean of the delay ( $M = -23.5$ ,  $SD = 20.88$ ) was also significantly different than zero;  $t(19) = -5.03$ ,  $p = 0.0001$ . Lastly, for 5.6 m/s there was again significant difference in the delay ( $M = -19.15$ ,  $SD = 18.19$ ) from zero;  $t(19) = -4.71$ ,  $p = 0.0002$ .

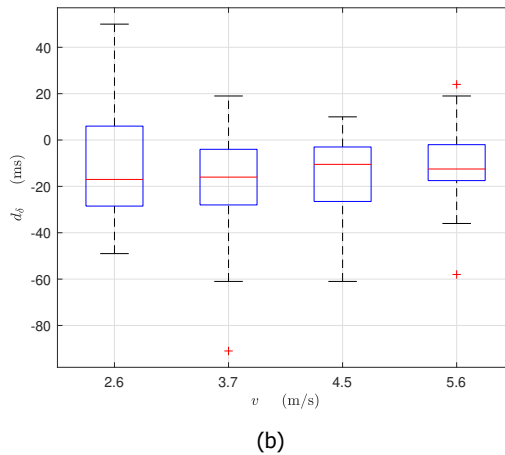
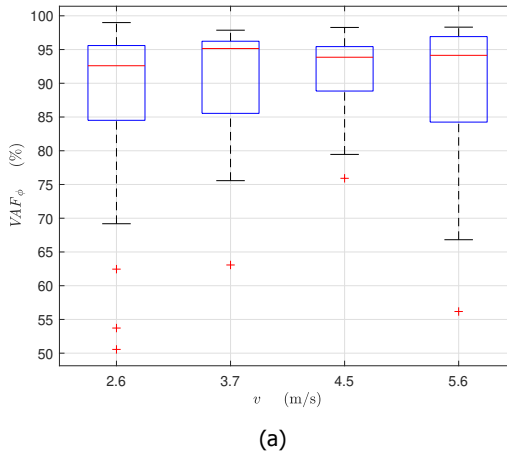


Figure 5.5: a) Box plot of variance accounted for between roll angle impulse response functions for all speed levels. b) Box plot of the relative delay in the estimated steering angle response between the two experimental conditions. Negative value means that the feedback on signal is delayed compared to the feedback off.

## 5.5. Discussion and conclusions

From the aforementioned results it is suggested that the effects of haptic feedback are minimal to non-existent for the roll stabilization task. Neither performance (see Figure 5.5 (a)) or steering effort was affected by the removal of haptic steering feedback. Balance performance among conditions was comparatively consistent (see Figure 5.5 (a)). However, in the unstable speed region the variance and the number of outliers were higher. For steering effort the null hypothesis that the  $PSC_x$  metric came from independent random samples with equal means and equal variances failed to be rejected for all speed levels. This does not undoubtedly prove that the samples came from the same population, however it gives a strong indication towards that fact. On the other hand, for the feedback on the steering response was delayed ( $\approx 18$  ms see Figure 5.5 (b)) in comparison to the feedback off. This might be due to the fact that the handlebars are more inert due to the additional steering feedback.

The lateral pull disturbances can be translated into a lean torque in the direction of forward speed and a steer torque in the direction of the steering axis. This means that any dynamic effects that influences these torques must be examined. The performance of the steer-by-wire controller was examined by numerical simulation and subjective measurements. All subjects reported that they felt like riding a mechanically steered bicycle, no adaptation period was required before the experiments. During the experiments very little motion of the upper body was evident and steer control was expected to be the main mechanism for bicycle balance [9]. Thus, we assume that the intrinsic and reflexive responses of the upperbody do not affect the validity of these results.

Physiologically there are two ways in which proprioception works in order to give the rider information regarding the state of the front assembly. First are the muscle spindles which by detecting changes in velocity and position of the shoulder joint give the rider an estimation of the steering angle and steering rate of the handlebars. Second are the Golgi tendon organs which work as force feedback sensors. The sensory information provided by the latter sensor is what this experiment tried to invalidate. In the feedback on case, information from the ground reaction torque of the front tire is transferred through the handlebars to the sensory receptors of the rider arms and is used for further state estimation. In the feedback off case the steering feedback information is lost.

Despite the change in the dynamics of the upper handlebar the response of the rider is almost identical. Thereupon, we assume that the internal controller of the rider is either adaptive or is driven by some combination of torque or position control. In the case of torque control this would mean complete readaptation of feedback gains which would have resulted in some kind of adaptation period for the participants when they swapped steering configurations. Although, no adaptation period was needed for any of the participants. Alternatively, in the case of position control steer angle increments are feed-through an inverse model of the steering assembly to produce the necessary forcing element. In this case, switching between

configurations, would mean readaptation of the internal model of the handlebar assembly. This is much more plausible as it mainly concerns tuning of the internal perception of handlebar inertia which can happen instantaneously. To reveal if the later assumption is true an additional study that models the rider as position and torque controller will be conducted. The identified parameters of the former and later controller might lead into further insights regarding the conclusions of this study.

All the data used in this manuscript can be obtained by requesting from the corresponding author. The supplementary data related to this article are available online at <https://doi.org/10.5281/zenodo.3484032> (Dialynas et al., 2019).

## References

- [1] J. D. G. Kooijman, J. P. Meijaard, J. M. Papadopoulos, A. Ruina, and A. L. Schwab, *A bicycle can be self-stable without gyroscopic or caster effects*, *Science* **332**, 339 (2011).
- [2] R. Hayama, S. Kawahara, S. Nakano, and H. Kumamoto, *Resistance torque control for steer-by-wire system to improve human-machine interface*, *Vehicle System Dynamics* **48**, 1065 (2010).
- [3] L. M. Crespo and D. J. Reinkensmeyer, *Haptic guidance can enhance motor learning of a steering task*, *Journal of Motor Behavior* **40**, 545 (2008).
- [4] Y. Marumo and M. Nagai, *Steering control of motorcycles using steer-by-wire system*, *Vehicle System Dynamics* **45**, 445 (2007).
- [5] Y. Marumo and N. Katagiri, *Control effects of steer-by-wire system for motorcycles on lane-keeping performance*, *Vehicle System Dynamics* **49**, 1283 (2011).
- [6] G. Dialynas, R. Happee, and A. L. Schwab, *Design and implementation of a steer-by-wire bicycle*, in *Proceedings of the 7th Annual International Cycling Safety Conference* (2018).
- [7] E. Sanjurjo, M. A. Naya, J. Cuadrado, and A. L. Schwab, *Roll angle estimator based on angular rate measurements for bicycles*, *Vehicle System Dynamics* **57**, 1705 (2019).
- [8] S. C. Walpole, D. Prieto-Merino, P. Edwards, J. Cleland, G. Stevens, and I. Roberts, *The weight of nations: an estimation of adult human biomass*, *BMC Public Health* **12**, 439 (2012).
- [9] J. K. Moore, J. Kooijman, A. L. Schwab, and M. Hubbard, *Rider motion identification during normal bicycling by means of principal component analysis*, *Multibody System Dynamics* **25**, 225 (2011).

# 6

## Rider control identification in cycling taking into account steer torque feedback and sensorial delays

Corresponding article: G. Dialynas, C. Christoforidis, R. Happee, A. L. Schwab, Rider control identification in cycling taking into account steer torque feedback and sensorial delays, **Submitted**, (2020).

### 6.1. Abstract

An instrumented steer-by wire bicycle designed and built at the TU Delft bicycle laboratory was used to investigate rider responses with and without steering torque feedback. Steering responses and bicycle motions were measured perturbing balance with impulsive forces at the seat post while following a straight lane at unstable ( $2.6$  &  $3.7 \text{ ms}^{-1}$ ) and stable speeds ( $4.5$  &  $5.6 \text{ ms}^{-1}$ ) controlling speed using an electric drive. Responses could well be captured by linear impulse response functions which were consistent across participants. The impulse response functions were used to evaluate rider-bicycle models in their ability to capture human behaviour. The mechanics of the bicycle-rider system were modelled using the Carvallo-Whipple bicycle model extended with rider inertia. A balancing and heading controller was added, capturing visual, vestibular and proprioceptive sensory information using feedback of roll angle, roll angle rate, heading angle, heading angle rate, steering angle and steering torque, taking into account muscular activation dynamics bicycle model extended with rider inertia. Results showed that the rider model followed the necessary stability condition of steer into the fall and

was capable of stabilizing the bicycle. Sensory delays had a negative effect on the model fit, which was resolved with an internal model and prediction algorithm. A model without steer angle and steer velocity feedback could not well capture the human response at the highest speeds and the absence of torque feedback had similar effects for all speeds, supporting the relevance of steer angle and torque feedback in bicycle control. To our knowledge this is the first publication addressing the role of steer torque feedback and sensorial delays by means of a neuromuscular control model.

### Keywords

Bicycle dynamics, manual control, system identification, rider model.

## 6.2. Introduction

The balance and control of a bicycle in motion is a skill that we acquire since our early childhood. Even though the majority of the population knows how to ride a bike, yet the way humans control and balance a bicycle has not been fully understood or quantified from a scientific point of view [1]. From the first appearance of the modern bicycle in the late 1880s until now, dynamic models of uncontrolled bicycles have provided fundamental insights into bicycle stability in relation to speed and geometry [2, 3]. However, additional knowledge into human control is required not only to design safer bicycles but also to assess new safety systems (e.g. steer assist functionalities). In depth-analyses of the rider sensory dynamics including delays and thresholds are necessary to probe the dynamics of rider-bicycle balance control.

Research in the field of cybernetics started in the 1950s to advance aircraft technology and understand pilot control. McRuer and Krendel [4] were amongst the first to model the human operator as a servo system element with time delay. The so called "McRuer cross over model" was later extended to the "McRuer precision model" which accounted for low frequency neuromuscular lags [5]. Results showed that the humans compensate the system to create an open-loop first-order integrator near the systems cross-over frequency. Among the first researchers who focused on the manual control of bicycles were Van Lunteren et al. [6]. They used a stationary bicycle simulator and system identification techniques to identify the parameters of a proportional–integral–derivative (PID) rider controller with delay at a constant forward speed of  $4.2 \text{ ms}^{-1}$ . However, their bicycle simulator had no visual display and the obtained controller has not been experimentally validated. Massing and Roland [7, 8] developed a bicycle stability and path following torque controller. The controller consisted of an inner and outer loop responsible for roll stabilization and lateral tracking. Stabilization was achieved with a PID controller with delay, whereas tracking employed a simple proportional controller. Results showed adequate performance but the model was not yet validated. Weir [9] developed a cross-over model for Sharp's [10] motorcycle model. He tried to identify the transfer functions for different control input–output relations. From his analysis it was concluded that a simple linear steer torque controller that takes into account the lean angle is sufficient for balancing a motorcycle in motion. Eaton [11] later

conducted experiments to validate the theoretical motorcycle model of Sharp et al. [10] with the rider model of Weir [9]. Despite the fact that he excluded the lean torque and used only the lean angle stabilization loop as a control input to the rider model below the stable speed region, results were promising. Low uncertainty was present in the estimated control parameters, and steer torque responses were fitted well. Jason Moore [12] in his PhD thesis focused on identifying rider control during simple bicycle maneuvers. He constructed an instrumented bicycle capable of measuring accurately the applied steer torque and conducted a series of lateral perturbation experiments on a treadmill and on a pavilion floor. The large amount of data collected during the experimental tests were used to identify both the plant and control model of the underlying system. Some of the methods and modelling approaches that he utilized in his thesis were also adopted herein. Hess et al. [13] introduced task independent handling quality metrics for bicycle control. Using these metrics, they developed a rider model with five gains, two second-order filters, and a preview time. Soudbakhsh et al. [14] mounted a stationary bicycle on top of a motion platform and applied lateral sweep perturbations to capture the rider's responses. Their conclusion was that it is impossible to stabilize the stationary bicycle only with upper body movements. With additional steering control the riders can balance the bicycle under three delays in the neurological system. Chu et al. [15] measured the steering and roll angle of a bicycle and used a model predictive controller as a rider model to control the bicycle by applying steering and leaning torques. Wang et al. [16] conducted experiments in order to analyse the stability and control of a rider-bicycle system and developed a human control model for the body lean torque. Schwab et al. [17] modelled the bicycle rider using lateral force perturbation experiments to explore the potential feedback of sensory cues during the bicycle balancing task. A rider control model which is inherently limited by neuromuscular lags was developed. Even though, the rider control model seemed to mimic human control in a natural way, there were limitations in this study. The experiments were conducted on a narrow treadmill and as reported this may have created bias in the control behaviour. A single effective time delay was initially incorporated in the model to attribute sensory delays but was ultimately removed for successful numerical identification. To enhance the findings and results of Schwab et al. [17] study, we conduct lateral force perturbation experiments in a wide cycling path using the instrumented steer-by-wire bicycle developed by Dialynas et al. [18]. Next, we reconfigure the parameters of the Carvallo-Whipple bicycle model [2] to the physical properties of the experimental bicycle and design a new rider control model.

This study has three main objective; the first is to design a rider control model which takes into account steer torque feedback and sensorial delays. To achieve this we include an internal control model (ICM), as frequently employed in human motor control studies to compensate delays [19–22]. The second is to examine the ability of humans to adapt to altered steering dynamics even when feedback is intermittent and delayed. The third is to evaluate the effect of handlebar torque and position feedback during the balancing task. We validate three models of increasing complexity using experimental data collected by Dialynas et al. [23]. Two metrics

are used to assess the performance of each model and to analyse the impact of torque feedback on rider control. The covariance coefficient (CV) of the estimated controller parameters is used as a measure of uncertainty, whereas the variance accounted for (VAF) as a measure of discrepancy between the simulated and actual responses. The paper is organized as follows: First, the experimental set-up and experimental procedure are presented. Next, the methods and results, are presented. The article ends with a discussion and conclusion section highlighting the main findings of this research. A preliminary analysis of this research data was published as an MSc thesis [24]. All data presented herein have been reanalysed and results were further extended.

## 6.3. Methods

### 6.3.1. Description of experimental set-up

At TU Delft we designed and built a steer-by-wire bicycle [18] equipped with multiple sensors measuring most bicycle states and rider control inputs required for identification (see Figure 6.1). A pulling rope mechanism with a force transducer in series was used to manually apply lateral impulsive forces at the seat post (see Figure 6.3). The bicycle is equipped with rear wheel hub motor and a cruise control system, so the subjects did not need to pedal during the experiments to maintain a constant speed. Measurements of the inertial measurement unit (IMU), steering angle encoder, torque sensor and rope force transducer were logged with a sampling frequency  $F_s$  of 1000 Hz. Steering angle  $\delta$  was directly measured from the absolute encoder of the upper front assembly, while the roll angle  $\phi$  was estimated from the measured roll rate  $\dot{\phi}$  according to the methodology described by Sanjurjo et al. [25].

### 6.3.2. Description of steer-by-wire controller

To minimize the difference between the handlebar  $\delta$  and fork angle  $\theta$  of the steer-by-wire system, two proportional-derivative (PD) controllers are implemented. This way an action-reaction torque is applied at the handlebar  $T_{PDH}$  and fork  $T_{PDF}$  and a similar behaviour to an ordinary mechanically steered bicycle is achieved [18]. The double PD-controllers are formed as,

$$T_{PDH} = K_{PH}(\delta - \theta) + K_{DH}(\dot{\delta} - \dot{\theta}) \quad (6.1)$$

$$T_{PDF} = K_{PF}(\delta - \theta) + K_{DF}(\dot{\delta} - \dot{\theta}), \quad (6.2)$$

where  $K_{PH} = 0.9$ ,  $K_{PF} = 2$  Nm/rad are the proportional and  $K_{DH} = 0.012$ ,  $K_{DF} = 0.025$  Nms/rad are the derivative gains of the handlebar and fork assembly.  $\dot{\delta}$ ,  $\dot{\theta}$  are the handlebar and fork rates, which are estimated by taking the time derivative of the directly measured angles, for a fixed time interval of 1 ms.

The steer-by-wire system enables flexible adjustment of steering actions and haptic feedback (steering torque). In this paper the controller was programmed to approximate: 1) normal steering motion with normal steering torque (haptics on) and 2)



Figure 6.1: Steer-by-wire bicycle prototype with handlebar and fork actuators, sensors, pulling rope mechanism, digital controller and custom made battery pack.

normal steering motion with minimal steering torque ( $K_{PH}$  and  $K_{DH} = 0$ ), isolating the rider from torques resulting from tyre to road interaction (haptics off).

### 6.3.3. Procedure

Eighteen males and two females (age =  $26 \pm 2$  years) volunteered in this study. To assure safety, all participants were requested to wear protective equipment, which includes a standards-approved bike helmet, knee and elbow pads. All subjects gave informed consent according to the guidelines of the human research ethics committee of Delft University of Technology. They reported that they did not experience any kind of pain or injury in the year before the experiments. The mean weight of the participants ( $82.1 \pm 6.4$  kg) was selected to be close to the European population [26], whereas the height ( $181 \pm 7$  cm) was close to the mean height of young European men [27].

Each experimental trial consisted of four different speeds (i.e., 2.6, 3.7, 4.5, 5.6  $\text{ms}^{-1}$ ) covering both the stable and the unstable forward speed range. Two individual trials were performed in random order for every speed. In one trial steering feedback was enabled (haptics on), whereas in the other trial steering feedback was disabled (haptics off). Every trial had a duration of approximately 60 seconds, with on average a total of 12 lateral perturbations. An example of the data measured for one subject at the lowest speed are presented in Figure 6.2.

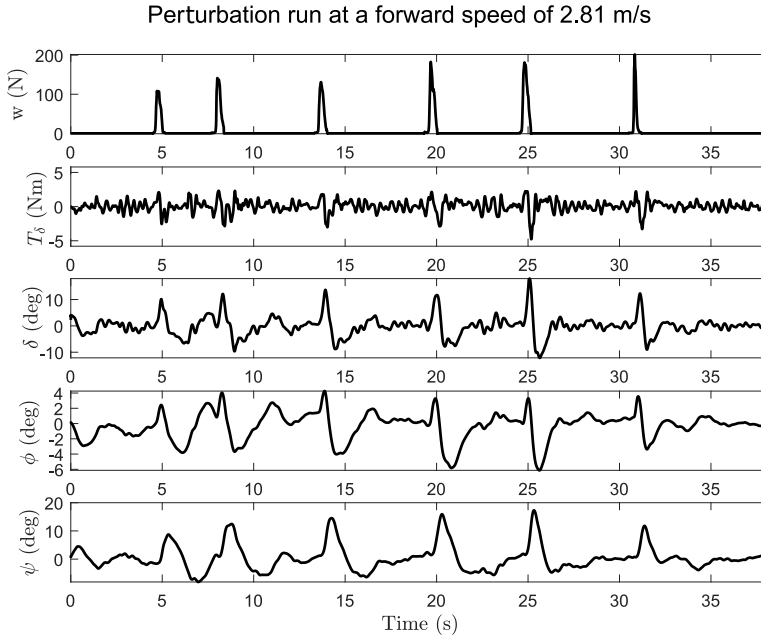


Figure 6.2: Example measurements of the lateral disturbance force  $w$ , rider applied steer torque  $T_\delta$ , steer angle  $\delta$ , roll angle  $\phi$  and heading  $\psi$  at a forward velocity of  $2.81 \text{ ms}^{-1}$  (first 40 seconds).

All experiments were performed at a straight cycling path at the Heertjeslaan on the TU Delft campus during the summer of 2019. The subjects were requested to ride the steer-by-wire bicycle in all aforementioned speeds while being laterally perturbed with impulsive forces at the seat post. An additional bicycle was used by the experiment coordinator to cycle next to the instrumented steer-by-wire bicycle and perturb the subject (see Figure 6.3). A set-up which allowed both push and pulls was initially tested but the pushes were subject to inconsistencies. After inspecting the data of the pilot runs, it was observed that unilateral disturbances did not affect the predictability of the perturbation, as the responses of the subjects were similar. For this reason, the unilateral approach was chosen. To avoid any feedforward control behaviour (e.g. seeing the coordinator preparing to pull the rope) all subjects were asked to focus on the road ahead.

## 6.4. System model

The system consists of a bicycle and rider model. For the bicycle we selected the Carvallo-Whipple model [2], whereas for the rider model we examine three different linear feedback control approaches with increasing complexity and sensory delays.



Figure 6.3: Experimental trial performed at TU Delft; The experiment coordinator (left) cycling next to the steer-by-wire bicycle (right) applies an impulsive lateral force with a rope.

### 6.4.1. Bicycle model

The Carvallo-Whipple bicycle model [2] consists of four rigid bodies: a rear frame  $B$  which includes the rider as a rigid mass with no hands on the handlebars, a front frame  $H$  which consists of the handlebar and fork assembly and a front wheel  $F$  (see Figure 6.4). The bodies are connected together with in total three resolute joints, one for each wheel and one for the connection of the rear and front frame. The contact between the wheels and the surface is modelled by holonomic constraints in the normal direction and by non-holonomic constraints in the longitudinal and lateral directions with zero longitudinal and lateral slip. The resulting bicycle model has three velocity degrees-of-freedom, the forward speed  $v$ , the rear frame roll rate  $\dot{\phi}$  and the steering rate  $\dot{\delta}$ .

According to Meijaard et al. [2] for small perturbations the lateral bicycle motions can be described by two coupled second order differential equations:

$$\mathbf{M}\ddot{\mathbf{q}} + v\mathbf{C}_1\dot{\mathbf{q}} + [g\mathbf{K}_0 + v^2\mathbf{K}_2]\mathbf{q} = \mathbf{f} \quad (6.3)$$

where the time-varying variables are the roll and steer angle  $\phi$ ,  $\delta$  and roll and steer torque  $T_\phi$ ,  $T_\delta$  represented by two vectors  $\mathbf{q}$ ,  $\mathbf{f}$ , respectively. The coefficients in this equation are: a constant symmetric mass matrix,  $\mathbf{M}$ , a damping-like matrix,  $v\mathbf{C}_1$ , which is linear in the forward speed  $v$ , and a stiffness matrix which is the sum of a constant symmetric part due to gravity,  $g\mathbf{K}_0$ , and a part,  $v^2\mathbf{K}_2$ , which is quadratic in the forward speed. The forces on the right-hand side,  $\mathbf{f}$ , are the generalized

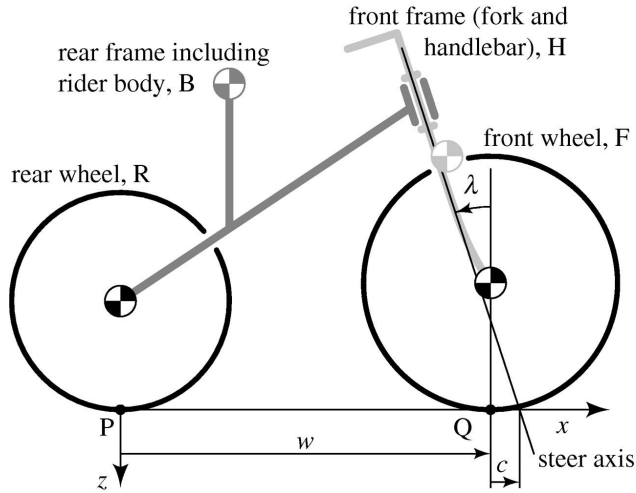


Figure 6.4: The bicycle model consists of four rigid bodies: a rear frame B which includes the rider as a rigid mass with no hands on the handlebars, a front frame H which consists of the handlebar and fork assembly and a front wheel F. The bodies are connected together with in total three resolute joints, one for each wheel and one for the connection of the rear and front frame. The center of mass locations are expressed relative to the  $x$  and  $z$  coordinates shown (with origin at P and  $y$  pointing towards the reader). Other parameters are the body masses and inertias, the steer axis tilt  $\lambda$ , wheelbase  $w$  and trail  $c$ .

6

forces.

To capture the full bicycle motion several additional states were defined. For the forward motion, the angular rates of the front and rear wheels were determined as,  $\dot{\theta}_R = -v/r_R$ ,  $\dot{\theta}_F = -v/r_F$ , where  $\theta_R$  and  $\theta_F$  are the rear and front wheel angles and  $r_R$  and  $r_F$  are the wheel radius, respectively. For the lateral dynamics the heading (yaw) angle  $\psi$  and lateral displacement of the rear  $y_P$  and front wheel  $y_Q$  contact point are calculated:

$$\dot{\psi} = \frac{v\delta + c\dot{\delta}}{w} \cos \lambda \quad (6.4)$$

$$\dot{y}_P = v\psi \quad (6.5)$$

$$\dot{y}_Q = \dot{y}_P + w\dot{\psi} - c\dot{\delta} \cos \lambda_s \quad (6.6)$$

with wheelbase  $w$ , trail  $c$  and steer axis tilt  $\lambda_s$ . During our balance experiments, the contribution of the visual heading cues on the bicycle trajectory could not be neglected, for this reason the state vector of Equation 6.3 is extended to include heading by adding the yaw rate Equation 6.4 to the set of equations of motion.

The entries in the constant coefficient matrices  $\mathbf{M}$ ,  $\mathbf{C}_1$ ,  $\mathbf{K}_0$  and  $\mathbf{K}_2$  can be calculated from a non-minimal set of 25 bicycle parameters as described by Meijaard et al. [2]. A procedure similar to Moore et al. [28] was used to measure the parameters of the steer-by-wire bicycle of Figure 6.1. The measured parameters are presented in Table 6.8 of the Appendix I. To model the dynamics of the steer-by-wire in the haptics off configuration we decouple the roll and steer dynamics. The handlebars then act as a steer angle command, with only force feedback from the inertia of the handlebars. The entries in the constant coefficient matrices of Equation 6.3 then become:

$$\begin{aligned} \mathbf{M} &= \begin{bmatrix} M_{11} & M_{12} \\ 0 & I_{H_{xz}} \end{bmatrix}, & \mathbf{C}_1 &= \begin{bmatrix} C_{111} & C_{112} \\ 0 & 0 \end{bmatrix} \\ \mathbf{K}_0 &= \begin{bmatrix} K_{011} & K_{012} \\ 0 & 0 \end{bmatrix}, & \mathbf{K}_2 &= \begin{bmatrix} 0 & K_{212} \\ 0 & 0 \end{bmatrix} \end{aligned} \quad (6.7)$$

where  $I_{H_{xz}}$  in this case is the mass moment of inertia of only the handlebar assembly. Table 6.9 shows the selected coefficients of the haptics on/off configurations.

To determine the stability of the straight-ahead steady motion, exponential motions of the form  $q = q_0 \exp(\lambda t)$  are assumed. Then in combination with Equation 6.3 the characteristic polynomial equation can be formed,

$$\det(\mathbf{M}\lambda^2 + v\mathbf{C}_1\lambda + g\mathbf{K}_0 + v^2\mathbf{K}_2) = 0 \quad (6.8)$$

and the eigenvalues  $\lambda$  can be calculated for the haptics on/off configurations (see Figure 6.5). For the haptics on there are in total four eigenmodes. Two are important for stability and are usually referred as the weave and capsize modes. The weave is an oscillatory mode as can be seen by the existence of imaginary parts and represents a motion in which the bicycle sways about its heading. The oscillatory motions exponentially fades when forward speed is larger than  $4.39 \text{ ms}^{-1}$ . The capsize mode on the other hand has an eigenvector dominated by lean and leads to a gradual roll drift to infinity when the eigenvalue crosses the zero line around  $6.67 \text{ ms}^{-1}$ . The third eigenmode is the overall stable castering mode. This mode has a large negative real eigenvalue with an eigenvector dominated by steering. The eigenvalues corresponding to the kinematic differential equations are all zero and correspond to changes in the rotation angles of the wheels, a constant yaw angle and a linearly increasing lateral displacement. For the haptics off configuration the handlebar dynamics are decoupled from the fork, the response of the steering assembly is no longer speed dependant and for this reason the bicycle is unstable in all speeds.

#### 6.4.2. State space representation

For control purposes Equation 6.3 is expressed in state space form:

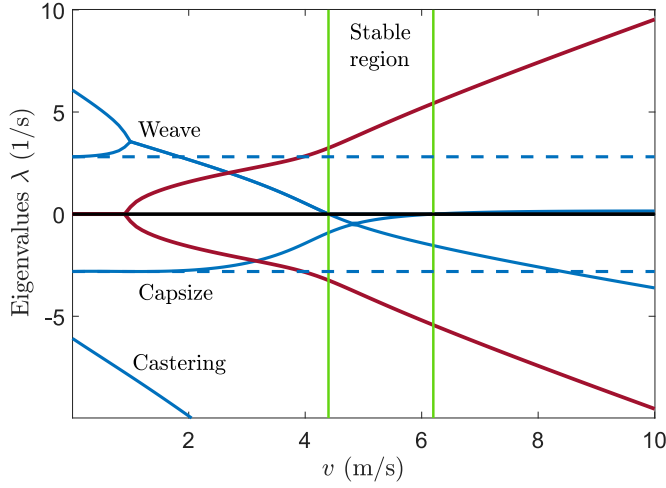


Figure 6.5: Root locus plot of the instrumented steer-by-wire bicycle (see Figure 6.1). Solid blue and red lines indicate the real and imaginary part of the eigenvalues  $\lambda$  for the haptics on configuration, while dashed blue line the eigenvalues  $\lambda$  for the haptics off configuration. For the haptics on the stable region corresponds to speeds  $4.39 \lesssim v \lesssim 6.67 \text{ ms}^{-1}$ , whereas for the haptics off the bicycle is always unstable.

6

$$\dot{\mathbf{x}}_{\mathbf{b}} = \mathbf{A}_{\mathbf{b}}\mathbf{x}_{\mathbf{b}} + \mathbf{B}_{\mathbf{b}}\mathbf{f} + \mathbf{H}_{\mathbf{d}}\mathbf{w} \quad (6.9)$$

$$\mathbf{y}_{\mathbf{b}} = \mathbf{C}_{\mathbf{b}}\mathbf{x}_{\mathbf{b}} + \mathbf{D}_{\mathbf{b}}\mathbf{f} \quad (6.10)$$

with state vector  $\mathbf{x}_{\mathbf{b}} = [\dot{\phi}, \dot{\delta}, \phi, \delta, \psi]^T$ , generalized forces  $\mathbf{f} = [T_{\phi}, T_{\delta}]^T$ , lateral force input vector  $\mathbf{w} = [w]$  and output vector  $\mathbf{y}_{\mathbf{b}}$  equal to the full state. We assume no applied generalised roll torque,  $T_{\phi} = 0$ . The system matrix  $\mathbf{A}_{\mathbf{b}}$ , input gain matrix  $\mathbf{B}_{\mathbf{b}}$ ,  $\mathbf{H}_{\mathbf{d}}$  lateral disturbance matrix, observer matrix  $\mathbf{C}_{\mathbf{b}}$  and direct feed-through matrix  $\mathbf{D}_{\mathbf{b}}$  are defined as:

$$\mathbf{A}_{\mathbf{b}} = \begin{bmatrix} -\mathbf{M}^{-1}v\mathbf{C}_1 & -\mathbf{M}^{-1}(g\mathbf{K}_0 + v^2\mathbf{K}_2) \\ \mathbf{I}_{2 \times 2} & \mathbf{0} \\ 0 & \frac{c \cdot \cos \lambda}{w} & 0 & \frac{v \cdot \cos \lambda}{w} \end{bmatrix},$$

$$\mathbf{B}_{\mathbf{b}} = \begin{bmatrix} \mathbf{M}^{-1} \\ \mathbf{0} \end{bmatrix},$$

$$\mathbf{C}_{\mathbf{b}} = \mathbf{I}_{5 \times 5}, \mathbf{D} = \mathbf{0}, \quad (6.11)$$

$$\mathbf{H}_{\mathbf{d}} = \begin{bmatrix} \mathbf{M}^{-1} \begin{bmatrix} l_g \\ c_s \end{bmatrix} \\ \mathbf{0} \end{bmatrix},$$

In the  $\mathbf{H}_a$  matrix the coefficients  $l_g$  and  $c_s$  transform the lateral perturbation force  $w$  to the generalized torques  $T_\phi$  and  $T_\delta$ , and were derived by a virtual work approach. The coefficient  $l_g$  can be identified as the moment arm and is equal to 0.84 m. For the haptics on configuration, the coefficient  $c_s$  was 0.01 m, whereas for the haptics off, this coefficient was set to 0, since the roll and steer dynamics are then decoupled.

### 6.4.3. Rider control model

The rider model architecture consists of four main blocks in series (i.e. the delay, the predictor, the linear gain controller and the neuromuscular dynamics ) that represent the human control process sensing, reasoning and actuation. To obtain a complete sensory input to the rider model the bicycle states were further extended with the steer torque  $T_\delta$ , which comes as an output of the neuromuscular dynamics of the rider arms. The output states attributed to the proprioceptive, visual and vestibular system were delayed taking into account perception and neural delays presented in Table 6.1. For the steering angle, steering angle rate (muscle spindles) and steer torque (golgi tendon organs) the selected delays were based on previous studies conducted by Van der Helm et al. [29] and De Vlugt et al. [30]. For the roll angle and heading (yaw) angle (visual) the delays were selected in agreement with Kawakami et al. [31], whereas for the roll rate (vestibular) the delay was selected according to Barnett et al. [32].

Table 6.1: Sensory motor delays.

Bicycle states	Delay (ms)
$\delta$	25
$\dot{\delta}$	25
$T_\delta$	25
$\phi$	200
$\psi$	200
$\dot{\phi}$	50

A prediction algorithm which includes an internal model of the bicycle and neuromuscular dynamics was used to simulate how the central nervous deals with sensory delays and estimates the current state integrating applied control inputs. The predicted states were fed through the gain block which includes six free parameters (one for each bicycle state), estimated as described in the Section [Parameter estimation](#). The produced neural output was filtered through the neuromuscular dynamics block which gives as an output the rider steer torque  $T_\delta$ . The high level overview of the obtained rider-bicycle system can be seen in Figure 6.6.

### 6.4.4. Neuromuscular dynamics

To simulate the limitations of the rider's arm responses a second order system was used as a neuromuscular model similar to the approach adopted by Jason Moore in his PhD thesis [12]. The model used activation dynamics estimated for

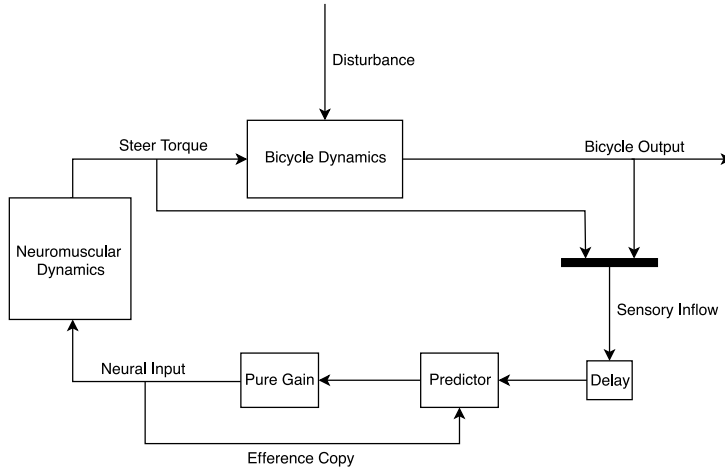


Figure 6.6: High level overview of the rider-bicycle model.

the shoulder joint from previous studies [33, 34]. The state space representation of the neuromuscular model is expressed as,

$$\dot{\mathbf{x}}_{\text{nm}} = \mathbf{A}_{\text{nm}}\mathbf{x}_{\text{nm}} + \mathbf{B}_{\text{nm}}a \quad (6.12)$$

$$\mathbf{y}_{\text{nm}} = \mathbf{C}_{\text{nm}}\mathbf{x}_{\text{nm}} \quad (6.13)$$

$$\mathbf{A}_{\text{nm}} = \begin{bmatrix} 0 & 1 \\ -\omega_c^2 & -2\zeta\omega_c \end{bmatrix}$$

$$\mathbf{B}_{\text{nm}} = \begin{bmatrix} 0 \\ \omega_c^2 \end{bmatrix}$$

$$\mathbf{C}_{\text{nm}} = [1 \quad 0]$$

where  $\mathbf{x}_{\text{nm}} = [T_\delta \quad \dot{T}_\delta]^T$  is the state and  $\mathbf{y}_{\text{nm}}$  is the output of the neuromuscular system with cut-off frequency  $\omega_c = 2.17 \cdot 2\pi \text{ rad s}^{-1}$ , damping coefficient  $\zeta = \sqrt{1/2}$  and neural input  $a$ . The model acts as a critically damped second-order filter with a cut-off frequency equal to  $\omega_c$ .

#### 6.4.5. Combined plant model

The bicycle dynamics state space representation was combined with the neuromuscular dynamics. A similar methodology and notation as the one adopted by Jason Moore in his thesis [12] are also followed herein in order to produce the extended plant dynamics:

$$\dot{\mathbf{x}} = \mathbf{A}\mathbf{x} + \mathbf{B}a + \begin{bmatrix} \mathbf{H}_d \\ \mathbf{0}_{2 \times 1} \end{bmatrix} w \quad (6.14)$$

$$\mathbf{y} = \mathbf{C}\mathbf{x} \quad (6.15)$$

$$\mathbf{A} = \begin{bmatrix} \mathbf{A}_b & \mathbf{B}_{b_{i,2}} \mathbf{C}_{nm} \\ \mathbf{0}_{0 \times 5} & \mathbf{A}_{nm} \end{bmatrix}, \quad i = 1, \dots, 5$$

$$\mathbf{B} = \begin{bmatrix} \mathbf{0}_{5 \times 1} \\ \mathbf{B}_{nm} \end{bmatrix}$$

$$\mathbf{C} = \begin{bmatrix} \mathbf{I}_{6 \times 6} & \mathbf{0}_{6 \times 1} \\ \mathbf{0}_{1 \times 6} & 0 \end{bmatrix}$$

where state vector  $\mathbf{x} = [\dot{\phi}, \delta, \phi, \psi, T_\delta, \dot{T}_\delta]^T$ ,  $\mathbf{y}$  the output vector consisting of the sensory inflow feedback and neural signal  $a$  being the control input.

#### 6.4.6. Sensory delay reafferent optimal predictor (SDROP)

To compensate the effect of sensory delays and achieve an adequate rider control performance, we explored the use of internal predictive models. Several authors have proposed that the cerebellum functions as a predictor of body motion. Miall et al. [35] suggested that the cerebellum may hold at least two separate Smith Predictors. The Smith predictor is a basic prediction scheme in control theory [36]. The Smith predictor compensates for time delays using a forward model of the controlled dynamics and an internal model of the sensory delays. The forward model utilizes an efferent signal being the applied neural control input  $a$ . The comparison between prediction and measurement simulates the human's ability to distinguish between reafference and exafference. Unfortunately, the Smith predictor does not work for unstable open loop systems [36] such as the Carvallo-Whipple bicycle model [2]. As a consequence, further adjustments were made to the Smith predictor. The forward model was replaced by a discrete optimal predictor (DOP) which was further adapted to work with different time delays (Table 6.1). A comparison between the conventional DOP and adapted SDROP is presented in Figure 6.11 (a), (b) of Appendix I. The SDROP used additional delays to synchronize the input states and an internal model to forward the bicycle states in time. The predicted state estimates and current bicycle states were compared and subtracted from each other. The resulting error was added to the former estimates (reafferent correction) for optimization. The SDROP required full state feedback, but in our extended bicycle model only 6 out of 7 states are sensed. The missing  $T_\delta$  was estimated by the predictor. To detect disturbance effects, which are not captured by the efference copy, we utilized the same correction principle as the one used in the Smith predictor [36]. The low level overview of the rider controller and bicycle plant can be seen in Figure 6.7.

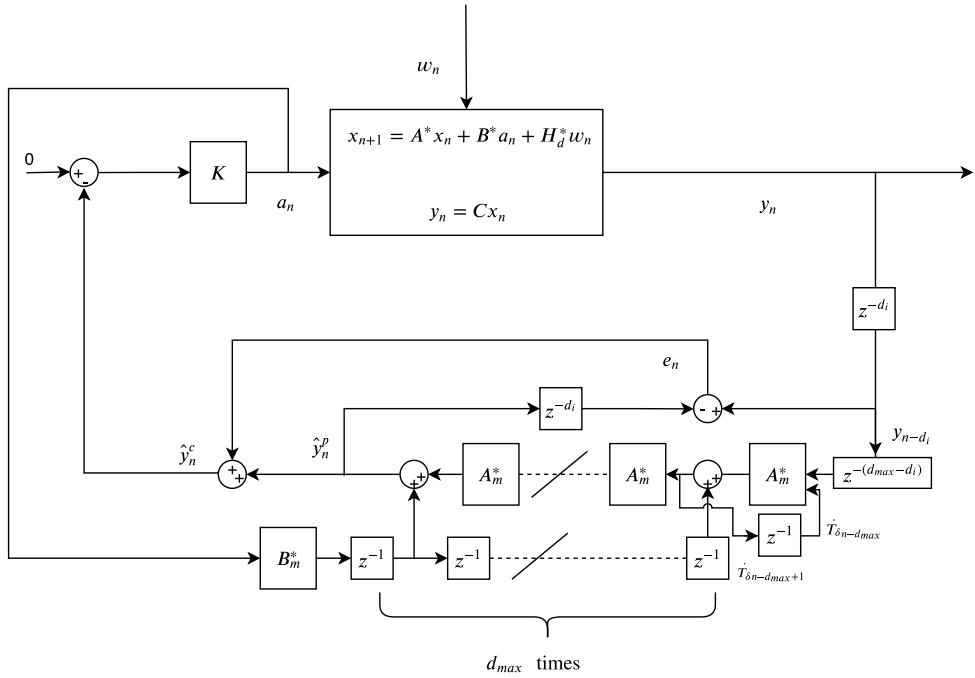


Figure 6.7: Low level overview of the rider-bicycle system. Matrices  $A^*$ ,  $B^*$ ,  $H_d^*$  are the discretized matrices of the extended plant dynamics,  $d_i$  is the amount of delay in times steps per sensory channel and  $d_{max}$  the maximum value of those. Matrices  $A_m^*$ ,  $B_m^*$  express the dynamics of the internal model of the process.  $\hat{y}^p$ ,  $\hat{y}^c$  symbolize the undelayed and delayed estimates of the output states, respectively.  $e$  is the error between the predicted and delayed states (Smith correction) and  $K$  is a pure gain block containing all six gains.  $a$  represents the neural signal send to the rider arm muscles.

## 6.5. System identification

The rider control system identification used a combination of black box and gray box models to identify the numerical values of the control gains employed by the rider. Starting with the basic measurements, the identification was performed in six steps:

1. **Data preparation:** There were two datasets available for our analysis (haptics on and haptics off). An in depth comparison of these conditions is presented by Dialynas et al. [23]. A dependent paired sample t-test was conducted to compare if there was significant difference (95% confidence interval) in steering effort between conditions for all speed levels. The steering angle power spectrum was analogous and almost identical impulse response functions (IRFs) were reported. Hence only the haptics on dataset was selected for modelling. This dataset was split into two data clusters. The cluster with the first 10 subjects was used for "identification" of the controller gains, and the cluster with the last 10 subjects for "validation" of the model output.
2. **Black box identification:** To produce the filtered impulse response (IRF),

finite impulse response (FIR) models were fitted to the four output states  $y$  in response to the lateral force  $w$  for each run.

3. **Filtering:** The IRFs  $h_\delta(t)$ ,  $h_\phi(t)$ ,  $h_\psi(t)$ ,  $h_{T_\delta}(t)$  were filtered using a zero-phase low pass filter with a cut-off frequency of 10 Hz.
4. **Median response:** The individual responses of the “identification” and “validation” datasets were averaged in order to produce two mean IRFs. Each individual subject response was compared with the mean. The subject with the best fit (highest VAF) for all runs was selected as the median rider for both datasets. We could also have used the two mean raw measurements to identify the median rider for the two aforementioned datasets but this was avoided due to the fact there was too much unwanted information in the experiments which was not directly attributed to the impulse perturbation. All results described herein were based on the median rider response IRFs, since intersubject variability was low at  $\pm 8\%$ .
5. **Black box filtering:** The IRFs of the median subject was convolved with the measured disturbances of each run to produce the non-parametric output states  $\tilde{y}_\delta(t)$ ,  $\tilde{y}_\phi(t)$ ,  $\tilde{y}_\psi(t)$ ,  $\tilde{y}_{T_\delta}(t)$ .
6. **Gray box identification:** A gray box model with a maximum of six free parameters (one gain for each bicycle state feedback loop plus one for the steer torque) was fitted to the the non parametric outputs  $\tilde{y}_\delta$ ,  $\tilde{y}_\psi$  given the measured external input  $w$ .

These individual steps are explained in detail in the following sections.

### 6.5.1. Black box model

To remove the effects of unwanted disturbances and noise, the measured steering angle  $\delta$ , roll angle  $\phi$ , heading  $\psi$  and steer torque  $T_\delta$  signals were approximated by a FIR model. The impulse response function  $h(t)$  was convolved with external input  $w(t)$  to produce the filtered output response  $\tilde{y}(t)$ . The output data represent the input to output relationship corresponding to either  $h_\delta(t)$ ,  $h_\phi(t)$ ,  $h_\psi(t)$ ,  $h_{T_\delta}(t)$ . In finite discrete time;  $t = 1, 2, 3, \dots, N$  the measured output  $y(t)$  is given by,

$$y(t) = \tilde{y}(t) + v(t) \quad (6.16)$$

$$\tilde{y}(t) = \sum_{k=1}^m h(k)w(t-k) \quad (6.17)$$

where  $m$  is the sample length of the impulse response function and  $v(t)$  is the remnant caused by the unwanted disturbances. Experimenting with different finite impulse lengths, the oscillations were found to die out after  $m = 798$  samples, which corresponds to a finite response length of 3.08 seconds. In state space form Equations 6.16, 6.17 are expressed as,

$$y = Wh + v \quad (6.18)$$

where  $W$  is the matrix containing time shifted versions of the the input signal.

$$W = \begin{bmatrix} w(0) & 0 & 0 & \dots & 0 \\ w(1) & w(0) & 0 & \dots & 0 \\ w(2) & w(1) & w(0) & \dots & 0 \\ \vdots & \vdots & \vdots & \ddots & \vdots \\ w(N-1) & w(N-2) & w(N-3) & \dots & w(N-N) \end{bmatrix} \quad (6.19)$$

Since Equation 6.18 is linear in the coefficients a unique solution can be found by the least squares method.

$$h = (W^T W)^{-1} W^T y \quad (6.20)$$

6

The estimated IRFs were further filtered using a eight-order Butterworth filter with cut-off frequency of 10 Hz. All input signals were convolved with  $h$  in order to remove noise and produce an estimate of the output signals  $\hat{y}$ . An example of obtained responses of the mean and median rider for the lowest measured forward velocity is presented in Figure 6.8.

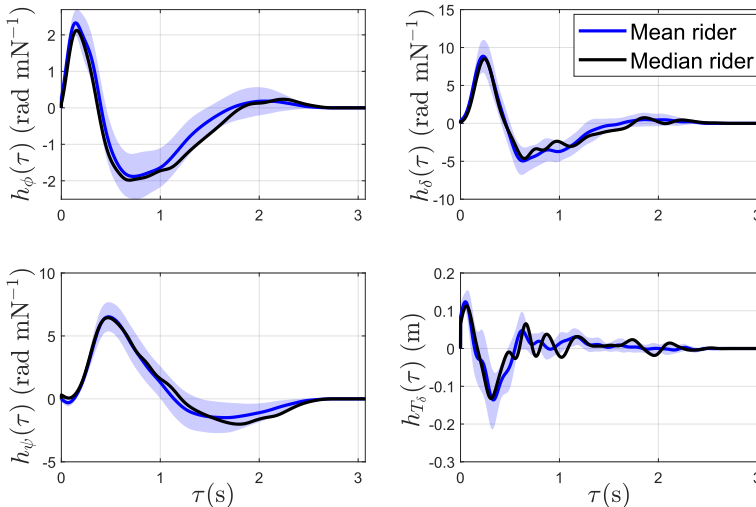


Figure 6.8: IRFs for the roll angle  $\phi$ , steering angle  $\delta$ , heading angle  $\psi$  and steer torque  $T_\delta$  for a forward velocity of  $v = 2.8 \text{ ms}^{-1}$ , shade = SD of mean over participants (haptics on).

### 6.5.2. Gray box model

The rider control model includes six unknown linear feedback control gains. In state space the gain block of Figure 6.6 can be expressed as a vector of the following form,  $\mathbf{K} = [K_{\phi}, K_{\delta}, K_{\dot{\phi}}, K_{\dot{\delta}}, K_{\psi}, K_{T_{\delta}}]^T$ . As feedback is defined as negative the control input is given by:

$$a = -\mathbf{K}\hat{\mathbf{y}}^c \quad (6.21)$$

where  $\hat{\mathbf{y}}^c$  is the output of the predictor (see figure 6.7).

### 6.5.3. Parameter estimation

The gains of the rider control model were estimated by fitting the model outputs into the convolved filtered IRFs. This was achieved minimizing the following cost function:

$$V_N(\mathbf{K}) = \frac{1}{N} \sum_{t=1}^N \left[ 0.8 \frac{(\hat{y}_{\delta}(t, \mathbf{K}) - \tilde{y}_{\delta}(t))^2}{(\bar{y}_{\delta})^2} + 0.16 \frac{(\hat{y}_{\psi}(t, \mathbf{K}) - \tilde{y}_{\psi}(t))^2}{(\bar{y}_{\psi})^2} + 0.04 \frac{(\hat{y}^{T_{\delta}}(t, \mathbf{K}))^2}{(\bar{y}_{T_{\delta}})^2} \right] \quad (6.22)$$

where  $\mathbf{K}$  is a vector containing all free feedback control gains and  $\hat{y}_{\delta}$ ,  $\hat{y}_{\psi}$  and  $\tilde{y}_{\delta}$ ,  $\tilde{y}_{\psi}$  are the simulated and non-parametric outputs, respectively. The constant scaling factors  $\bar{y}_{\delta}$ ,  $\bar{y}_{\psi}$  and  $\bar{y}_{T_{\delta}}$  are the absolute allowable magnitude limits, which are equal to 0.4 rad for the two angles and 10 Nm for the steering torque.

The first two terms of the cost function are trying to match the steering and heading responses of the parametric model with those of the non-parametric model. The third term minimizes the magnitude of input torque in order to optimize fitting, while minimizing the control effort. If this term was omitted it led to oscillatory responses in the steering angle and unrealistic input torques, due to the double differentiation to get from position to torque. Roll responses were not fitted due to systematic deviations between the predicted and actual responses (read Discussion Section for further explanation). All weights of the cost function were chosen heuristically, the weight ratio of the heading and steer error was selected as 1:5, since this gave the best possible fitting. For optimization a genetic algorithm (fitness limit = 0.03, crossover fraction = 0.85, and population size = 10 times bigger the size of the parameter length) was used to initialize the process for the gradient descend algorithm to estimate the global minimum of the gains.

Most estimated gains of the gray box model were negative, producing torques opposed to the state direction. Due to the fact that the rider was expected to act

like a restoring steering stabilizer with finite stiffness and damping properties, all gains associated to the arm muscle spindles ( $K_\delta, K_\delta$ ) were constrained to be only positive. At the same time, the heading and roll gains ( $K_\psi, K_\phi$ ) were constrained between -250 and 250  $\text{kg m}^2 \text{s}^{-1}$ , because if they were left unconstrained they drive the whole gain vector to unrealistic values without any noticeable improvement on fitting performance.

#### 6.5.4. Performance metrics

As metric of model validity the variance accounted for between the parametric and non-parametric output was calculated as,

$$\text{VAF}_d(\mathbf{K}) = 1 - \frac{\sum_{t=1}^N (\hat{y}_d(t) - \hat{y}_d(t, \mathbf{K}))^2}{\sum_{t=1}^N (\hat{y}_d(t)^2)} \quad (6.23)$$

with  $d$  being any of the roll  $\phi$ , steer  $\delta$  and heading  $\psi$  outputs. To quantify the uncertainty of each parameter the covariance matrix was first estimated as,

$$\text{cov}_{ij}(\hat{\mathbf{K}}) = V_N(\hat{\mathbf{K}})H_{ij}(\hat{\mathbf{K}})^{-1} \quad (6.24)$$

where the hessian matrix  $\mathbf{H}$  was calculated by the gradient descend algorithm as,

$$\mathbf{H}(\hat{\mathbf{K}}) = H_{ij}(\hat{\mathbf{K}}) = \frac{\partial^2 V_N}{\partial K_i \partial K_j} \quad (6.25)$$

where  $\hat{\mathbf{K}}$  in both Equations 6.24, 6.25 stands for the closest estimate to the true parameter vector  $\mathbf{K}^*$ , that produces the true global minimum. To obtain comparable results between the estimated parameters the diagonal elements of the covariance matrix  $\text{cov}_{ij}(\hat{\mathbf{K}})$  were normalized with the respective parameter estimate. The normalized coefficient of variation for each parameter was calculated as,

$$CV_i = \sqrt{\frac{\sigma_{\hat{K}_i}^2}{\hat{K}_i^2}} \quad (6.26)$$

where  $\sigma_{\hat{K}_i}^2$  stands for the diagonal elements in this equation.

## 6.6. Results

Three rider models with increasing complexity are presented and discussed in this section. 1) A zero delay model which does not incorporate a predictor; the bicycles

states are direct inputs to the Pure Gain block (see Figure 6.6), 2) a model with sensory delays (see Table 6.1) in the sensory paths but without predictor, and 3) a model with delays and predictor. The performance characteristics of all models are assessed for three different configurations. In the first configuration the rider has the torque feedback loop connected (haptics on) and the plant dynamics approximate a normal bicycle. In the second configuration the internal torque feedback loop of the rider is disconnected (hence there are 5 instead of 6 feedback parameters) and the plant dynamics approximate a bicycle without steering torque feedback ( $T_\delta = 0$ ). This will show in how far a human control model *without steering torque feedback* can explain normal human behaviour. In the third configuration the steering dynamics change to that of steer-by-wire (haptics off). This means that the plant approximates a bicycle with decoupled roll-steer dynamics, hence the rider receives only steering torque feedback due to the inertia of the handlebars and not due to the front wheel dynamics. This will show in how far a human control model with *reduced steering torque feedback* information can explain normal human behaviour.

### 6.6.1. Zero delay (ZD)

The results of the zero delay model for all configurations and speed levels are presented in Table 6.2 (see Figure 6.9 for a comparison among all models and configurations for the lowest and highest measured speeds). A VAF of over 90% was observed for both the steer angle and heading, while for the roll angle the VAF is between 77-90% depending on speed and configuration. The CV indicates moderate dispersion for most gains and speed levels, except for the w/o  $T_\delta$  configuration where the uncertainty of  $K_\delta$  is much higher than the rest of the gains. For all speed levels  $VAF_\delta$  drops the most in the w/o  $T_\delta$  configuration. The steering angle and torque signals become substantially more oscillatory, although roll stabilization does not seem to be affected. In the haptics off case,  $VAF_\delta$  drops less than 3% and the degradation in the steering angle, torque and roll signals is small. All model predictions lag behind compared to the non-parametric responses. For the roll angle the predicted magnitude is two to three times smaller than the measured output.

### 6.6.2. With sensory delay (SD)

The results of the sensory delay model for all configurations and speed levels are presented in Table 6.3. Despite the fact that additional delays (Table 6.1) are introduced into the sensory paths, torque feedback information seems to be sufficient for prediction of the future states. However the model fit degraded by the introduction of sensory delays. The model with normal steering torque feedback provided a reasonable fit but  $VAF_\delta$  dropped, in particular for higher speeds (from 97.5% to 78% at  $5.7 \text{ ms}^{-1}$ ). The CV indicates moderate dispersion for most gains and speed levels, except for the steer angle gain  $K_\delta$ , where a higher dispersion was observed for the highest speeds. In contrast to the previous model a larger drop in the VAFs of all signals was observed between the first two configurations (with and w/o  $T_\delta$  feedback), and an equally significant drop between the last two. Aside

Table 6.2: Results of the zero delay model for the median rider for all configurations and speed levels. Haptic on/off differentiates based on the dynamics of the bicycle model, while "with or w/o  $T_\delta$  feedback" differentiates based on the structure of the rider control model. The values of the gains are presented together with their corresponding uncertainty level (CV). The VAF between the parametric and non-parametric signal outputs is also presented in percentage % to assess fitting performance. The derivative gains  $K_\phi$ ,  $K_\delta$  are measured in  $\text{kg m}^2 \text{s}^{-1}$ , the proportional gains  $K_\phi$ ,  $K_\delta$ ,  $K_\psi$  are measured in  $\text{kg m}^2 \text{s}^{-2}$  and the torque feedback gain  $K_{T_\delta}$  is dimensionless.

Speed	Bicycle Model Rider Model	Haptic On				Haptic Off	
		with $T_\delta$ feedback		w/o $T_\delta$ feedback		with $T_\delta$ feedback	
		Value	CV ( $10^{-4}$ )	Value	CV ( $10^{-4}$ )	Value	CV ( $10^{-4}$ )
$2.8 \text{ ms}^{-1}$	$K_\phi$	-77.17	114.86	-22.46	29.77	-115.36	213.52
	$K_\delta$	2.26	73.57	2.58	18.93	8.76	187.30
	$K_\phi$	-164.88	132.25	-24.50	73.14	-248.24	217.05
	$K_\delta$	32.75	150.14	3.76	140.96	29.67	215.07
	$K_\psi$	-63.22	133.29	-9.85	53.71	-93.44	223.02
	$K_{T_\delta}$	3.51	176.20	-	-	7.53	223.83
	$VAF_\phi$		77.80		82.79		78.37
	$VAF_\delta$		98.34		79.19		98.20
	$VAF_\psi$		93.46		93.51		93.74
	$3.6 \text{ ms}^{-1}$	$K_\phi$	-109.94	146.98	-21.30	35.99	-78.28
$K_\delta$		8.22	139.00	3.30	24.78	9.09	51.11
$K_\phi$		-248.47	147.39	-34.64	71.54	-229.14	84.40
$K_\delta$		50.78	147.72	6.48	130.57	53.16	92.96
$K_\psi$		-132.13	152.08	-17.74	61.92	-103.75	74.49
$K_{T_\delta}$		4.52	167.24	-	-	6.89	64.17
$VAF_\phi$			79.92		85.93		80.89
$VAF_\delta$			98.83		86.40		97.08
$VAF_\psi$			95.33		97.95		95.15
$4.7 \text{ ms}^{-1}$		$K_\phi$	-92.50	117.34	-27.29	46.40	-102.63
	$K_\delta$	4.81	183.05	4.25	41.56	11.24	28.38
	$K_\phi$	-183.03	135.64	-38.17	76.43	-249.74	74.10
	$K_\delta$	22.57	237.51	2.65	591.87	63.36	88.33
	$K_\psi$	-165.42	126.89	-33.78	63.74	-188.67	58.81
	$K_{T_\delta}$	3.42	174.23	-	-	8.98	13.88
	$VAF_\phi$		77.03		83.06		78.60
	$VAF_\delta$		97.57		80.27		95.57
	$VAF_\psi$		91.41		97.03		92.48
	$5.7 \text{ ms}^{-1}$	$K_\phi$	-83.90	117.61	-31.12	43.99	-76.30
$K_\delta$		5.83	142.87	5.58	40.62	10.91	30.23
$K_\phi$		-166.08	127.89	-43.64	67.14	-208.33	83.09
$K_\delta$		14.85	98.10	1.14	1836.39	79.44	75.47
$K_\psi$		-186.77	128.56	-49.82	52.31	-176.96	69.82
$K_{T_\delta}$		3.24	185.07	-	-	8.45	29.67
$VAF_\phi$			79.17		84.03		80.30
$VAF_\delta$			97.51		84.09		94.71
$VAF_\psi$			90.97		96.41		91.56

from that an additional delay in the predicted signals was evident (see Figure 6.9). The magnitude of the roll angle remains two to three times smaller than the actual non-parametric output.

### 6.6.3. Sensory delay reafferent optimal predictor (SDROP)

The results of the SDROP model for all configurations and speed levels are presented in Table 6.4. Despite the fact that significant delays are introduced into the sensory paths (Table 6.1) the internal model of the predictor compensates for all system latencies and achieves a good level of performance for all three configurations. A VAF of over 90% was observed for both the steer angle and heading, while for the roll angle VAF is between 80-86% depending on speed and configuration. The CV indicates a stable level of dispersion for most gains and speed levels. Only for the haptics on configurations a higher dispersion was observed for the steer rate  $K_{\delta}$  and steer angle gains  $K_{\delta}$ . A drop in  $VAF_{\delta}$  and an oscillatory behavior similar to the ZD model was observed in the w/o  $T_{\delta}$  and haptics off configuration. Also for this model the predicted roll angle magnitude remains two to three times smaller than the actual non-parametric output.

### 6.6.4. Testing and validation

The SDROP predictions capabilities are also tested without the Smith correction control loop, in this case the performance of only the adapted DOP is tested (see Figure 6.11 of Appendix I). To remove any potential effects related to the gains of the previous simulations the gain estimates of the ZD model are adopted for both SDROP and DOP simulations. A comparison between the true roll rate and predicted roll rate of the DOP and SDROP model without any internal model discrepancies is presented in Figure 6.10 (a). The state estimate of the SDROP model is closest to the true state, which is expected since the Smith loop corrects the error between the state estimates by comparing its predicted states with the direct outputs of the bicycle model. However, the main advantage of the Smith correction loop is the ability to correct for internal model imperfections, which come along with changes in the bicycle plant dynamics. To examine this ability the forward model of the SDROP is replaced with that of the haptics off configuration. This is based on the assumption that the rider has a reduced perception of bicycle dynamics when riding the steer-by-wire bicycle in the haptics off configuration. A comparison between the true roll rate and predicted roll rate of the DOP and SDROP with internal model imperfections is presented in Figure 6.10 (b). The SDROP manages to handle all model imperfections and achieve high level of performance, while the DOP predictions are oscillatory and lag behind compared to the true state estimates.

All results presented up to now, included feedback of steering angle and steering angle rate. To assess the importance of these loops, we also simulated the SDROP model omitting either or both feedback loops. Results in Table 6.7 demonstrated a poor fit for the highest speeds, in particular when removing both feedback loops. More specifically,  $VAF_{\delta}$ ,  $VAF_{\phi}$  dropped from approximately 90 to 60% and 80 to 26%, respectively.  $VAF_{\psi}$  dropped from 94 to 20%.

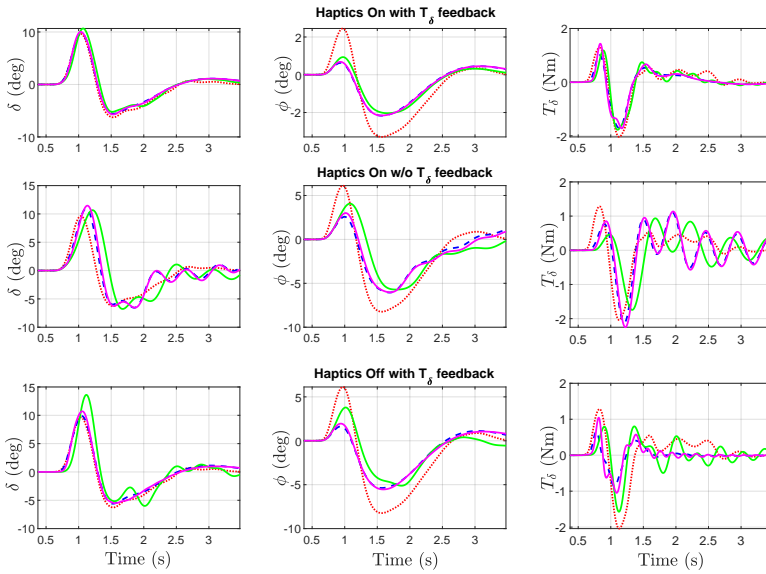
Table 6.3: Results of the with sensory delay model for the median rider for all configurations and speed levels. Haptic on/off differentiates based on the dynamics of the bicycle model, while "with or w/o  $T_\delta$  feedback" differentiates based on the structure of the rider control model. The values of the gains are presented together with their corresponding uncertainty level (CV). The variance accounted for (VAF) between the parametric and non-parametric signal outputs is also presented in percentage % to assess fitting performance. The derivative gains  $K_{\dot{\phi}}$ ,  $K_{\dot{\delta}}$  are measured in  $\text{kg m}^2 \text{s}^{-1}$ , the proportional gains  $K_\phi$ ,  $K_\delta$ ,  $K_\psi$  are measured in  $\text{kg m}^2 \text{s}^{-2}$  and the torque feedback gain  $K_{T_\delta}$  is dimensionless.

Speed	Bicycle Model Rider Model	Haptic On				Haptic Off	
		with $T_\delta$ feedback		w/o $T_\delta$ feedback		with $T_\delta$ feedback	
		Value	CV ( $10^{-4}$ )	Value	CV ( $10^{-4}$ )	Value	CV ( $10^{-4}$ )
$2.8 \text{ ms}^{-1}$	$K_{\dot{\phi}}$	-68.53	38.72	-14.93	37.52	-28.19	35.15
	$K_{\dot{\delta}}$	2.09	110.32	2.30	32.17	2.65	13.18
	$K_\phi$	-146.29	72.07	-16.98	92.51	-79.20	78.41
	$K_\delta$	22.18	95.38	4.62	103.75	10.51	93.36
	$K_\psi$	-40.34	56.18	-3.78	116.84	-14.53	67.08
	$K_{T_\delta}$	3.52	64.80	-	-	2.59	29.48
	$VAF_\phi$		81.15		69.61		80.01
	$VAF_\delta$		93.43		23.34		66.84
	$VAF_\psi$		93.78		69.67		83.30
$3.6 \text{ ms}^{-1}$	$K_{\dot{\phi}}$	-51.02	56.62	-15.40	55.90	-21.25	51.31
	$K_{\dot{\delta}}$	2.50	170.45	2.81	50.20	2.79	17.72
	$K_\phi$	-120.51	85.28	-22.82	102.83	-76.41	90.89
	$K_\delta$	16.58	153.27	3.94	243.76	17.14	84.92
	$K_\psi$	-43.06	79.41	-7.37	147.32	-13.30	103.52
	$K_{T_\delta}$	3.42	62.79	-	-	3.09	21.20
	$VAF_\phi$		82.85		79.48		73.14
	$VAF_\delta$		91.63		53.29		52.83
	$VAF_\psi$		95.10		84.88		71.58
$4.7 \text{ ms}^{-1}$	$K_{\dot{\phi}}$	-51.78	64.60	-19.26	349.70	-14.88	55.92
	$K_{\dot{\delta}}$	2.75	160.68	4.42	438.96	3.04	20.62
	$K_\phi$	-136.22	105.15	-27.02	111.78	-48.91	115.90
	$K_\delta$	3.21	1156.00	0.01	492609.67	16.01	99.26
	$K_\psi$	-64.43	87.60	-14.29	412.99	-10.82	119.48
	$K_{T_\delta}$	3.70	63.91	-	-	2.61	30.62
	$VAF_\phi$		77.86		71.14		63.73
	$VAF_\delta$		81.63		36.19		15.61
	$VAF_\psi$		90.32		80.57		55.71
$5.7 \text{ ms}^{-1}$	$K_{\dot{\phi}}$	-38.58	136.91	-19.65	110.85	-10.10	62.29
	$K_{\dot{\delta}}$	1.13	2085.75	5.42	128.32	3.08	21.38
	$K_\phi$	-120.59	120.57	-33.34	117.63	-30.95	133.76
	$K_\delta$	0.00	3969013.40	0.01	280859.33	18.46	79.69
	$K_\psi$	-60.65	95.03	-19.20	183.00	-8.17	131.56
	$K_{T_\delta}$	4.27	191.50	-	-	2.58	26.58
	$VAF_\phi$		73.65		70.08		49.58
	$VAF_\delta$		77.99		40.64		-
	$VAF_\psi$		84.32		79.50		39.90

Table 6.4: Results for the SDROP model for the median rider for all configurations and speed levels. Haptic on/off differentiates based on the dynamics of the bicycle model, while "with or w/o  $T_\delta$  feedback" differentiates based on the structure of the rider control model. The values of the gains are presented together with their corresponding uncertainty level (CV). The variance accounted for (VAF) between the parametric and non-parametric signal outputs is also presented in percentage % to assess fitting performance. The derivative gains  $K_\phi$ ,  $K_\delta$  are measured in  $\text{kg m}^2 \text{s}^{-1}$ , the proportional gains  $K_\phi$ ,  $K_\delta$ ,  $K_\psi$  are measured in  $\text{kg m}^2 \text{s}^{-2}$  and the torque feedback gain  $K_{T_\delta}$  is dimensionless.

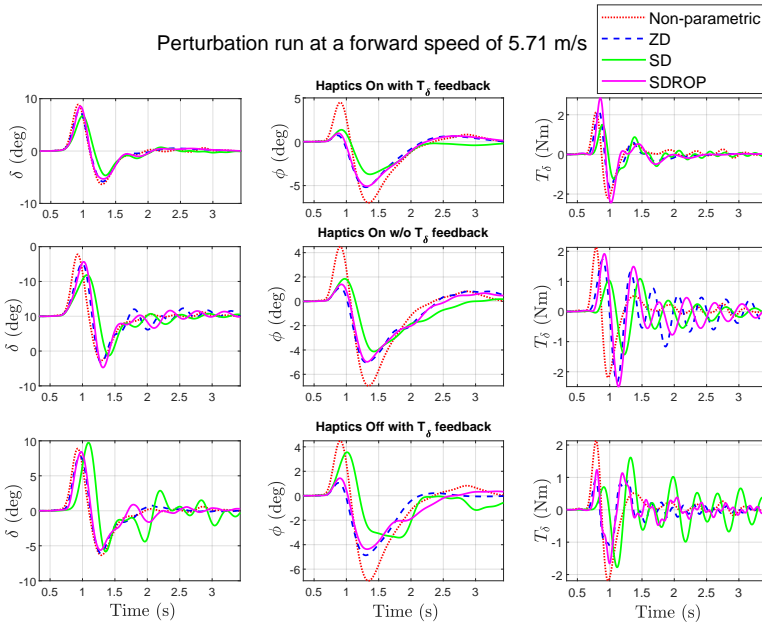
Speed	Bicycle Model		Haptics On		Haptics Off			
	Rider Model		with $T_\delta$ feedback	w/o $T_\delta$ feedback	with $T_\delta$ feedback			
			Value	CV ( $10^{-4}$ )	Value	CV ( $10^{-4}$ )	Value	CV ( $10^{-4}$ )
$2.8 \text{ ms}^{-1}$	$K_\phi$		-111.62	152.10	-22.44	28.45	-123.53	27.90
	$K_\delta$		1.80	234.11	2.62	14.59	8.62	35.62
	$K_\phi$		-248.74	151.15	-24.17	84.44	-239.60	18.65
	$K_\delta$		45.60	150.24	4.05	147.97	22.82	90.52
	$K_\psi$		-94.18	156.50	-9.03	65.63	-91.07	14.16
	$K_{T_\delta}$		4.66	170.99	-	-	7.93	27.78
	VAF $_\phi$		78.80		82.33		80.67	
	VAF $_\delta$		98.21		68.99		97.59	
	VAF $_\psi$		94.04		90.77		94.95	
$3.6 \text{ ms}^{-1}$	$K_\phi$		-94.83	125.80	-22.08	33.58	-97.15	115.92
	$K_\delta$		3.33	404.51	3.34	17.01	9.68	75.60
	$K_\phi$		-249.80	64.02	-37.61	80.02	-249.84	214.29
	$K_\delta$		58.12	63.15	7.44	140.22	50.23	247.35
	$K_\psi$		-125.36	97.89	-17.72	66.95	-119.20	160.68
	$K_{T_\delta}$		4.24	91.84	-	-	7.57	95.88
	VAF $_\phi$		81.66		86.50		83.35	
	VAF $_\delta$		97.33		79.27		96.15	
	VAF $_\psi$		96.13		96.97		96.80	
$4.7 \text{ ms}^{-1}$	$K_\phi$		-120.38	145.55	-27.59	56.00	-164.59	112.31
	$K_\delta$		0.24	4252.46	4.15	59.72	22.39	106.46
	$K_\phi$		-249.40	133.42	-37.98	90.28	-249.82	107.93
	$K_\delta$		29.49	210.73	2.67	665.03	14.70	649.60
	$K_\psi$		-222.31	143.06	-31.24	81.57	-209.12	111.47
	$K_{T_\delta}$		5.75	141.98	-	-	13.87	78.12
	VAF $_\phi$		79.21		81.88		80.97	
	VAF $_\delta$		97.07		70.43		90.44	
	VAF $_\psi$		92.97		95.43		95.93	
$5.7 \text{ ms}^{-1}$	$K_\phi$		-83.24	24.27	-27.53	46.08	-146.38	35.81
	$K_\delta$		0.65	1394.64	4.31	43.06	28.45	31.76
	$K_\phi$		-169.81	13.03	-44.71	92.82	-246.85	116.80
	$K_\delta$		8.29	278.33	4.13	493.77	29.42	401.88
	$K_\psi$		-185.36	6.72	-43.34	72.02	-211.40	56.88
	$K_{T_\delta}$		4.49	72.85	-	-	15.81	10.28
	VAF $_\phi$		82.35		85.06		80.57	
	VAF $_\delta$		96.12		75.40		87.27	
	VAF $_\psi$		93.83		97.03		93.59	

Perturbation run at a forward speed of 2.81 m/s



(a)

Perturbation run at a forward speed of 5.71 m/s



(b)

Figure 6.9: Steering angle  $\delta$ , roll angle  $\phi$  and steering torque  $T_\delta$  compared among the three rider models for all torque feedback configurations, for the lowest speed (top) and highest speed (bottom).

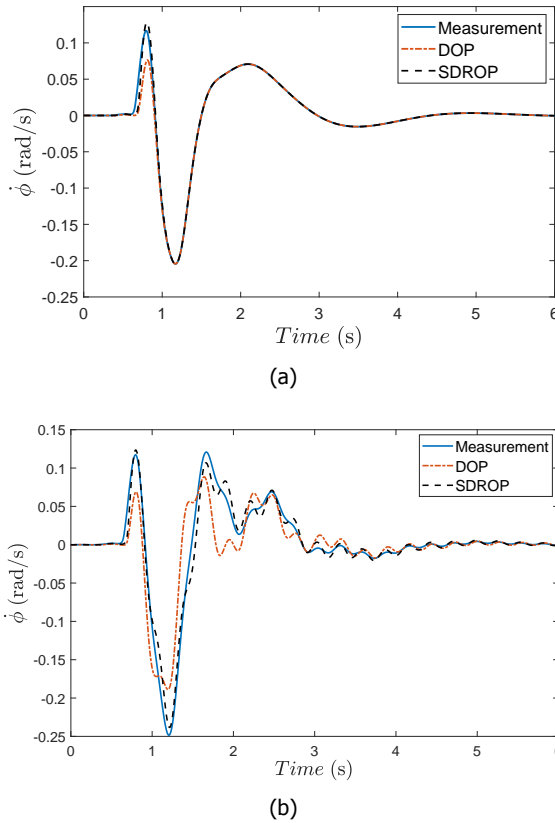


Figure 6.10: Comparison of true roll rate with simulated response of the DOP and SDROP predictors, (a) without internal model imperfections, (b) with internal model imperfections.

As a final step the simulated outputs of the SDROP model, which derive from the modelling dataset, are compared with the non-parametric responses of the validation dataset. The resulting VAFs are summarized in Table 6.5. Even though the perturbations in the validation set occurred at slightly lower speeds than the modelling dataset, most estimated VAFs are inline with those presented in the aforementioned tables. The median rider responses obtained from the two datasets lead to similar simulated responses and VAFs. To that end, all results described herein are justified indicating high quality of the identified rider models.

## 6.7. Discussion

We investigated rider control in steering and balancing using three control models varying presence of sensory delays (ZD vs SD) and prediction (SDROP), and varying presence of haptic steering torque feedback. In addition, for the SDROP model we assessed the importance of steering angle  $\delta$  and steering rate  $\dot{\delta}$  by omitting either

Table 6.5: Validation results of the SDROP model with  $T_\delta$  feedback, VAFs between the simulation output and the non-parametric response of the median rider of the validation dataset for all forward speed levels.

$v$ (ms <sup>-1</sup> )	$VAF_\phi$	$VAF_\delta$	$VAF_\psi$
2.5	69.86	90.39	91.73
3.7	72.40	80.02	96.18
4.4	70.51	95.32	87.78
5.6	73.76	85.28	91.18

or both feedback loops. Comprehensive analysis of the three control models indicated almost identical responses between the ZD and SDROP models. Differences between ZD and SDROP can be explained as follows. The predictor can accurately estimate effects of steering actions (efference copy) but only detects the effect of the external perturbation after the sensory delay. This explains the small time delay between 20-80 ms observed in the predictions of the SDROP model. The SD model responses were more strongly delayed compared to the actual measurements, with a delay between 20-120 ms, due to the sensory delays and missing prediction capabilities.

## 6

All models showed the best performance for the haptics on with  $T_\delta$  feedback configuration, with a VAF mostly over 90% for all speeds. For the ZD model the VAF predictions were closed with the predictions of the five state Jason Moore human controller [12] with no time delays or feedforward prediction. Although, in Jason's model steer torque was not included as feedback and predictions were evaluated against the lightly processed almost-raw data (250+ trials, hours of data) high VAFs predictions were obtained for both the treadmill and gymnasium data. For the SD model torque feedback was proven potent enough to compensate the added sensory delays but VAFs dropped in particular for higher speeds. For the haptics on w/o  $T_\delta$  feedback configuration a drop of at least 15% in the VAFs of all models was observed between the first two configurations (with and w/o  $T_\delta$  feedback), with a higher dispersion in the steer angle signals. Torque feedback improves fitting performance for all models and for this reason it is considered important for rider control. Different performance between the SD model and other two models is observed for the haptics off configuration. For the ZD and SDROP model  $VAF_\delta$  drops approximately 8% similar to the previous experiments conducted by Dialynas et al. [23]. Although for the SD model, a  $VAF_\delta$  drop of 70% and a much higher degradation in the fitting performance was observed compared to the other two models.

For the SDROP model omitting both steering angle  $\delta$  and steering rate  $\dot{\delta}$  had a negative effect in the fitting performance especially for the highest speeds. A large drop of about 70% was evident in the  $VAF_\psi$  and a drop of about 50%  $VAF_\phi$ . A drop of about 20% was also evident at the  $VAF_\delta$ . The higher degradation of the heading and roll VAFs indicates that handlebar position and velocity feedback (muscle spindles) enhances bicycle heading and roll perception at higher speeds.

For all models the predicted magnitudes of the roll angle remained two to three times smaller than the actual measured output (see Figure 6.9). Hence,  $VAF_\phi$  never reaches values higher than 85%. During the experiments the upper body remained unconstrained and acted as a double inverted pendulum with some torsional spring and damping properties. Additionally, simulations showed that rider compliance can influence the magnitude of the roll angle. A much higher roll angle of the bicycle is expected when the rider is more compliant (see Figure 6.12 of Appendix I for justification). Consequently, the degree to which the rider can extrapolate information from their vestibular system to make deductions on the state of the bicycle is debatable, since the vestibular system measures roll rate and acceleration of the head and not of the bicycle. Here it may be argued that proprioceptive (spindle) information can be used to relate head referenced perception (vestibular and visual) to bicycle motion. However, since this remains consistent among conditions the effectiveness of the torque feedback loop will remain analogous across conditions.

The gains for the rider controller roll  $K_\phi$ ,  $K_{\dot{\phi}}$  and heading  $K_\psi$  are consistently negative for all models, configurations and speeds. This is in full agreement with the basic bicycle balance mechanism: to steer into the undesired fall [3]. The balance of a bicycle is a so called non-minimal phase system. The heading gain  $K_\psi$  exhibits a consistent trend, its magnitude increases with speed. This means that at higher speeds the rider focus is shifted towards heading control.

## 6.8. Conclusion

In an effort to iterate over existing rider control models, the SDRP model has been created that successfully accounts for sensory delays by the use of an internal forward model. The performance of the SD model has proven that implementation of sensory delays without feedforward compensation does not produce results that match the experimental data. A prediction strategy has been developed that manages to circumvent the inability of the conventional Smith predictor to work on inherently unstable open loop systems. The rider model is able to control the bicycle at all speeds and follows the necessary stability condition of steer into the fall. All simulated responses match the non-parametric outputs obtained from both datasets with high level of performance, even when internal model inaccuracies are introduced.

With this rider model the importance of accurate determination of the various state variables via our sensors has been examined. The analysis showed that a highly realistic rider model must include steer angle, steer velocity and torque feedback to obtain adequate performance at all speed levels. Although, if the torque feedback loop is severed and not disconnected as in the haptics off configuration, state information might be deduced by the remaining inertial properties of the handlebar. This possibly explains why no differences were observed herein and also in the previous experiments conducted by Dialynas et al. [23]. Even though a steer-by-wire system decouples the roll-steer dynamics (haptics off) the remaining inertial

torque and position feedback of the handlebar is proven to be adequate for the rider to control and balance a bicycle. The absence of haptic feedback substantially changes the system dynamics where with haptics off the bicycle is always unstable (see Figure 6.5) but apparently riders can effectively stabilise and control the system. Future work can be directed towards a deeper understanding of the haptic feedback mechanism at the handlebars by varying the dynamic steer stiffness of the handlebars and applying handlebar steer torque perturbations.

## Appendix I

### Abbreviations

PID	proportional–integral–derivative.
ICM	internal control model.
IMU	inertial measurement unit.
IRF	impulse response function.
FIR	finite impulse response.
CV	covariance coefficient.
VAF	variance accounted for.
DOP	discrete optimal predictor.
ZD	zero delay.
SD	sensory delay.
SDROP	sensory delay reafferent optimal predictor.

### Mathematical notations

$F_s$	sampling frequency.
$\delta$	steering angle.
$\phi$	roll angle.
$\dot{\phi}$	roll rate.
$\theta$	fork angle.
$\dot{\theta}$	fork rate.
$\dot{\delta}$	steer rate.
$T_{PDH}, T_{PDF}$	handlebar and fork applied torques of PD controller.
$K_{PH}, K_{PF}$	proportional handlebar and fork gains.
$K_{DH}, K_{DF}$	derivative gains of the handlebar and fork.
$v$	forward speed.
$T_\phi, T_\delta$	roll and steer rider torques.
$\theta_R, \theta_F$	rotation angle of the rear and front wheel.
$\dot{\theta}_R, \dot{\theta}_F$	rotational angular rates of the rear and front wheel.
$y_P, y_Q$	rear and front wheel contact points.
$\psi$	heading (yaw) angle.

$l_g$	force moment arm coefficient measured from the ground.
$c_s$	denotes the force relationship between roll and steer angle.
$y^\delta(t), y^\phi(t), y^\psi(t), y^{T\delta}(t)$	non-parametric output states of steer, roll, heading angle and steer torque.
$\hat{y}^\delta, \hat{y}^\psi$	simulated disturbance output states.
$\bar{y}_k^\delta, \bar{y}_k^\psi, \bar{y}_k^{T\delta}$	absolute magnitude limits of steer, heading angle and steer torque.
$\tau$	time length of the impulse response function.
$h^\delta(\tau), h^\phi(\tau), h^\psi(\tau), h^{T\delta}(\tau)$	impulse response functions of steer, roll, heading angle and steer torque.
$w(t)$	external input force.
$K_\phi, K_\delta, K_\psi, K_\delta, K_\psi, K_{T\delta}$	steer, roll, heading angle and steer torque gains.

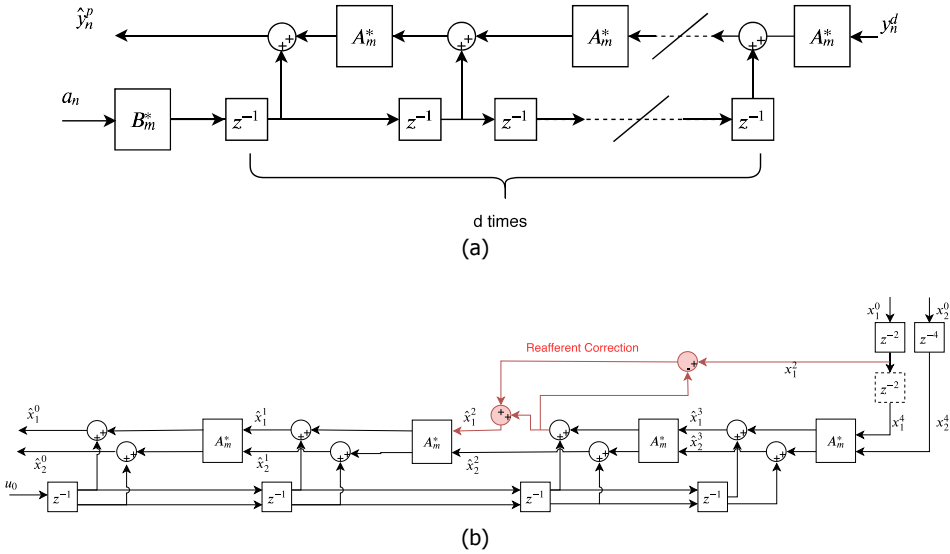


Figure 6.11: The discrete optimal predictor (DOP) control scheme, (a) conventional predictor with tapped delay line used to forward bicycle states in time for a predetermined delay  $z$ , where  $a_n$  represents the previous control input known as an "efference copy",  $y_n^d, y_n^p$  are the delayed and approximated state estimates, respectively. Matrices  $A_m^*$  and  $B_m^*$  are the best available discrete approximation of the system dynamics. (b) sensory delay refferent optimal predictor (SDROP) with tapped delay  $z$ , where  $u_0$  represents the previous control input "efference copy",  $x_1, x_2$  are the delayed input state estimates. Since  $x_1$  delay is smaller in magnitude than  $x_2$  an additional delay is added for synchronization of the states. The delayed state enters the tapped delay line until the point when the forward simulation produces an estimate of  $x_1$  that is concurrent with its measurement the refferent correction is performed and the process continues normally as for the conventional predictor.

Table 6.7: Effect of removing steering angle feedback for the SDROP model for the median rider for all speed levels for the haptics on configuration. Performance of the rider control model w/o  $\delta$  feedback, w/o  $\delta$  feedback and w/o  $\delta$  and  $\delta$  feedback. The values of the gains are presented together with their corresponding uncertainty level (CV). The variance accounted for (VAF) between the parametric and non-parametric signal outputs is also presented in percentage % to assess fitting performance. The derivative gains  $K_\phi$ ,  $K_\delta$  are measured in  $\text{kgm}^2 \text{s}^{-1}$ , the proportional gains  $K_\phi$ ,  $K_\delta$ ,  $K_\psi$  are measured in  $\text{kgm}^2 \text{s}^{-2}$  and the torque feedback gain  $K_{T_\delta}$  is dimensionless.

Speed	Bicycle model		Haptics On				
	Rider model	w/o $\delta$ feedback		w/o $\delta$ feedback		w/o $\delta$ and $\delta$ feedback	
		Value	CV · 10 <sup>4</sup> )	Value	CV · 10 <sup>4</sup>	Value	CV · 10 <sup>4</sup>
2.8 ms <sup>-1</sup>	$K_\phi$	-244.79	77.74	-94.37	66.88	-250	55.30
	$K_\delta$	9.33	64.92	-	-	-	-
	$K_\phi$	-241.28	88.57	-249.85	53.30	-250	102.55
	$K_\delta$	-	-	53.69	42.89	-	-
	$K_\psi$	-146.99	83.82	-88.83	60.95	-178.15	71.22
	$K_{T_\delta}$	6.38	85.61	4.82	66.41	5.99	65.72
	VAF $_\phi$	73.61		79.36		62.83	
	VAF $_\delta$	94.20		97.40		67.83	
	VAF $_\psi$	89.11		94.28		78.30	
	3.6 ms <sup>-1</sup>	$K_\phi$	-200.47	152.56	-76.35	128.90	-199.56
$K_\delta$		7.21	138.89	-	-	-	-
$K_\phi$		-249.87	164.90	-249.84	105.40	-230.98	87.22
$K_\delta$		-	-	67.47	92.39	-	-
$K_\psi$		-235.82	162.06	-115.48	124.48	-249.99	51.77
$K_{T_\delta}$		5.98	168.61	4.51	126.15	8.58	76.13
VAF $_\phi$		77.20		80.90		73.61	
VAF $_\delta$		96.27		97.13		90.01	
VAF $_\psi$		89.13		95.33		84.17	
4.7 ms <sup>-1</sup>		$K_\phi$	-120.38	96.66	-119.44	141.14	-249.73
	$K_\delta$	0.24	82.25	-	-	-	-
	$K_\phi$	-249.40	114.37	-249.98	129.63	-37.80	700.44
	$K_\delta$	29.49	-	30.59	108.31	-	-
	$K_\psi$	-222.31	111.07	-221.80	141.62	-23.44	616.86
	$K_{T_\delta}$	5.75	116.12	5.80	134.27	33.38	360.41
	VAF $_\phi$	80.19		79.21		27.33	
	VAF $_\delta$	96.08		97.07		61.85	
	VAF $_\psi$	94.34		92.96		21.19	
	5.7 ms <sup>-1</sup>	$K_\phi$	-142.58	74.83	-108.88	133.46	-215.38
$K_\delta$		3.96	375.50	-	-	-	-
$K_\phi$		-249.85	101.89	-227.62	122.66	-77.80	314.07
$K_\delta$		-	-	8.17	520.30	-	-
$K_\psi$		-239.04	89.12	-248.72	133.19	-42.70	440.01
$K_{T_\delta}$		5.06	102.05	6.08	129.43	40.79	14.25
VAF $_\phi$		80.27		81.13		26.99	
VAF $_\delta$		91.90		96.99		58.24	
VAF $_\psi$		93.35		92.74		19.51	

Table 6.8: Parameters of the steer-by-wire measurement bicycle from Figure 6.1 for the bicycle model of Figure 6.4.

Parameter	Symbol	Value
Wheel base	$w$	$1.03\ m$
Trail	$c$	$0.0665\ m$
Steer axis tilt	$\lambda$	$\pi\backslash 10$
Gravity	$g$	$9.81\ m/s^2$
Speed	$v$	<i>various m/s</i>
<u>Rear wheel R</u>		
Radius	$r_R$	$0.3429\ m$
Mass	$m_R$	$8.5\ kg$
Inertia	$(I_{Rxx}, I_{Ryy})$	$(0.095625, 0.19125)\ kgm^2$
<u>Rear Body and frame assembly B</u>		
Center of mass	$(x_B, z_B)$	$(0.4, -0.6)$
Mass	$m_B$	$95\ kg$
Inertia	$\begin{bmatrix} I_{Bxx} & 0 & I_{Bxz} \\ 0 & I_{Byy} & 0 \\ I_{Bxz} & 0 & I_{Bzz} \end{bmatrix}$	$\begin{bmatrix} 9.2 & 0 & 2.4 \\ 0 & 11 & 0 \\ 2.4 & 0 & 2.8 \end{bmatrix} kgm^2$
<u>Front Handlebar and fork assembly H</u>		
Center of mass	$(x_H, z_H)$	$(0.9, -0.66)$
Mass	$m_H$	$1.5\ kg$
Inertia	$\begin{bmatrix} I_{Hxx} & 0 & I_{Hxz} \\ 0 & I_{Hyy} & 0 \\ I_{Hxz} & 0 & I_{Hzz} \end{bmatrix}$	$\begin{bmatrix} 0.05892 & 0 & -0.00756 \\ 0 & 0.06 & 0 \\ -0.00756 & 0 & 0.00708 \end{bmatrix} kgm^2$
<u>Front wheel F</u>		
Radius	$r_F$	$0.6858\ m$
Mass	$m_F$	$1.84\ kg$
Inertia	$(I_{Fxx}, I_{Fyy})$	$(0.096, 0.195)\ kg\ m^2$
<u>Battery rack B</u>		
Center of mass	$(x_b, z_b)$	$(0.4, -0.55)$
Mass	$m_H$	$4\ kg$
Inertia	$\begin{bmatrix} I_{Hxx} & 0 & I_{Hxz} \\ 0 & I_{Hyy} & 0 \\ I_{Hxz} & 0 & I_{Hzz} \end{bmatrix}$	$\begin{bmatrix} 0.02 & 0 & -0.02 \\ 0 & 0.04 & 0 \\ -0.02 & 0 & 0.02 \end{bmatrix} kgm^2$

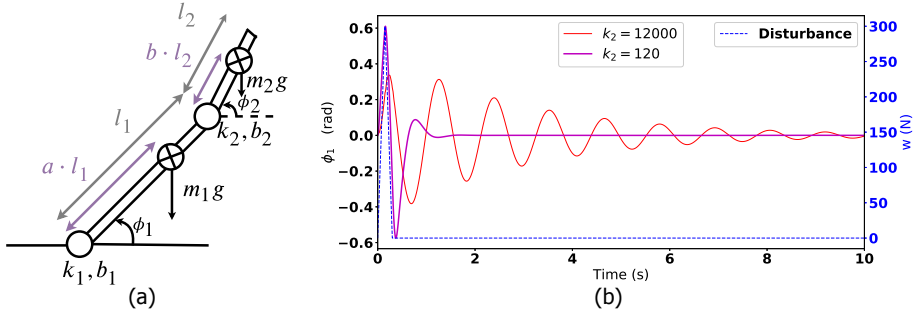


Figure 6.12: Double pendulum (a) with bicycle, rider mass equal  $m_1 = 20$ ,  $m_2 = 80$  kg and rod lengths equal  $l_1 = 0.8$  m,  $l_2 = 0.2$  m,  $a = 0.8$ ,  $b = 1$ , respectively. (b) Simulated roll angle  $\phi_1$  responses for two different stiffness and damping conditions  $k_1 = 3000$ ,  $k_2 = 12000$  kg m<sup>2</sup> s<sup>-2</sup> and  $b_1 = 50$ ,  $b_2 = 10$  kg m<sup>2</sup> s<sup>-1</sup>.

Table 6.9: Mass, damping and stiffness matrices for the bicycle model from Figure 6.4 according to the parameters from Table 6.8. Haptics on refers to the dynamics of a normal bicycle, whereas haptics off to that of a steer-by-wire bicycle.

6

Haptics on	
$\mathbf{M}_0 = \begin{bmatrix} 129.56096931 & 1.90339264 \\ 1.90339264 & 0.15330056 \end{bmatrix},$	$\mathbf{C}_1 = \begin{bmatrix} 0 & 37.68635697 \\ -0.540721349 & 1.00301681 \end{bmatrix}$
$\mathbf{K}_0 = \begin{bmatrix} -104.1937454 & -1.7093813 \\ -1.70938130 & -0.49976496 \end{bmatrix},$	$\mathbf{K}_2 = \begin{bmatrix} 0 & 97.75850654 \\ 0 & 1.72463528812 \end{bmatrix}$
Haptics off	
$\mathbf{M}_0 = \begin{bmatrix} 129.56096931 & 1.90339264 \\ 0 & 0.096 \end{bmatrix},$	$\mathbf{C}_1 = \begin{bmatrix} 0 & 37.68635697 \\ 0 & 0 \end{bmatrix}$
$\mathbf{K}_0 = \begin{bmatrix} -104.19374540 & -1.7093813 \\ 0 & 0 \end{bmatrix},$	$\mathbf{K}_2 = \begin{bmatrix} 0 & 97.758506542 \\ 0 & 0 \end{bmatrix}$

All the data used in this manuscript can be obtained by requesting from the corresponding author. The supplementary data related to this article are available online at <https://doi.org/10.5281/zenodo.3484032> (Dialynas et al., 2019).

## References

- [1] A. L. Schwab and J. P. Meijaard, *A review on bicycle dynamics and rider control*, *Vehicle System Dynamics* **51**, 1059 (2013).
- [2] J. P. Meijaard, J. M. Papadopoulos, A. Ruina, and A. L. Schwab, *Linearized dynamics equations for the balance and steer of a bicycle: a benchmark and review*, *Proceedings of the Royal society A: mathematical, physical and engineering sciences* **463**, 1955 (2007).
- [3] J. D. G. Kooijman, J. P. Meijaard, J. M. Papadopoulos, A. Ruina, and A. L. Schwab, *A bicycle can be self-stable without gyroscopic or caster effects*, *Science* **332**, 339 (2011).
- [4] D. T. McRuer and E. S. Krendel, *The human operator as a servo system element*, *Journal of the Franklin Institute* **267**, 381 (1959).
- [5] D. T. McRuer, D. Graham, and E. S. Krendel, *Manual control of single-loop systems: Part i*, *Journal of the Franklin Institute* **283**, 1 (1967).
- [6] A. Van Lunteren, H. Stassen, and M. S. H. Schlemper, *On the influence of drugs on the behavior of a bicycle rider*, in *Proceedings of the 6th Annual Conference on Manual Control, Wright Patterson AFB, OH, USA* (1970) pp. 7–9.
- [7] D. E. Massing, *A digital computer simulation of bicycle dynamics*, Tech. Rep. (Cornell Aeronautical Laboratory, 1971).
- [8] R. D. Roland, *Computer simulation of bicycle dynamics*, in *Proceedings of the ASME Symposium Mechanics and Sport* (1973) pp. 35–83.
- [9] D. H. Weir, *A manual control view of motorcycle handling*, Tech. Rep. (1973).
- [10] R. S. Sharp, *The stability and control of motorcycles*, *Journal of Mechanical Engineering Science* **13**, 316 (1971).
- [11] D. Eaton, *Man-machine dynamics in the stabilization of single-track vehicles*, Ph.D. thesis, University of Michigan (1975).
- [12] J. K. Moore, *Human control of a bicycle*, Ph.D. thesis, University of California Davis, Davis, CA, Aug. (2012).
- [13] R. Hess, J. K. Moore, and M. Hubbard, *Modeling the manually controlled bicycle*, *IEEE Transactions on Systems, Man, and Cybernetics-Part A: Systems and Humans* **42**, 545 (2012).
- [14] D. Soudbakhsh, Y. Zhang, and J. Yi, *Stability analysis of human rider's balance control of stationary bicycles*, in *2012 American Control Conference (ACC)* (IEEE, 2012) pp. 2755–2760.

- [15] T. D. Chu and C. K. Chen, *Modelling and model predictive control for a bicyclist-rider system*, *Vehicle System Dynamics* **56**, 128 (2018).
- [16] P. Wang, J. Yi, and T. Liu, *Stability and control of a rider-bicycle system: Analysis and experiments*, *IEEE Transactions on Automation Science and Engineering* (2019).
- [17] A. L. Schwab, P. D. L. de Lange, R. Happee, and J. K. Moore, *Rider control identification in bicycling using lateral force perturbation tests*, *Proceedings of the Institution of Mechanical Engineers Conference, Part K: Journal of Multi-body Dynamics* **227**, 390 (2013).
- [18] G. Dialynas, R. Happee, and A. L. Schwab, *Design and implementation of a steer-by-wire bicycle*, in *Proceedings of the 7th Annual International Cycling Safety Conference* (2018).
- [19] B. A. Francis and W. M. Wonham, *The internal model principle of control theory*, *Automatica* **12**, 457 (1976).
- [20] C. E. Garcia and M. Morari, *Internal model control. a unifying review and some new results*, *Industrial & Engineering Chemistry Process Design and Development* **21**, 308 (1982).
- [21] D. M. Wolpert, Z. Ghahramani, and M. I. Jordan, *An internal model for sensorimotor integration*, *Science* **269**, 1880 (1995).
- [22] R. B. Gillespie, A. H. Ghasemi, and J. Freudenberg, *Human motor control and the internal model principle*, *IFAC-PapersOnLine* **49**, 114 (2016).
- [23] G. Dialynas, C. Christoforidis, R. Happee, and A. L. Schwab, *The effect of haptic feedback in the balance task of bicycling*, in *8th International Cycling Safety Conference* (2019).
- [24] C. Christoforidis, A. C. Schouten, R. Happee, G. Dialynas, and A. L. Schwab, *Rider control identification in cycling taking into account steer torque feedback and sensorial delays*, *Master's thesis*, "under embargo", Delft University of Technology (2019).
- [25] E. Sanjurjo, M. A. Naya, J. Cuadrado, and A. L. Schwab, *Roll angle estimator based on angular rate measurements for bicycles*, *Vehicle System Dynamics* **57**, 1705 (2019).
- [26] S. C. Walpole, D. Prieto Merino, P. Edwards, J. Cleland, G. Stevens, and I. Roberts, *The weight of nations: an estimation of adult human biomass*, *BMC Public Health* **12**, 439 (2012).
- [27] P. Grasgruber, J. Cacek, T. Kalina, and M. Sebera, *The role of nutrition and genetics as key determinants of the positive height trend*, *Economics and Human Biology* **15**, 81 (2014).

- [28] J. K. Moore, M. Hubbard, J. D. G. Kooijman, and A. L. Schwab, *A method for estimating physical properties of a combined bicycle and rider*, in *ASME 2009 international design engineering technical conferences and computers and information in engineering conference* (American Society of Mechanical Engineers, 2009) pp. 2011–2020.
- [29] F. C. Van der Helm, A. C. Schouten, E. de Vlugt, and G. G. Brouwn, *Identification of intrinsic and reflexive components of human arm dynamics during postural control*, *Journal of Neuroscience Methods* **119**, 1 (2002).
- [30] E. De Vlugt, A. C. Schouten, and F. C. Van Der Helm, *Adaptation of reflexive feedback during arm posture to different environments*, *Biological Cybernetics* **87**, 10 (2002).
- [31] O. Kawakami, Y. Kaneoke, K. Maruyama, R. Kakigi, T. Okada, N. Sadato, and Y. Yonekura, *Visual detection of motion speed in humans: spatiotemporal analysis by fmri and meg*, *Human Brain Mapping* **16**, 104 (2002).
- [32] M. Barnett-Cowan, *Vestibular perception is slow: a review*, *Multisensory Research* **26**, 387 (2013).
- [33] E. De Vlugt, A. C. Schouten, and F. C. Van der Helm, *Closed-loop multivariable system identification for the characterization of the dynamic arm compliance using continuous force disturbances: a model study*, *Journal of Neuroscience Methods* **122**, 123 (2003).
- [34] R. Happee, E. De Vlugt, and A. C. Schouten, *Posture maintenance of the human upper extremity; identification of intrinsic and reflex based contributions*, *SAE International Journal of Passenger Cars-Mechanical Systems* **1**, 1125 (2008).
- [35] R. Miall, D. J. Weir, D. M. Wolpert, and J. Stein, *Is the cerebellum a smith predictor?* *Journal of Motor Behavior* **25**, 203 (1993).
- [36] O. Smith, *Closed control of loops with dead time*, *Chemical Engineering Progress* **53**, 217–219 (1957).

# 7

## Design and hardware selection for a bicycle simulator

Corresponding article: G. Dialynas, R. Happee, and A. L. Schwab: Design and hardware selection for a bicycle simulator, *Mech. Sci.*, **10**, 1-10, <https://doi.org/10.5194/ms-10-1-2019>, 2019.

### 7.1. Abstract

With the resurgence in bicycle ridership in the last decade and the continuous increase of electric bicycles in the streets a better understanding of bicycle rider behaviour is imperative to improve bicycle safety. Unfortunately, these studies are dangerous for the rider, given that the bicycle is a laterally unstable vehicle and most of the time in need for rider balance control. Moreover, the bicycle rider is very vulnerable and not easily protected against impact injuries. A bicycle simulator, on which the rider can balance and manoeuvre a bicycle within a simulated environment and interact with other simulated road users, would solve most of these issues. In this paper, we present a description of a recently build bicycle simulator at TU Delft, where mechanical and mechatronics aspects are discussed in detail.

### 7.2. Introduction

A number of recent studies have used recorded data of riders during naturalistic driving [1, 2]. However, behavioral studies for other vehicles often use simulators as they afford more reproducible experiments over a range of riders in a safe environment [3]. There have been a number of groups that have developed bicycle

simulators for a variety of research goals. Schwab and Requero [4] designed and built a haptic steering interface for the control input of a bicycle simulator, a potentiometer was used to estimate the angular position of the handlebar and not an angular encoder, whereas the output feedback torque magnitude of the selected motor was insufficient for this application. He et al. and Yin and Yin [5, 6] describe the design of a simulator mounted on a Stewart platform with steering and pedaling subsystems, which was used to study rider-bicycle models, but use steer angular position measurements to estimate angular accelerations and consequently the input torques via the product of angular accelerations and shaft inertia. However, the estimation of input torques from inertia and angular acceleration data contains dynamic errors [7]. Caro and Bernardi, Herpers et al., Plumert et al. [8–10] focus on rider behavior at a cognitive level and do not incorporate a realistic vehicle model.

At TU Delft we have designed and built a fixed-base bicycle simulator with haptic feedback at the handlebars, which can be used for various applications, for example studying rider behavior in various infrastructures, studying rider interaction in traffic and performing rider training. The bicycle simulator includes a haptic steering device which generates feedback driven by an underlying bicycle computer model, an incremental encoder to measure handlebar angle and a torque sensor to measure handlebar applied torque. In this paper we present a step by step guide to build such a bicycle simulator. First, the design requirements of the simulator interfaces are examined. Then, the design of the mechanical structure is described. Afterwards, the hardware components selection and calibration procedure is analyzed. The article ends with a discussion and conclusion section presenting other factors that make such a design valid for rider behaviour studies.

### 7.3. Design requirements of bicycle simulator interfaces

The aim of this section is to examine all the necessary requirements needed to build a realistic bicycle simulator. This is achieved by understanding the role of each sensory system on rider control. The primary sensory systems used during the riding process are, the vestibular sensory system, the visual sensory system and the proprioceptive sensory system [11]. Secondary sensory systems such as the tactile and the auditory sensory system also contribute to the perception of information during the riding process. For example, Mclane and Wierwille found that additional auditory information and tactile vibratory information improved the humans' estimation of speed [12]. In the first paragraph, of this section we describe the relation between the sensory systems and bicycle states. The second paragraph describes, the necessary requirements needed to be fulfilled in order to activate these sensory systems and build the simulator interfaces.

We presume that the bicycle rider system is a closed loop control system, balancing the mostly unstable bicycle and manoeuvring in the environment using feedback from the vestibular sensory system, the visual sensory system and the propriocep-

tive sensory system [11]. The rider uses bicycle roll angle  $\phi$  as part of the feedback control loops for the vestibular/visual sensory systems and handlebar steer angle  $\delta$  as part of the feedback control loop for the proprioceptive sensory system. The rider processes each state individually in order to apply a steer torque  $T_\delta$  to control the bicycle. A block diagram of the bicycle-rider system illustrating the relation between the primary sensory systems and bicycle states  $[\phi, \delta]$  the rider uses to control the bicycle by applying a steer torque  $T_\delta$  is presented in Figure 7.1.

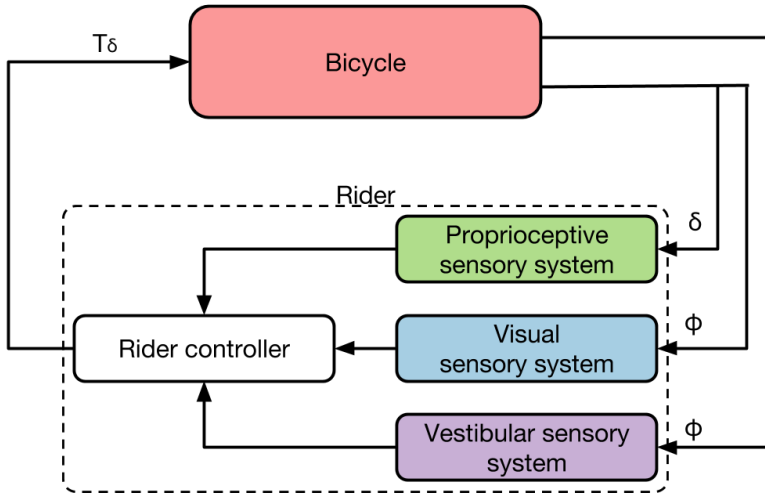


Figure 7.1: Block diagram of the bicycle-rider system illustrating the relation between the primary sensory systems and bicycle states  $[\phi, \delta]$  the rider uses to control the bicycle by applying a steer torque  $T_\delta$ .

Due to the aforementioned it is necessary to design and build user interfaces able to activate at least the primary sensory systems of the rider. To activate the visual sensory system a virtual environment is built using Unity® software. Projection of the virtual environment is achieved with a PC screen or with a head-mounted virtual reality display. To stimulate the proprioceptive sensory system a haptic steering device is designed and built. The steering device is able to generate torque feedback based on the equations of motion of a three-degree-of-freedom bicycle model, the so-called Carvallo-Whipple model [13]. The absence of a hexapod in the current implementation of the bike simulator does not allow the user to experience physical roll and thus, the vestibular sensory system remains inactive. Although, in naturalistic bicycle riding the rider uses both the vestibular and visual sensory systems to estimate roll angle. We think that visual roll of the horizon in the virtual environment might be an effective tool to compensate the vestibular loss. However, it should be noticed that the absence of vestibular input might have a negative effect on rider behavior in certain tasks, such as braking and lateral trajectory control. For this reason, the usage of such a simulator to study these tasks may be inappropriate [14]. The implementation of the equations of motions of the Carvallo-Whipple bicycle model used to drive the haptic steering device and Unity® environment will

be detailed in future publications.

## 7.4. Description of the mechanical structure

Several structural design considerations should be taken into account in case of building a bicycle simulator. Structural strength and required geometry are some of the most important aspects of the building process. The bicycle frame must be able to support the load of the rider during all operational conditions while having adjustable dimensions. Adjustable reach and stack dimensions are considered important mainly because it is suspected that body posture also influences the amount of applied torque. As stated in previous bicycle experiments conducted by Too [15] the interaction of muscle length with muscle lever moment arm length is one of the factors which will dictate the amount of force or torque that can be produced by the rider during cycling. It should be noted that this statement does not describe the relationship between muscle length, muscle activity, and torque of the brachialis muscles however, it shows the influence of body posture to applied torque. On the other hand, the bicycle frame must be able to support all the functional subsystems used in bicycles. For instance, the rear wheel and derailleur, the seatpost and seat, the bottom bracket and pedal subsystem etc. In addition to the above, the simulator must be able to simulate the steering forces acting at the bicycle during the riding process. In the first section of this chapter we describe the design and building process of the main structure of the bicycle frame, next we present the design of the haptic steering device and overload protection mechanism.

The mechanical portion of the simulator consists of three main structural parts. A bicycle roller training base (600x400 mm), a square tube (40x40x1000 mm) used as a steering column, and a rear half of a step-through bicycle frame (54 cm), see Figure 7.2. To mount all the structural parts together the following modification are made. The front roller of the base is removed and a rectangular tube (40x20x500 mm) is welded as a replacement. In addition, six metal foot pegs (40x20x500 mm) two at the front, middle and rear are also mounted. The foot pegs are mainly used to increase the vertical distance of the base in respect to ground and also to distribute the load equally to specific areas of the frame. At the steering column a (25x500 mm) tube is welded at a 25° angle and at a 40 mm distance from the end of the square tube. At the bicycle frame the headtube is removed two custom made clamps (AL7075) are mounted to the upper and lower tubes respectively. The upper and lower clamps are connected with two metal straps one per each side. The combination of the upper frame clamp design together with the (25x500 mm) welded tube of the steering column create the first prismatic joint of the assembly. As it can be seen in Figure 7.3 point (1) this prismatic joint is used to mount the steering column to the bicycle frame. Steer and saddle height can be adjusted over a large range, and the steering assembly can be moved horizontally to accommodate a large range of body sizes and bike geometries.

To mount the steering column and bicycle frame to the roller base a combination of different types of adjustable blocks are used (blocks are provided from RK Rose Krieger). A hinge clamp block and a t-shape block (Gwv 40). First, the hinge clamp

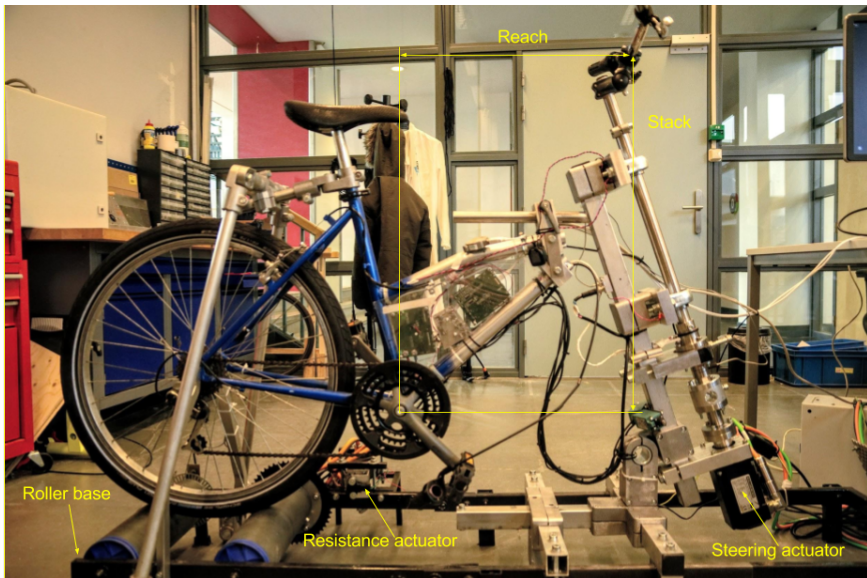


Figure 7.2: TU Delft fixed base bicycle simulator.

block is mounted to the column and tilted to create a bicycle headtube angle of  $72^\circ$ , since this is a common angle also adopted in the Carvallo-Whipple bicycle model [13]. Afterwards, the hinge block is mounted to the t-shape block which is next mounted to the racks of the base with two addition square tubes (40x40x380 mm) and two custom made c-shape clamps. Because the upper joint of the column is prismatic a second prismatic joint is also constructed at the base level. To construct the second joint an additional t-shape block is mounted to the base oppose to the first one. A square tube (40x40 mm) is mounted to the first clamp and sliding freely through the square hole of the second one as can be seen at Figure 7.3 point (2). These two prismatic joints together with the c shape clamps are used to adjust the reach dimensions of the bicycle frame. The mounting of the bicycle frame from the front end is now completed. To mount the bicycle frame from the rear end to the base two mechanical arms and a trapezoidal shape structure are combined. The mechanical arms are constructed from L-shape stripes and are used to mount the bike from the rear wheel axis to the base. The trapezoidal structure is constructed from aluminium tubes and a combination of hinge clamps (Gp 25, Kvr 25, W 25). This structure is used to mount the bicycle frame from the seatpost to the base as can be seen in Figure 7.3 point (3).

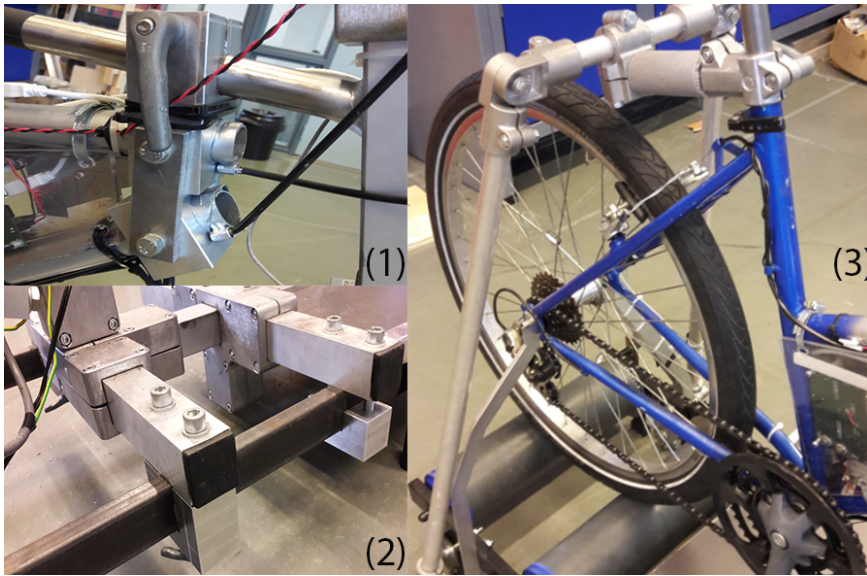


Figure 7.3: Connection of the bicycle frame to the roller base using prismatic joints (1), (2) and mechanical arms (3).

#### 7.4.1. Description of haptic steering device

To allow the rider to interact with a virtual environment and receive realistic handlebar torque feedback from the simulation model a haptic steering device is required. The device must be able to generate realistic torque feedback in order to enhance rider control and prevent excessive rotation of the handlebars. The importance of haptic steering feedback on rider control is stated in previous bicycle experiments conducted by Lee et al. [16]. In this subsection we describe the components used to build such a device.

The haptic steering device consists of two sub-assemblies. The steering shaft assembly and the column mount assembly. The steering shaft assembly includes the components used to build the steering shaft, whereas the steering column assembly includes the components used to mount the steering shaft to the column. The steering shaft assembly consists mainly of eight components (not including the handlebar assembly and adaptors). Five of these components are mechanical and three of them are electromechanical. More specific, an overload protection mechanism is used for safety, a steer range limiter is used to restrict the rotational range to  $\pm 35^\circ$ , a shaft is used to intersect with the actuators of the limit switches (limit switches are shown in Figure 7.5) and turn of the electric motor when the maximum rotational range is reached. Two pillow block bearings are used to mount the telescopic shaft to the column. An electric motor is used to generate steering feedback, an incremental encoder is used to measure the steering angle and a torque sensor is used to measure the applied handlebar torque. The steer shaft assembly is mounted to the column with 3 additional custom made clamps, the electric motor

clamp and two bearing clamps. An extra clamp is used to mount the reading head of the encoder. Material used for the shaft components is AL7075 excluding the telescopic shaft which is made from Steel 304. In Figure 7.4 the steering shaft and column assembly is presented.

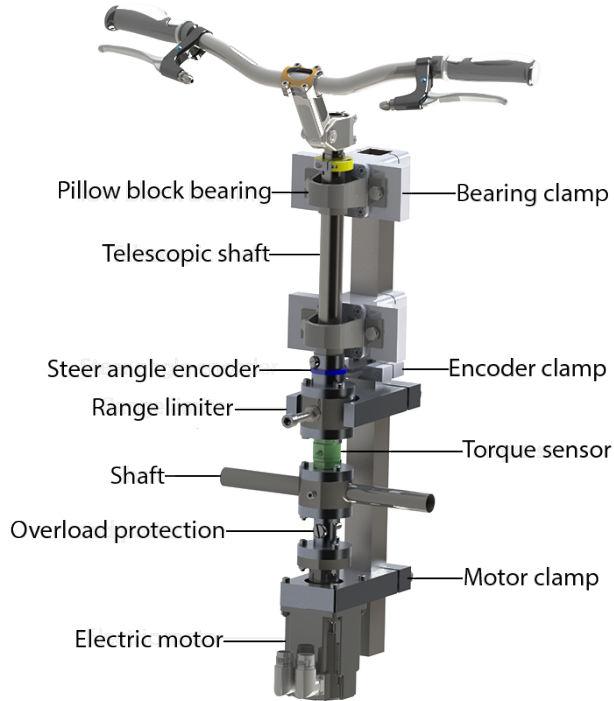


Figure 7.4: Steering column and shaft assembly exported from Solidworks 2016.

#### 7.4.2. Description of overload protection mechanism

Different methods can be used to protect a rotating shaft from torsional stress. On a software level torque and rotational range limits can be set in the parameter programming of the motor drive. However, in case of a sensor malfunction the software might be unable to recognize the torsional overload condition. For this reason, a mechanical solution is recommended as a second measure of protection. There are typically two mechanical mechanisms used to protect a rotation shaft, a torque limiter and a shear pin. From the above two mechanisms the usage of a torque limiter is not recommended for this application mainly because there is no clear indication of the operational speed the rated torques are measured at, as first noticed by Jason Moore [17]. Most of the available torque limiters list the rated torques but with no indication of the operating speed the torques are measured at.

It turns out they are with respect to an 1800 rpm operating speed. The absence of this vital information together with the low steer rates make the selection of a limiter inappropriate, since it might lead to further adjustments and modifications to make the limiter operate properly. For this reason, a custom shear pin mechanism is designed and mounted inline with the steering shaft. The shear pin mechanism functions are to protect the steering shaft and the user by mechanically disengaging the feedback motor from the handlebars when the maximum torsional strength is reached. For the geometric design of the shaft-hub mechanism and selection of the proper pin size the following equations are used. For the shaft-hub combination the desired geometric relationship between the two diameters is  $D_1 = 1.5D$ , where  $D_1$  is the hub, and  $D$  the shaft diameter, respectively. The diameter of the shear pin  $d$ , is calculated based on the shear strength  $\tau$ , of the material, the service factor  $\kappa$ , the maximum breaking torque  $T$ , and the hub diameter  $D$ , as seen in Equation 7.1 conforming to the requirements of ISO 8730-40 standards.

$$\tau = \kappa \frac{4T}{\pi d^2 D} \quad (7.1)$$

The shear strength of the selected pin is also tested in practice. The pin shears between 25-26 Nm which is 30% lower from the steering shaft overload condition. The selected shear limit is considered adequate according to the aforementioned ISO standards.

## 7.5. Sensor and motor selection

There are three sensors and one actuator motor in the existing bicycle simulator. Two of the three sensors are located at the steering assembly. More specifically, an angular encoder, a torque sensor and an electric motor are mounted inline with the steering shaft, see Figure 7.5, whereas a gearwheel encoder is mounted at the rear roller of the powertrain assembly as seen at Figure 7.6.

To select the proper motor and sensors a number of technical specifications need to be determined in advance. For the encoders, the type and resolution, for the torque sensor, the range and resolution, and for the electric motor the maximum and continuous torque. In this section we describe the procedure followed to determine these requirements. In the first two paragraphs, the encoders and torque sensor requirements are determined, whereas in the last paragraph the electric motor requirements.

Two types of encoders are found in literature, incremental and absolute. Incremental rotary encoders output the pulse corresponding to the rotation angle only while rotating, and the counting measurement method that adds up the pulse from the measurement beginning point. On the other hand, absolute rotary encoders output the signal of position corresponding to the rotation angle by coded elements. The incremental encoder does not output an absolute position and for this reason typically the internal structure is simpler and the cost lower. For both the steer angle and wheel speed measurements incremental encoders are selected. The resolution

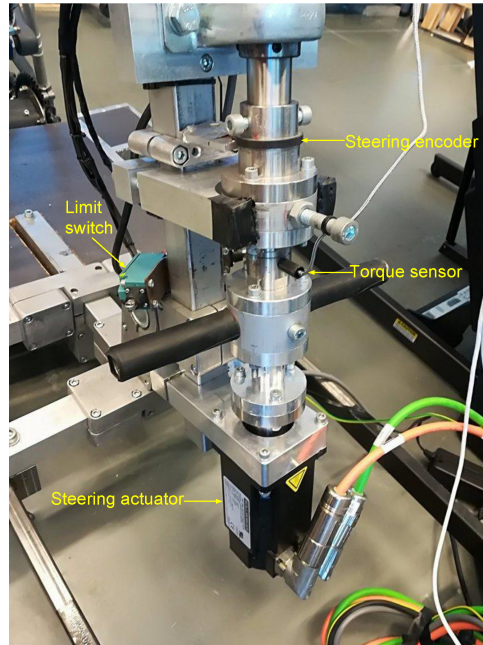


Figure 7.5: Steering shaft assembly.

## 7

of the steer encoder in counts per turn (cpt), is determined based on the smallest steer angle increment  $\Delta\delta$ , as seen at equation below [18]:

$$N = \frac{360^\circ}{4\Delta\delta} \quad (7.2)$$

A steer encoder with 152,000 (cpt), and an additional index channel for accurate homing was selected (RLM2HDA001). For the wheel speed encoder the resolution is selected based on the resolution range of encoders used for similar systems, such as the anti-lock braking systems of motorcycles. A gearwheel encoder with 192 (cpt), is selected (reading head is from rls type is GTS35, gearwheel from KTM). The gearwheel and reading head are mounted directly to the rear roller and base respectively as seen at Figure 7.6.

For the selection of the torque sensor the steer torque profile must be determined, not only for normal bicycle riding but also during perturbation tests. Measuring the steer torque profile can be achieved with modern torque sensors although the problem of crosstalk disturbance must be taken into account. Crosstalk occurs due to the large forces and moments applied to the fork and handlebars by the ground and the rider during bicycling. These forces and moments corrupt the relatively small torque measurements as they can be hundreds of times larger in magnitude. Few published studies attempt to estimate or directly measure steer torque. De



Figure 7.6: Gearwheel sensor mounted at base roller.

Lorenzo and Hull [19] instrumented a bicycle which could measure pedal, handlebar, and hub forces to characterize the in-plane structural loads during downhill mountain biking. The handlebar forces acting forward and parallel to the ground were used to estimate the steering torque. A maximum torque of about 7 Nm is shown in this study although crosstalk disturbance was not taken into account. Jackson and Dragovan [20] attempted to estimate the torques acting on the front frame based on orientation, rate and acceleration data taken while riding a bicycle with no-hands. They estimated a steer torque under  $\pm 2.5$  Nm. Cheng et al. [21] attached a torque wrench to a bicycle and made left and right turns at speeds from 0-13 m/s. The torques were found to be under 5 Nm except for the 13 m/s trial which read about 20 Nm. However, the torque wrench calibration range (0-84 Nm) was too large for the obtained torque measurements reducing the accuracy of his results. Iunchi and Murakami [22] attached a steer motor and controller to the handlebars and tried to estimate steer torque from the motor current and handlebar moment of inertia. They are one of the few studies that takes into account some of the inertial effects of the handlebar. Cain and Perkins [23] designed and fitted a custom torque sensor in the bicycle steer tube. They tried to remove crosstalk effects by applying an axial load on the sensor but they did not account for the dynamic inertial affects of the components above and below the sensor. Their measured steer torques during cornering were under  $\pm 2.4$  Nm. From the above mention studies, none succeed to measure the actual applied rider torque since very few accounted crosstalk disturbance and even fewer the dynamic inertial effects of the components above or below the sensor. Jason Moore [17] was the first who developed an experimental bicycle that can accurately extract rider applied torque. In his design a torque sensor (Futek 150, TFF350,  $\pm 15$  Nm) is mounted inline with the handlebar and fork using a double universal joint isolating the handlebar and fork loads during bicycling. The instrumented bicycle he developed was used to measure steer torque responses during lateral force perturbation experiments

[11]. A rider torque range between 0-10 Nm, is realized in these experiments. For that reason, a torque sensor with a range of  $\pm 25$  Nm, and a resolution of 4  $\mu$ Nm, is selected (Kistler 9349A).

For the selection of the haptic steer feedback motor the Carvallo-Whipple bicycle model developed by Meijaard et al. [13] is used to predict the maximum torque required within the stable and unstable speed. To obtain an estimation of the feedback motor torque a steer torque impulse of 5 Nm is given as an input to the model. The selected input torque is based on previous bicycle experiments conducted from [17] and is considered the maximum steering torque measured for controlling a bicycle in normal manoeuvres. To calculate the output feedback torque the steer angular acceleration  $\delta$ , and the moment of inertia  $I$ , of the steer axis of the bicycle simulator is used, see Equation 7.3. The steer angular acceleration  $\delta$ , is given as an output of the Carvallo-Whipple bicycle model, whereas the steer shaft moment of inertia  $I$ , of the bicycle simulator is measured experimentally.

$$T = I\ddot{\delta}(t) \quad (7.3)$$

As shown in Figure 7.7 a maximum torque of almost 5,4 Nm is noticed at the unstable speed region, whereas at the stable speed region a torque of maximum 0,02 Nm is found. Combining a reduction gearhead with an electric motor to reduce its physical size and increase torque output is not optimal for the existing design. Backlash of the gearhead can distort torque sensor measurements and for this reason is excluded from the existing steering design. For this reason, an electric motor of 1410 W and drive combination able to deliver a stall torque of approximately 4 Nm, and a max.torque 11.5 Nm are selected for the steering actuation (Kollmorgen AKM42G and AKDP00606).

## 7.6. Calibration and testing of hardware components

To ensure that the selected components fulfill their specifications every component is tested and calibrated. It is important that all of the sensors and actuator behave in a consistent and predictable manner. For example, motor performance before and after tuning is compared not only with its own feedback but also with the torque sensor output. This way performance mismatch is analyzed in an early development stage and is avoided by either re-calibrating specific sensors or by re-tuning the motor drive control parameters.

To calibrate the torque sensor a table wrench, a digital torque wrench, an amplifier (Kistler 5030A2) and an oscilloscope are used. The torque sensor is mounted from one end to a table wrench and from the other end to a digital torque wrench. Next, the torque sensor is connected to an amplifier and an oscilloscope. For different torque magnitudes and amplification ranges the voltage output is measured. Amplification range 1 can measure torque magnitudes up to  $\pm 25$  Nm, whereas range

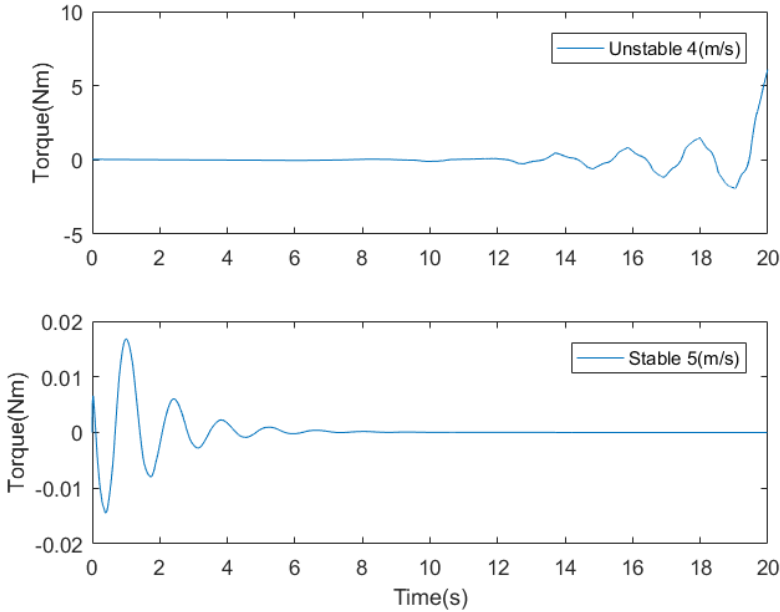


Figure 7.7: Estimated haptic steer feedback torque based on angular acceleration output  $\ddot{\delta}$ , of the benchmark bicycle model for a steer torque input of 5 Nm.

2 only up to  $\pm 2.5$  Nm. Expected rider torque is assumed within 0-10 Nm range and thus amplifier range 1 is selected as a configuration for the bicycle simulator.

An analog signal is used to supply a reference command torque to the haptic feedback motor. There are three command modes that the motor drive can be set with the analog mode, position control, velocity control and torque control. Position and velocity control are typically used when precise tasks are required, for instance a welding task. On the other hand, torque control is used when compliant control is needed. Compliant here means that the rider is able to rotate the shaft at any angle required while receiving torque feedback from the motor. Since compliance is required the operation mode is set to analog torque mode.

The analog torque control loop of the motor drive unit can be seen at Figure 7.8, where ( $V_r$ ) is the reference voltage, ( $i_r$ ) is the current reference, ( $i_c$ ) is the output current of the motor controller and ( $i_f$ ) the feedback current of the electric motor. To convert the input reference voltage ( $V_r$ ) to an input current reference ( $i_r$ ) a scaling constant must be set in  $\text{Amp V}^{-1}$ . This scaling constant is set based on the peak current of the drive and the maximum voltage range of the controller. For a peak motor current of 18Amps and a maximum input voltage of 12 V the constant is set to  $1.5 \text{ Amps V}^{-1}$ .

After the current scaling constant is set, the torque constant is determined by mea-

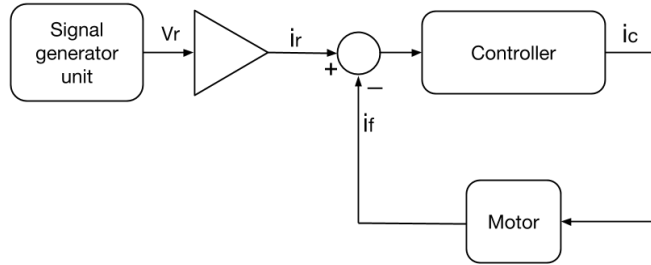


Figure 7.8: Block diagram of motor and motor drive configuration.

asuring the motor response for a given input command. For an input voltage command of 1,06 ( $V_r$ ), which corresponds to a current of 1.6 ( $i_r$ ) a torque of 1.75 Nm is produced as an output from the motor, see Figure 7.9. A linear torque/current relationship of  $1.09 \text{ Nm Amp}^{-1}$  is set in the software for controlling the motor in torque mode. A maximum motor torque output of 10.92 Nm can be reached for this specific motor-drive configuration.

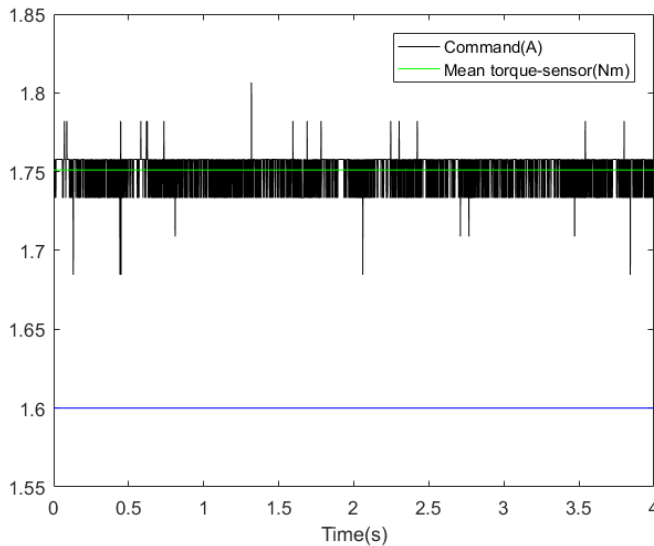


Figure 7.9: Ampere/torque analogy.

Once the motor is connected to the steering shaft the system is tested for given control tasks. A sinusoidal input signal with a frequency of 2 Hz and an amplitude of 1,6 Amp equivalent to 1.75 Nm is given as an input to capture the response of the system. The performance of the motor is tested before and after tuning. The methodology used to estimate the shaft inertia and tune the motor drive is described

at next subsection. As it can be seen at Figure 7.10 the torque commanded to the motor matches to the output feedback torque when the motor is tuned. On the other hand, overshooting and phase shift occurs when the motor is not properly tuned.

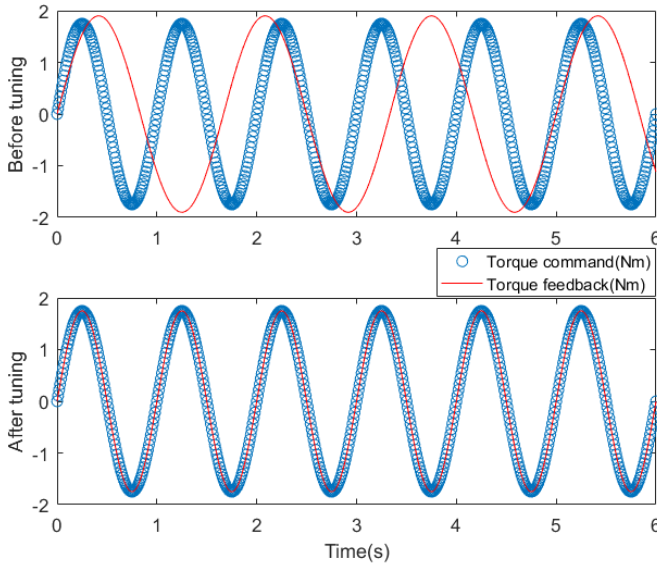


Figure 7.10: Motor performance before and after tuning.

### 7.6.1. Estimation of steering shaft moment of inertia

The damping and inertia properties of the steering shaft must be estimated in case the torque that the rider applies is estimated from acceleration data and also in case position and velocity modes are used to control the motor and auto tuning can not be used for safety reasons. To estimate the moment of inertia different methods can be used. A first approach could be to extract the moment of inertia from the CAD model. A second approach could be to use system identification. A third approach could be to add two springs and calculate the moment of inertia from the oscillation period and the equation of motion of the system. The first method can not be used for the existing CAD model. In the CAD model of the steering shaft there are parts exported from suppliers which are represented as solid entities and are not modeled correctly. The assembly parts of these entities could not be separated and the moment of inertia of these components can not be calculated separately. For instance, the motor shaft moment of inertia can not be measured as a separate body of the motor. On the other hand, system identification can be used to estimate the moment of inertia of the steering shaft, however a more straightforward approach is the spring method. For the above reasons, the last approach is used to estimate the moment of inertia of the steering shaft. To

oscillate the steering shaft two extension springs with a rate of  $k = 317 \text{ N/m}$  and a length of  $0.05 \text{ m}$  are added perpendicular to the handlebars as shown in Figure 7.11.

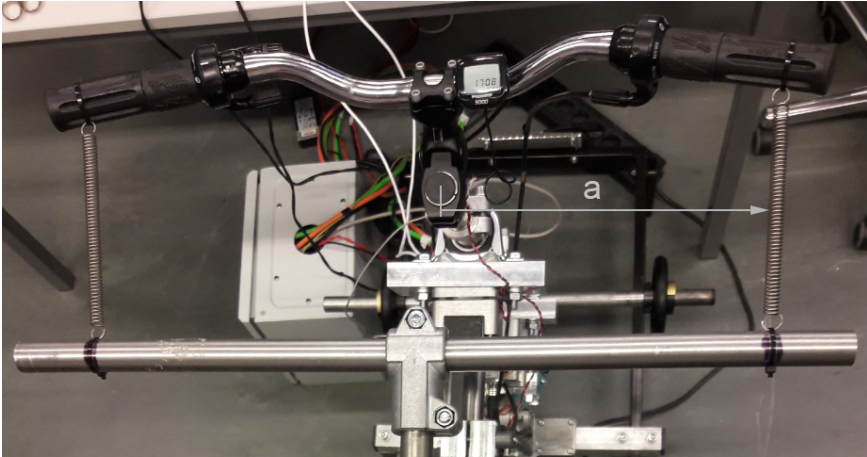


Figure 7.11: Experimental set-up to measure moment of inertia.

The springs are pretensioned proportionally and set to idle around  $0^\circ$ . The springs are excited and the oscillation period is measured through the steering encoder. The oscillatory motion of the shaft can be seen in Figure 7.12. The equation of motion of the steering shaft after attaching the springs is:

$$I\ddot{\delta}(t) + b\dot{\delta}(t) + 2ka^2\delta(t) = 0 \quad (7.4)$$

The steering shaft equation of motion consists of the inertia  $I$ , viscous friction  $b$ , and spring stiffness  $k$ , and moment arm  $a$ .  $\delta$  denotes the desired angle of the system,  $\dot{\delta}$  and  $\ddot{\delta}$  the desired angular velocity and acceleration respectively. Friction caused between bearings and electric motor components is neglected, thus  $b$  is considered zero. Thus the mass moment of inertia equals:

$$I = \frac{2ka^2}{\omega^2} \quad (7.5)$$

The mass moments of inertia of the steering shaft assembly using the spring method and auto-tuner of the motor drive are  $I=0,0828 \text{ kgm}^2$  and  $I=0,0912 \text{ kgm}^2$  respectively. The comparison of the two methods is used to validate the spring method. The inertia difference between the two methods might be due to the fact that viscous friction  $b$ , is neglected in the spring method, whereas this is not the case when auto-tuning is used.

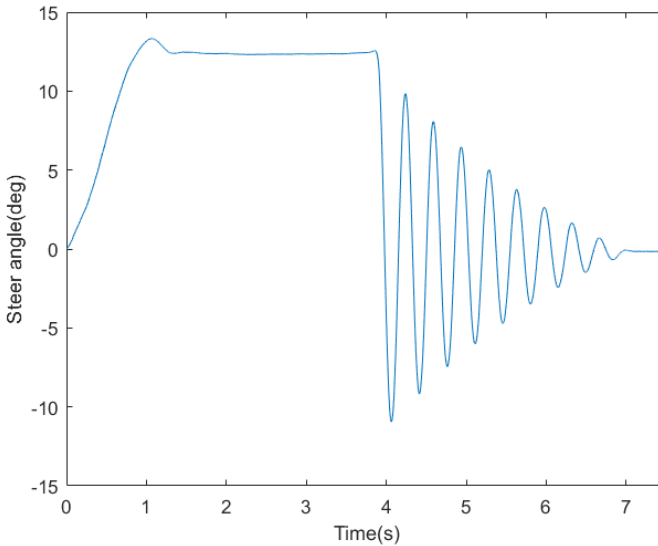


Figure 7.12: Oscillation of steering shaft using spring method.

## 7.7. Conclusions

The objective of this study was to realize all the necessary steps needed to design and build a realistic bicycle simulator. The simulator prototype is the result of multiple design choices and constraints. Constraints, primarily time-wise, have resulted in a system wherein a mountain bike is placed on top of rollers and later fitted with a haptic steering device. There is still space for improvement regarding the mechanical structure and haptic steering device. For example, the prismatic joints of the mechanical structure can be equipped with linear bearings to allow friction-less motion when adjusting the stack and reach dimensions. The steering shaft assembly can be machined as a single part and from a light material in order to reduce both inertia weight and misalignment.

All the data used in this manuscript can be obtained by requesting from the corresponding author. The supplementary data related to this article are available online at <https://doi.org/10.5281/zenodo.2525685> (Dialynas et al., 2018).

## References

- [1] N. Kovascova, J. C. F. D. Winter, A. L. Schwab, M. Christoph, D. A. M. Twisk, and M. P. Hagenzieker, *Riding performance on a conventional bicycle and a pedelec in low speed exercises : Objective and subjective evaluation of middle-aged and older persons*, *Transportation Research Part F: Traffic Psychology and Behaviour* **42**, 28 (2016).
- [2] J. K. Moore, J. G. Kooijman, A. L. Schwab, and M. Hubbard, *Rider motion identification during normal bicycling by means of principal component analysis*, *Multibody System Dynamics* **25**, 225 (2011).
- [3] J. Steen, H. Damveld, R. Happee, M. Van Paassen, and M. Mulder, *A review of visual driver models for system identification purposes*, in *Proceedings of IEEE Systems Man and Cybernetics Conference* (2011) pp. 2093–2100.
- [4] A. L. Schwab and A. M. Recuero, *Design and experimental validation of a haptic steering interface for the control input of a bicycle simulator*, in *Proceedings of ECCOMAS Multibody Dynamics Conference* (2013) pp. 1–4.
- [5] Q. He, X. Fan, and D. Ma, *Full bicycle dynamic model for interactive bicycle simulator*, *Computing and Information Science in Engineering* **5**, 373 (2005).
- [6] S. Yin and Y. Yin, *Study on virtual force sensing and force display device for the interactive bicycle simulator*, *Sensors and Actuators A: Physical* **140**, 65 (2007).
- [7] R. Oliveira, R. Claudino, R. Kalid, T. Fröhlich, L. Gusmão, and H. Lepikson, *Estimate of the inertial torque in rotating shafts—a metrological approach to signal processing*, *Journal of Physics: Conference Series* **648**, 012019 (2015).
- [8] S. Caro and S. Bernardi, *The role of various sensory cues in self-speed perception: a bicycle riding simulator preliminary study*, in *Proceedings of the Driving Simulation Conference* (2015) p. 4p.
- [9] R. Herpers, W. Heiden, M. Kutz, D. Scherfgen, U. Hartmann, J. Bongartz, and O. Schulzyk, *Fivis bicycle simulator: an immersive game platform for physical activities*, in *Proceedings of the Future Play Conference* (2008) pp. 244–247.
- [10] J. M. Plumert, J. K. Kearney, and J. F. Cremer, *Children’s perception of gap affordances: Bicycling across traffic-filled intersections in an immersive virtual environment*, *Child Development* **75**, 1243 (2004).
- [11] A. L. Schwab, P. D. L. de Lange, R. Happee, and J. K. Moore, *Rider control identification in bicycling using lateral force perturbation tests*, *Proceedings of the Institution of Mechanical Engineers Conference, Part K: Journal of Multi-body Dynamics* **227**, 390 (2013).
- [12] R. C. Mclane and W. W. Wierwille, *The influence of motion and audio cues on driver performance in an automobile simulator*, *Human Factors and Ergonomics Society* **17**, 488 (1975).

- [13] J. P. Meijaard, J. M. Papadopoulos, A. Ruina, and A. L. Schwab, *Linearized dynamics equations for the balance and steer of a bicycle: a benchmark and review*, in *Proceedings of the Royal Society of London A: Mathematical, Physical and Engineering sciences*, Vol. 463 (The Royal Society, 2007) pp. 1955–1982.
- [14] A. Shahar, V. Dagonneau, S. Caro, I. Israël, and R. Lobjois, *Towards identifying the roll motion parameters of a motorcycle simulator*, *Applied Ergonomics* **45**, 734 (2014).
- [15] D. Too, *The effect of body configuration on cycling performance*, in *Proceedings of International Society of Biomechanics in Sports Conference*, Vol. 1 (1988) pp. 51–58.
- [16] O. Lee, R. Happee, and A. L. Schwab, *On the importance of haptic feedback in the balance task of bicycling*, in *Proceedings of ECCOMAS Multibody Dynamics Conference* (2015) pp. 7–8.
- [17] J. K. Moore, *Human control of a bicycle*, Ph.D. thesis, University of California Davis, Davis, CA, Aug. (2012).
- [18] Fagor, *Calculation of rotary encoder resolution*, (2013).
- [19] D. S. De Lorenzo and M. Hull, *Quantification of structural loading during off-road cycling*, *Journal of Biomechanical Engineering* **121**, 399 (1999).
- [20] A. Jackson and M. Dragovan, *An experimental investigation of bicycle dynamics*, *American Journal of Physics* (1998).
- [21] K. Y. Cheng, D. Bothman, and K. Astrom, *Bicycle torque sensor experiment*, (2003).
- [22] K. Iuchi and T. Murakami, *An approach to fusion control of stabilization control and human input in electric bicycle*, in *Proceedings of ECON 32nd Annual Conference on IEEE Industrial Electronics* (2006) pp. 3211–3216.
- [23] S. Cain and N. Perkins, *Comparison of a bicycle steady-state turning model to experimental data*, in *Proceedings of Bicycle and Motorcycle Dynamics Conference* (2010).

# 8

## Discussion

The aim of this thesis is to derive bicycle rider control models, based on experimental data, that mimic the rider in his balance control task at various forward speeds. These rider control models can help to understand cyclists falls, improve training techniques, artificially assess the handling properties of new bicycle designs and create active balance control systems (e.g. steer assist). To experimentally quantify and model the rider control behaviour we have designed and built three state-of-the-art bicycle mock-ups. The first mock-up we developed is an instrumented bicycle which we used to identify the apparent mass and seat-to-sternum transmissibility transfer functions. The transfer functions obtained herein are necessary to derive the parameters of biomechanical models which can later be used to optimize the design of suspensions and steering stabilizers that can enhance safety. On the other hand, the rider control models identified herein together with the steer-by-wire bicycle and simulator can guide towards the development of design of active balance control systems. Across the thesis chapters information related to the design and construction of the instrumented bicycles and system identification techniques are presented.

### 8.1. Facilities

Over the course of four years three experimental bicycles were designed and built at the TU Delft bicycle laboratory in order to conduct this research. In this section we describe the challenges that we faced during the design and build of these experimental bicycles, the merits of the setups, and discuss further technical improvements and usage.

#### 8.1.1. Instrumented bicycle mock-up

To identify the rider's body response to whole body vibration a dedicated modular experimental set-up was developed, consisting of a custom made bicycle mock-up

placed on an industrial high-end hexapod, see Figure 8.1. The mechanical structure of the bicycle mock-up consists of standard bicycle parts and steel tubes held together with aluminium clamps. The steering assembly is fixed and the footpegs are placed symmetrically in order to obtain comparable results between the two sides. The handlebar can not rotate around its axis at the moment. For future experiments it is recommended to modify the steering assembly and install rotating ball bearings and an electric motor inline with the steering shaft. With this upgrade perturbations around the handlebars can be accomplished and the intrinsic and reflexive responses of the rider arms around this axis could be identified as well. The design of the steering assembly can also be improved and become reconfigurable. For instance, the tubes that connect the steering shaft to the seatpost and front base may be removed. Linear sliding bearings can be integrated in the headtube and base clamps of the steering assembly to allow the handlebars to move in the longitudinal and vertical direction. This way a consistent rider posture would be possible, even when subjects with different bodybuild are participating in the experiments. Although, this was unnecessary for our experiments, all participants had similar bodybuild and obtained a consistent posture during the perturbation trial.

The bicycle mock-up is equipped with an inertial measurement unit (IMU) and a total of 13 full-bridge strain gauge sensors. The strain gauges are able to measure all three-dimensional forces (except for the footpegs forces in lateral Y-axis, where no relevant force responses are expected). An additional IMU was added to the rider torso in order to monitor its response during the perturbations. A data acquisition system from National Instruments (LabVIEW) and MTW Awinda (Xsens software) sampled the strain gauges and IMU signals at 100 Hz. All data derived during the experiments gave estimates of high quality and static mass measurements had a low standard deviation. There were mainly two issues related to the sensing and data logging during the experiments. Regarding the force measuring it turned out that the handlebars are more compliant in the vertical and longitudinal directions compared to the lateral. To determine crosstalk interference high lateral applied force were required compared to the other two directions. It turned out to be tricky to hold the handlebar in a vertical position while applying increasing loads at the lateral direction. To solve this problem and also reduce any geometry artifacts we could replace the handlebars with a straight steel tube, albeit, in that case the handlebar geometry would not have been realistic. Synchronizing and logging problems were also evident for both the force and acceleration signals. Apparently, two different software were used for the former and latter signals. To solve the synchronization issues a sinusoidal signal was implemented in the beginning and end of the measurement sequences. The signal served as a time stamp and synchronization was accomplished by cross-correlation between the two signals. Data logging at the sampling rate was accomplished by switching from Windows to Macintosh and cancelling out all running tasks related to other threads. For future research it is recommended to purchase two new IMUs and plug them directly to the Labview data acquisition system, this will be sufficient to avoid the aforementioned issues.

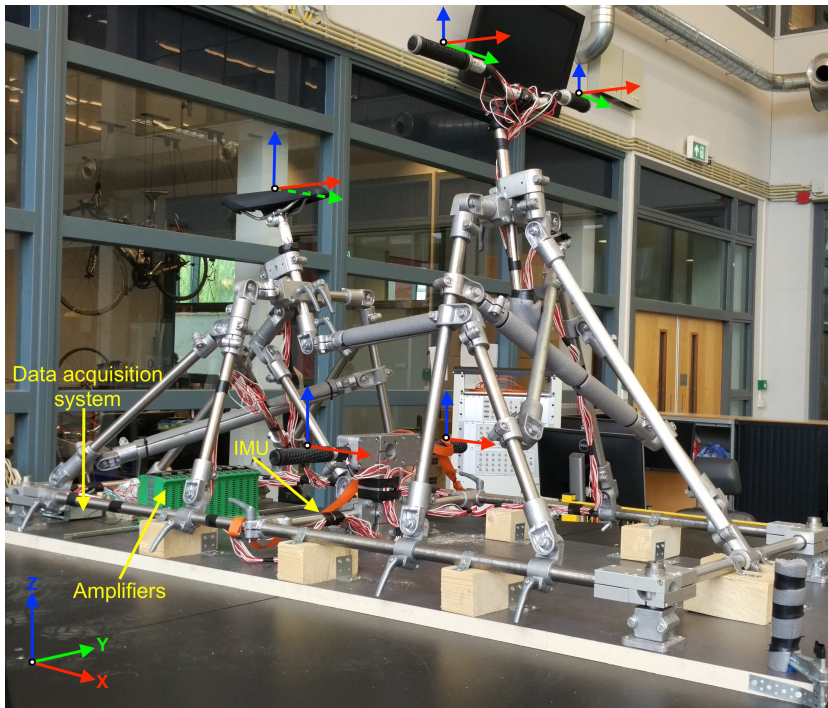


Figure 8.1: Instrumented bicycle mock-up mounted on the hexapod.

### 8.1.2. Steer-by-wire bicycle

To investigate how humans control a bicycle and investigate the effect of handlebar torque feedback on rider control a steer-by-wire bicycle was designed and built, see Figure 8.2. The steer-by-wire (SBW) bicycle is instrumented with multiple sensors that are able to measure most bicycle states. Two servomotors were selected to control the fork and handlebar and a rear wheel hub-motor with a throttle, a cruise controller was used to ride the bicycle without pedalling. The mechanical design of the bicycle frame was based on the Batavus Browser (56 cm) dutch city bike. Two design concepts were developed. The first design was similar to the first steer-by-wire prototype developed by Nick Appelman et al. [1] at TU Delft bicycle laboratory. A normal bicycle frame was used as a baseline for the steer-by-wire system. To solve the belt drive slip of the previous prototype a reduction gearhead and a tensioner was included in the later design. Unfortunately, the rigidity of the handlebar structure was proven to be insufficient compared to a normal bicycle frame. For this reason, it was decided to proceed with a second design which included a custom made bicycle frame with an upper and lower headtube assembly (see grabcad repository for all designs [2]).

To keep the handlebar height close to a normal mechanically steered bicycle every sensor was selected to have a minimum size and weight. A custom made torque

sensor was used to measure the applied handlebar torque and two absolute encoders were selected to measure the handlebar and fork position, respectively. For a compact design the actuator magnets of the encoders were integrated into the handlebar and fork shaft. The encoders performed with high level accuracy but aligning the fork encoder during mounting was challenging. The reading board of the fork encoder was mounted in an aluminium plate which was clamped at the bicycle frame from only one side. Due to limited space and extensive movement of the aluminum plate it was difficult to align the center of the magnet to that of the reading board. The later was accomplished by reading and comparing the handlebar and fork angles and readjusting the position of the plate accordingly. For a straight forward mounting of the fork encoder a similar aluminium plate with the one used for mounting the handlebar encoder is recommended. Another issue that we faced was related to the safety of our experimental subjects. A safety mechanism was required to be in place to mechanically engage the handlebar and fork in case of system failure. Initially, the idea of an electromagnetic clutch was explored. Albeit, the installation of a clutch was proven impractical due to misalignment of the servomotors. Thus, the implementation of a deadband mechanism was explored. Two mechanical deadband mechanisms were built and tested. The first mechanism used a mechanical pin and V-shape block to engage the handlebar and fork motors upon system failure. The mechanism was proven to be successful and all subjects were able to control the bicycle and make a complete stop without problems. However, the idea was aborted due to extensive wear of the belt drive. A second mechanism that connects the fork directly to the handlebars was examined. The mechanism consists of a steel tube mounted to the fork and a threaded rod with two metal spindels attached to the handlebars. The steel tube of the fork is connected to the threaded rod of the handlebar through a rectangular hole. Two spindle screws are used to adjust the deadband range and engage the handlebar and fork upon system failure (e.g., folding of the motors). The mechanism turned out to be successful for all speeds. All participants managed to control the bicycle and completed the experimental trials with safety. A group of five bachelor students designed and built a lateral balance perturbation device using compressed air for their thesis [3]. The device consisted of four main parts; a scuba diving tank, a solenoid valve, an electronic control module, and a bluetooth antenna for switching on/off the valve. The device was tested and was able to generate the force required for our experiments. Though, it turned out that the amount of noise by the expansion of air was distracting for the participants. For this reason a pulling rope mechanism with a force transducer in series was used to manually apply lateral impulsive forces at the seat post. The hardware and software of the steer-by-wire turned out to be successful the control loop frequency was configured at 1 kHz the same as the sampling frequency of the sensors and actuator signals. In total sixteen signals were successfully logged while controlling the servomotors without causing the buffer to overflow. All data derived gave estimates of high quality.

The steer-by-wire bicycle can also serve as an experimental platform to assess rider assist functions. The lateral stability of the bicycle could be improved with the ease of compiling new software in the controller without changing the physical

geometry of the bicycle. The handling qualities of the bicycle could be adjusted to everyone's needs with focus on the elderly and people with a physical handicap having trouble riding a conventional bicycle [4]. Schwab et al. [5] were the first who actually investigated in practice the impact of active steer-torque control on the lateral stability of a bicycle. Their results showed a considerably lower rider steer effort and increased stability at low forward speeds.

The steer-by-wire bicycle may also be used for identification of the rider's control behavior. Impulsive torques in the handlebars could be applied in order to identify the intrinsic and reflexive responses of the rider arms. The effect of countersteering during cornering could also be assessed. As recommended by Marumo and Nagai [6] removal of countersteering might be beneficial for controlling a two-wheeler, but of course this idea could be now tested in practice. Haptic guidance for lane keeping might also be tested, as suggested by Katagiri et al. [7] this can greatly improve safety. Different steering configurations such as reverse steering could be accomplished in order to explore the ability of the brain to adopt into the new steering configurations.



Figure 8.2: Steer-by-wire bicycle prototype with handlebar and fork actuators, sensors, pulling rope mechanism, digital controller and custom made battery pack.

### 8.1.3. Bicycle simulator

To evaluate further the role of the primary sensory systems and explore further rider control behaviour in a safe environment a static bicycle simulator with a haptic steering device was designed and built. The mechanical portion of the simulator consists of three main structural parts. A bicycle roller training base, a square tube

used as a steering column, and a rear half of a step-through bicycle frame, see Figure 8.3. To mount all the structural parts together several modifications were made and a combination of different types of adjustable blocks were used. The adjustable blocks were proven quite useful and gave us the flexibility to fixate all structural parts together without any major challenges. Only one problem was evident during testing of the simulator. Vibration of the powertrain was causing the screws of the hinge block that supports and titles the steering column to become loose. This resulted in misalignment between the two prismatic joints and as a consequence it was difficult to move the steering column horizontally to accommodate a large range of body sizes and bike geometries. To solve this issue we used loctite glue but as an upgrade a solid hinge clamp is recommended. Linear sliding bearings could also be added in both prismatic joints to reduce friction if necessary. The assembly of the haptic steering device turned out to be successful but there were two issues during testing. The first issue was related to the overload protection mechanism. The shear-pin was breaking at lower torques than expected. This was caused due to a mismatch between the indicated in the manual and actual shear strength of the selected nylon screws. Initially we thought to replace the overload mechanism with a torque limiter. However, as first observed by Jason Moore [8] industrial torque limiters are not functional at low rotating rates. Therefore, we followed the initial plan and continued testing in order to determine the proper screw size. The second issue was associated to the strength of the angular metal stripes that are used to mount the limit switches to the steering column. There were found insufficient to absorb the impact loads of the mechanical range limiter shaft without deforming. To absorb the impact loads and protect the mounts of the limit switches an elastic rubber was wrapped around the range limiter shaft. For future usage it might be useful to use a braking clutch in case the load is cycled more rapidly than the mechanical limiters can tolerate alone. A group of three bachelor students working under the supervision of Oliver Lee designed and built a pedal resisting unit for their thesis [9]. The idea was to install a chain drive unit and an electric motor at the rear rollers. During testing it was observed that the plastic roller strength was insufficient to support the applied resistive torques. Due to deformation of the sprocket mounts the chain was misaligned. Noise and extensive wear of the sprockets lead to exclude the powertrain unit from the final design. For future usage it is recommended to replace the driven plastic roller with a one made from carbon fiber to improve strength and avoid deformation due to the induced powertrain loads. The simulator is at the moment placed on a fixed base. This does not allow any rotational and translations movements. In the future, the simulator could be placed on a hexapod platform or similar. This way, virtual bicycle dynamics that are currently projected in a screen or head mounted display could be also perceived in the physical world.

#### 8.1.4. Summary

Three new setups have been developed, and two have already been used to investigate rider behaviour. For all three setups directions for further improvement are given. All three setups were useful in the research and show potential for future



Figure 8.3: TU Delft fixed base bicycle simulator.

usage. The bike simulator is work in progress requiring major further efforts in both hardware and software.

## 8

### 8.2. Findings

The aim of this section is to summarize all scientific findings of this thesis and to recommend possible ideas to extend further the obtained results.

#### 8.2.1. Some effects of crosswind on the lateral dynamics of a bicycle

In Chapter 2 we explored the effects of crosswind on bicycle dynamics and rider control. The uncontrolled bicycle was driven in the stable speed region and was subjected in a light & fresh wind breeze with an angle of attack of 30 degrees. The rider controlled bicycle was driven in the unstable speed region and was subjected in a fresh wind breeze with the same as the aforementioned angle of attack. Results showed that the uncontrolled bicycle is capable of stabilizing itself by turning into the wind after some short transient manoeuvre. Similar results were observed for the rider controlled bicycle. However, in the later case longer transient manoeuvres and a considerable steer torque effort were required to stabilize the bicycle. Additional simulations with different rider models and wind conditions might be performed in

order to extend further these preliminary results. For example, a rider model which has its gains identified during naturalistic bicycle riding and input disturbances like a gust of wind or turbulence could be also explored. For the former wind condition this could be simulated by a finite impulse response input, whereas, for the later by spatially correlated wind time histories. The exact magnitudes and frequencies of these disturbances should be selected in respect to the linearity limits of the selected bicycle model [10].

### 8.2.2. The dynamic response of the bicycle rider's body to vertical, fore-and-aft and lateral perturbations

In Chapter 3 we presented the dynamic response of the bicycle rider's body subjected to translational motions by means of apparent mass (APMS) and seat-to-sternum transmissibility (STST) functions. Heave and surge motion interacted with each other and showed similar dynamics (i.e. a result of subject leaning forward). The vertical STST and APMS of the seat and handlebars showed a resonance at 5 Hz. The longitudinal STST and APMS had a resonance at 2 Hz. Small resonant frequency variations were evident, howbeit this could be attributed to different body masses and postures. Sway was independent from the other two motions, the lateral STST and APMS showed similar trends: no resonance was observed and postural control was evident in both measurements. For heave and surge the rider's body acted as a rigid mass up to 2 Hz. For sway the rider's body behaved like a horizontal mass spring-damper system (pelvis) with a torsional spring inverted pendulum (trunk) on top for all frequencies. The high magnitude APMS for sway motion were perhaps a result of the angular trunk dynamics. For sway the rider's body dynamics were totally different from the other two motions. The rider's body was not close to a rigid mass even for the lowest frequencies. Hence, a parametric model is significantly important in order to understand better the passive dynamic contribution of the rider to the bicycle-rider system especially during lateral disturbances. Additionally, we explored the dynamic response of the rider's body subjected to rotational motions by means of APMS and STST functions [11]. The APMS was calculated as the ratio between measured forces and angular acceleration. The STST was considered as the ratio between the angular velocities of the torso and bicycle mock-up. For the pitch and yaw motions, relative high gains with low coherence were observed at low frequencies. Above 1 Hz, interfaces with high coherence were characterised by a main resonance peak at 1.8 Hz and 2.3 Hz for the former and later motion, respectively. A similar resonance frequency was found in the APMS and STST responses for the yaw motion. For the sway and roll motions, responses were almost identical. Postural control was evident during these motions. Obviously the rider uses his feet and hands to stabilize his pelvis and trunk in space. All findings discussed above are based on an average over twenty-four subjects. For future research a more straight forward approach to understand the rider's responses during rotational motions could be to estimate the mechanical impedance (i.e., the ratio between the applied torques and angular velocity).

### 8.2.3. Rider control identification in bicycling using lateral force perturbation tests

In Chapter 5, 6 we described several lateral force perturbation experiments during bicycling. The aim of the experiments was to model the steering and balance behaviour of bicycle riders and investigate the effect of handlebar torque feedback on rider control. The steer-by-wire bicycle designed and built at TU Delft bicycle laboratory was used as an experimental platform to capture the rider responses for two different steering configurations. In the first configuration the rider has the torque feedback loop connected (haptics on) and the plant dynamics approximate a normal bicycle. In the second configuration the steering dynamics change to that of steer-by-wire (haptics off). This means that the plant approximates a bicycle with decoupled roll-steer dynamics, hence the rider receives only steering torque feedback due to the inertia of the handlebars and not due to the front wheel dynamics.

In Chapter 5 we present the response of the rider's control actions in the time domain by means of impulse response functions (IRFs). To assess if there is any statistical significant difference between the two configurations we defined three performance metrics and calculated the delay between the two steering responses. There were no significant differences between the two steering configurations. Neither performance or steering effort was affected, but steering responses were faster for the latter configuration. Even though a steer-by-wire system decouples the roll-steer dynamics (haptics off) the torque feedback information is severed but not totally cancelled. State information can be deduced from the position of the handlebars and remaining inertial steering feedback. To neutralize the effect of inertial feedback we could have applied negative stiffness by using the handlebar motor. However, due to constraints related to the PD tracking controllers of the steer-by-wire system this would have been difficult in practice (see github repository for software [12]).

To examine further the rider's responses for the two aforementioned configurations in Chapter 6 we present three rider control model with increased complexity. In addition, we explored a third configuration where the internal torque feedback loop of the rider is disconnected and the plant dynamics approximate a bicycle without steering torque feedback ( $T_\delta = 0$ ). All models showed best performance for the haptics-on configuration and a high degradation in the fitting for the without steering torque feedback ( $T_\delta = 0$ ), which proves that steering feedback is important for balancing and controlling a bicycle. For the later control model, which takes into account steer torque, position feedback and sensorial delays, we also omitted both the steering angle  $\delta$  and steering rate  $\dot{\delta}$ . A negative effect in the fitting performance was observed especially for the highest speeds. The high degradation of the heading and roll indicates that handlebar position and velocity feedback (muscle spindles) enhances bicycle heading and roll perception at higher speeds. For all models the predicted magnitudes of the roll angle remained two to three times smaller than the actual measured output. During the experiments the upper body remained unconstrained and acted as a double inverted pendulum with some tor-

sional spring and damping properties. Additionally, simulations showed that rider compliance can influence the magnitude of the roll angle. A much higher roll angle of the bicycle is expected when the rider is more compliant. For the above reasons it is necessary to identify the spring and damping properties of the rider body and extend the Carvallo-Whipple bicycle model [10] in order to obtain better fitting in the roll responses. All findings discussed above are based on an average over twenty subjects.

Future work can be directed towards a deeper understanding of the haptic feedback mechanism at the handlebars by varying the dynamic steer stiffness of the handlebars and applying handlebar steer torque perturbations. Preliminary steer torque perturbation experiments showed high inter-subject variability especially for the lowest speeds [13]. This might be due to the fact that some participants did not adapt to the system completely which caused them to exhibit significant variance in their responses. On the other hand, this could also be an effect of unmodelled dynamics, such as upper body movement and extensive movements of the arms. In the future it might be necessary to understand how the rider modulates the intrinsic steering and damping stiffness in relation to speed. Also interesting would be to study the interaction between the intrinsic and reflexive components of the rider arms in order to understand better the biomechanics behind steer torque control.

#### 8.2.4. Bicycle simulator

In Chapter 7 we describe the design and hardware selection of a fixed base bicycle simulator that was used to conduct rider control experiments in virtual environment. Preliminary tests using the bicycle simulator showed that all subjects can manoeuvre the bicycle when a car-like stable bicycle model is used to generate haptic feedback and project the dynamics in the virtual environment. Visual roll and pitch of the horizon turned out to be an effective tool for creating the illusion of physical roll and pitch. The majority of the participants showed a tendency to excessively lean over the bicycle frame and due to the vision and vestibular sensory conflict they reported symptoms of motion sickness during and after the experiments.

### 8.3. Integration and outlook

From the above Section 8.2 it became apparent that data collected during different experiments and obtained models could be combined together to extend further the findings of this research. Regarding the rider control model that was used to study the effect of crosswind on bicycle dynamics the following modifications may be utilized. The data collected during the naturalistic bicycle experiments of Chapter 5 can be employed instead of the previous treadmill data. This is recommended due to the fact that the narrow path of the treadmill might have introduced statistical bias. The estimation of the controller gains especially to the one attributed to the bicycle heading might have affected the crosswind simulations. To a certain degree a more realistic rider control behaviour during crosswind could have been achieved using the latter data. Another possibility can be to replace the initially selected controller

by a more sophisticated rider model. However, it does not change the narrative of the end results. For instance, the rider control model of Chapter 6 which takes into account steer torque feedback and sensorial delays might have been applied instead. Furthermore, the plant dynamics of the Carvallo-Whipple bicycle model [10] could have been extended to that of a steer-by-wire bicycle. The ability of the rider to control a bicycle when subjected to crosswind for different steering configurations would have been possible. The mismatch between the predicted and actual measured magnitudes of the roll angle observed for all rider control models in Chapter 6 may have been addressed as follows. The Carvallo-Whipple bicycle model [10] could have been extended by adding a passive rider model like in a previous study [14]. A horizontal mass spring damper system with a torsional spring inverted pendulum on top would have been a sufficient solution to simulate upper body lean and trunk dynamics. The properties of the added model could have been identified from the rider's body responses during the sway motion that were presented in Chapter 3.

## References

- [1] N. Appelman and A. L. Schwab, *Dynamics and control of a steer-by-wire bicycle*, Master's thesis, Delft University of Technology (2012).
- [2] G. Dialynas, *GrabCad repository* (2015).
- [3] M. Van Beem, F. Van Beurden, S. Drost, R. Krijnen, and L. Zandt, *Lateral perturbation mechanism*, Bachelor's thesis, Delft University of Technology (2017).
- [4] K. J. Astrom, R. E. Klein, and A. Lennartsson, *Bicycle dynamics and control: adapted bicycles for education and research*, IEEE Control Systems Magazine **25**, 26 (2005).
- [5] A. L. Schwab and N. Appelman, *Dynamics and control of a steer-by-wire bicycle*, in *Proceedings of Bicycle and Motorcycle Dynamics Conference* (2013).
- [6] Y. Marumo and M. Nagai, *Steering control of motorcycles using steer-by-wire system*, Vehicle System Dynamics **45**, 445 (2007).
- [7] N. Katagiri, Y. Marumo, and H. Tsunashima, *Controller design and evaluation of lane-keeping-assistance system for motorcycles*, Journal of Mechanical Systems for Transportation and Logistics **2**, 43 (2009).
- [8] J. K. Moore, *Human control of a bicycle*, Ph.D. thesis, University of California Davis, Davis, CA, Aug. (2012).
- [9] H. Coenraadm, L. Stefan, and R. Folkert, *Pedal power*, Bachelor's thesis, Delft University of Technology (2016).
- [10] J. P. Meijaard, J. M. Papadopoulos, A. Ruina, and A. L. Schwab, *Linearized dynamics equations for the balance and steer of a bicycle: a benchmark and review*, Proceedings of the Royal society A: mathematical, physical and engineering sciences **463**, 1955 (2007).

- [11] J. W. De Haan, A. C. Schouten, R. Happee, G. Dialynas, and A. L. Schwab, *The apparent mass and transmissibility of a bicycle-rider system*, [Master's thesis](#), Delft University of Technology (2019).
- [12] G. Dialynas, [github repository](#) (2015).
- [13] C. Christoforidis, A. C. Schouten, R. Happee, G. Dialynas, and A. L. Schwab, *Rider control identification in cycling taking into account steer torque feedback and sensorial delays*, [Master's thesis](#), "under embargo", Delft University of Technology (2019).
- [14] A. L. Schwab, J. P. Meijaard, and J. D. G. Kooijman, *Lateral dynamics of a bicycle with a passive rider model: stability and controllability*, *Vehicle System Dynamics* **50**, 1209 (2012).

# 9

## Conclusions

All three experimental bicycles designed and built in TU Delft bicycle laboratory served successfully the aims of this research. Their capabilities in measuring, collecting data and generating disturbances exceed our initial expectations. More specific, the instrumented bicycle mock-up was proven successful in measuring the apparent mass (APMS) and seat-to-sternum transmissibility (STST) of the rider's body in all translational motions with high level of accuracy and without any malfunctions during the experiments. The steer-by-wire bicycle capabilities were proven more than sufficient for our experiments. The tracking error between the fork and the handlebars was minimum. The servomotors of the steering assembly were proven adequate in generating steer torque perturbations in a large range of magnitudes. Preliminary tests using the bicycle simulator showed that all subjects can manoeuvre the bicycle in the virtual environment when a car-like stable bicycle model was used.

Computer simulations showed that crosswind in bicycling has a considerable effect on the stability and control of the bicycle. Increasing crosswind speed can make an uncontrolled bicycle unstable for all forward speeds. The rider control effort increases considerably as crosswind speed increases, a constant steer torque is required to keep the bicycle at a straight heading.

The response of the rider's body subjected to vertical, fore-and-aft and lateral perturbations revealed that rider applied forces in all three-dimensional directions. Heave and surge motion interacted with each other and similar responses and were observed. Sway showed weak interaction with heave and surge and the responses were totally different from the other two motions. The vertical and longitudinal APMS for almost all bicycle interfaces followed the resonance of the STST measurements. All showed a twice as high magnitude at resonance, albeit a more heavily damped system was apparent in the STST measurements. Resonant frequencies were considerably higher in the vertical direction as compared to the longitudinal

direction. Lateral measurements showed no resonance, and trunk postural control was evident in the APMS measurements. For most frequencies and perturbation directions the response of the rider's body was not close to a rigid mass, hence a parametric model is required to understand better the passive dynamic contribution of the rider to the bicycle-rider system.

In an effort to iterate over existing rider control models, the SDROP model has been created that successfully accounts for sensory delays by the use of an internal predictive model. The performance of the SD model has proven that implementation of sensory delays without feedforward compensation does not produce results that match the experimental data. A prediction strategy has been developed that manages to circumvent the inability of the conventional Smith predictor to work on inherently unstable open loop systems. The rider model follows the necessary stability condition of steer into the fall and mimics human control in a natural way. All simulated responses match the non-parametric outputs obtained from both datasets with high level of performance, even when internal model inaccuracies are introduced.

With this rider model the importance of accurate determination of the various state variables via our sensors has been examined. The analysis showed that a highly realistic rider model must include steer angle, steer velocity and torque feedback to obtain adequate performance at all speed levels. Although, if the torque feedback loop is severed and not disconnected as in the haptics off configuration, state information might be deduced by the remaining inertial properties of the handlebar. Even though a steer-by-wire system decouples the roll-steer dynamics (haptics off) the remaining inertial torque and position feedback of the handlebar is proven to be adequate for the rider to control and balance a bicycle. The absence of haptic feedback substantially changes the system dynamics where with haptics off the bicycle is always unstable but apparently riders can effectively stabilise and control the system. Future work can be directed towards a deeper understanding of the haptic feedback mechanism at the handlebars by varying the dynamic steer stiffness of the handlebars and applying handlebar steer torque perturbations.



# Acknowledgements

This doctoral thesis is the result of a unique multidisciplinary training experience, which comprised empirical research and mathematical modelling of rider behaviour. In September 2015, I joined the Department of Biomechanical Engineering, Delft University of Technology as a Marie Curie Fellow in the European project MOTORIST (Motorcycle Rider Integrated Safety) project Nr.608092, [www.motorist-ptw.eu](http://www.motorist-ptw.eu). Within this project, I had the opportunity to interact with international experts in different fields and to extend my knowledge in directions I had never thought of before being a mechanical engineer. Mastering relevant knowledge within different disciplines and reconciling conflicting research paradigms in the absence of an established framework were the main scientific challenges during my doctoral research. I would like to thank all people who have been important to me during this journey.

I express my sincere gratitude to my supervisors Arend L. Schwab and Riender Happee for giving me the opportunity to get involved in the MOTORIST project. They provided me with the best opportunities available for my personal and professional development. Their critical comments and enthusiastic support helped me greatly in improving the structure of my thoughts and in finding my own research direction. I am particularly grateful to my daily supervisor Arend L. Schwab for his guidance and openness in sharing his knowledge on bicycle dynamics and experimental facilities. I am thankful to Riender Happee for providing me with excellent scientific advice on biomechanics and modeling of the rider controller and for constantly coaching me with professionalism and respectfulness during the last five years.

I am also deeply grateful to Jan van Frankenhuyzen and Jos van Driel for their mechanical and electrical advice respectively, Alex de Kraker from St Joris Cycles for building the custom bicycle frame of the steer-by-wire bicycle, Oliver Lee for having designed the printed circuit boards and Mick van Gelderen for his support in the implementation of the real time operational system (RTOS). I have truly enjoyed the freedom in this journey toward learning and becoming an independent researcher.

Focusing on research would not have been possible without valuable administrative staff. I thank Nancy Kouters, Sabrina Ramos Rodrigues and Angelique Timmerman of the biomechanical department for their support during my studies and during the preparation of my defence.

During my doctoral studies, I received training in different disciplines. I am grateful to all researchers involved in the MOTORIST project for sharing scientific knowledge

in the field of human factors and biomechanics, which had a profound impact on the empirical research I conducted in the early stages of my PhD. Thanks to my colleagues at TU Delft for their support during tough times, and my students Tony Prats, Max Greidanus, Robert Rooijmans, Koen Verbruggen, Peter Visser, Marnix van Beem, Frank van Beurden, Christian Drost, Robert Krijnen, Luc Int Zandt, Jelle Wailing de Haan and Christos Christoforidis for their individual effort and contribution to the project. In addition, I am grateful to the TU Delft Graduate School for very useful support in developing transferable and research related skills. Being a member of the Graduate School has been inspiring and motivating.

Finally, I express my most sincere gratitude to my partner Elisavet Kotsi, my parents Michail Dialynas and Glykeria Delivasi, and my brother Nikolaos Dialynas for their unconditional love. They have always respected my choices and supported me despite how far I was. Heartfelt thanks, I could not find better companions in this journey.

Georgios Dialynas, September 2020

# List of publications

## Conference proceedings

1. A. L. Schwab, G. Dialynas and R. Happee, Some effects of crosswind on the lateral dynamics of a bicycle, In Multidisciplinary Digital Publishing Institute Proceedings **2**, 218, (2018), <https://doi.org/10.3390/proceedings2060218>. [Chapter 2]
2. G. Dialynas, R. Happee, A. L. Schwab, Design and implementation of a steer-by-wire bicycle, In Proceedings of the 7th Annual International Cycling Safety Conference, (2018). [Chapter 4]
3. G. Dialynas, C. Christoforidis, R. Happee, A. L. Schwab, The effect of haptic feedback in the balance task of bicycling, In Proceedings of the 4th Triannual International Bicycle and Motorcycle Dynamics Conference, (2019). [Chapter 5]

## Journal publications

1. G. Dialynas, J. W. de Haan, A. C. Schouten, R. Happee, A. L. Schwab, The dynamic response of the bicycle rider's body to vertical, fore-and-aft and lateral perturbations, Proceedings of the Institution of Mechanical Engineers, Part D: Journal of Automobile Engineering, (2019), <https://doi.org/10.1177/2F0954407019891289>. [Chapter 3]
2. G. Dialynas, C. Christoforidis, R. Happee, A. L. Schwab, Rider control identification in cycling taking into account steer torque feedback and sensorial delays, **Submitted**, (2020). [Chapter 6]
3. G. Dialynas, R. Happee, and A. L. Schwab: Design and hardware selection for a bicycle simulator, Mech. Sci., **10**, 1-10, <https://doi.org/10.5194/ms-10-1-2019>, 2019. [Chapter 7]

# Curriculum Vitæ

## Personal

05-03-1988 Born in Amaroussion, Athens, Greece.

## Education

2002-2005 2nd Senior High School of Ierapetra, Ierapetra, Crete, Greece.

2005-2010 BSc in Mechanical Engineering, Alexander Technological Educational Institute, Thessaloniki, Central Macedonia, Greece.

2013-2014 MSc in Electromechanical Engineering, University of Antwerp, Antwerp, Flanders, Belgium.

2015-2020 PhD in Biomechatronics Human Machine Control, Delft University of Technology, Delft, South Holland, the Netherlands.

## Volunteer experience

2018-2019 University Ambassador, Reload Greece, Delft, South Holland, the Netherlands.

2017-2018 Representative of the Biomechanical Department, PhD Council 3mE, Delft, South Holland, the Netherlands.

2016-2017 Lead Powertrain Engineer, Ecorunner VI team, Delft, South Holland, the Netherlands.

2014-2015 Member & Volunteer, Road Safety Institute (RSI) Panos Mylonas, Galatsi, Athens, Greece.

## Awards

2015 Marie Curie Fellowship

# Propositions belonging to the PhD thesis

These propositions are regarded as lending themselves to opposition and as defensible, and have been approved as such by the promotor Dr. R. Happee and copromotor Dr. A. L. Schwab.

1. Existing steering stabilizers that are used primarily in motorcycles might have a negative impact if they are used on bicycles during the challenging moments of a gusty crosswind due to the higher resistance of the bicycle steering.

*This proposition pertains to this dissertation Chapter 2.*

2. Biodynamic lumped human-machine models with parameters derived based on experimental measurements (e.g. during mountain biking) can lead to the design of optimal suspensions for competitive racing.

*This proposition pertains to this dissertation Chapter 3.*

3. Steer-by-wire technology can improve safety by modifying the actions taken by the rider, making the two-wheeler both easier and more comfortable to control.

4. A low cost electric motor an IMU and a wheel speed sensor is all that is needed to improve the lateral stability of two-wheelers at low speeds.

5. A steer-assist system is not the only way to keep seniors upright.

*Propositions 3, 4, 5 pertain to this dissertation Chapter 4.*

6. Steering feedback is important for balancing and manoeuvring a bicycle.

*This proposition pertains to this dissertation Chapter 5, Chapter 6.*

7. A virtual reality bicycle simulator might be used as a balance and motor function rehabilitation system with further objective measurements of balance ability of the patients.

*This proposition pertains to this dissertation Chapter 7.*

8. Handling qualities of existing bicycles can be improved by machine learning algorithms such as artificial neural networks.

9. Self-balancing motorcycles from BMW, Yamaha and Honda are designed and built for marketing reasons, commercial usage of such motorcycles is not foreseeable in the near future.
10. Life for some people is like riding a bicycle with no assist, and for others like riding a bicycle with steer-assist.